



universität  
wien

# MAGISTERARBEIT

Titel der Magisterarbeit

**“Imaging and photometry of U Antliae and AQ Andromedae  
using the Herschel space telescope”**

Verfasser

**Bernhard Baumann, Bakk.rer.nat.**

angestrebter akademischer Grad

**Magister der Naturwissenschaften (Mag.rer.nat.)**

Wien, 2012

Studienkennzahl lt. Studienblatt: A 066 861

Studienrichtung lt. Studienblatt: Magisterstudium Astronomie

Betreuer: A. Univ. Prof. Dr. Franz Kerschbaum



# Danksagung

Die hier vorgestellte Masterarbeit wurde in Zusammenarbeit mit dem MESS Konsortium (<http://www.univie.ac.at/space/MESS/>) und dem Institut für Astronomie in Wien (<http://astro.univie.ac.at/>) erstellt.

Ich bedanke mich bei Franz Kerschbaum, dass ich bei diesen internationalen Projekten, Herschel Space Telescope und MESS, mitarbeiten durfte und für die Betreuung der Arbeit.

Mein herzlicher Dank gilt der AGB-Arbeitsgruppe (<http://www.univie.ac.at/agb/>), besonders Roland Ottensamer für die vielen wertvollen Diskussionen, Anregungen und Korrekturen sowie Marko Mecina für die gute Zusammenarbeit als Studienkollege.

Weiteren Korrekturlesern wie Verena Baumgartner und meinem Bruder Michael gilt mein Dank.

Zu guter Letzt möchte ich mich bei meinen Eltern sowie meinem Bruder Michael für die Unterstützung und Motivation während meines Studiums bedanken.

Wien, im März 2012.



# Zusammenfassung

Die vorliegende Masterarbeit beinhaltet die Beobachtungsauswertung und die Datenreduktion zweier Asymptotic Giant Branch (AGB) Sterne, U Ant und AQ And, welche mithilfe des Herschel Weltraumteleskops aufgezeichnet wurden. Die Ergebnisse dieser Datenreduktion werden mit der Modellierung in DUSTY verglichen, welche den Strahlungstransport in staubigen Umgebungen rund um Sterne simuliert. Mit den Ergebnissen ist es möglich, Rückschlüsse über die aktuelle und anschließende Entwicklung der Sterne zu ziehen.

Im ersten Teil erhält der interessierte Leser eine Einleitung zu AGB-Sternen und ihren Eigenschaften. Dadurch erkennt der Leser, wie wichtig es ist, die Entwicklung dieser Spätstadien-Objekte zu studieren. AGB-Sterne bestehen aus einem Kohlenstoff- und Sauerstoff-Kern mit umgebenden Wasserstoff- und Helium-Brennschalen. Diese Brennschalen stellen den Hauptteil der Energieproduktion und Leuchtkraft in dieser Phase der Sternentwicklung dar. Die stellare Hülle ist auf einige hundert Sonnenradien aufgebläht und begünstigt die Entstehung von Molekülen und Staub in den äußeren kühleren Regionen. Staub ist der Hauptgrund für den hohen Massenverlust, da der Impuls des Strahlungsfelds vom Staub aufgenommen und nach außen abgegeben wird. Weiters führt ein hoher Massenverlust von einigen Erdmassen pro Jahr zu zirkumstellaren Hüllen oder auch “attached” bzw. “detached shells” genannt, welche man im Infraroten mit dem Herschel Weltraumteleskop beobachten kann.

Das Herschel Weltraumteleskop ist im Kapitel 2 beschrieben und besonderes Augenmerk ist auf das SPIRE Instrument gelegt. Ein eigenes Kapitel erläutert die technischen Eigenschaften sowie die Reduktion der Objekte für SPIRE. Das Reduktionskapitel präsentiert in großem Umfang die Datenstruktur, das Map-making sowie den Quellcode, um den Leser bei nachfolgenden Arbeiten zu unterstützen.

Kapitel 3 “Science Objects” stellt die wichtigen Eigenschaften und Merkmale von beiden Objekten, U Ant und AQ And, dar. Zusätzlich gibt es eine Publikationsübersicht, die dem Leser eine Zusammenfassung der Publikationen mit Schwerpunkt “detached shell”-Beobachtung gibt.

Das abschließende Kapitel befasst sich mit den Ergebnissen von der Beobachtung und der Modellierung von U Ant und AQ And. Die Ergebnisse der Beobachtung und die Aperturphotometrie befinden sich in einem separaten Kapitel. Schlussendlich sind die Resultate der Modellierung in einem Kapitel zusammengefasst und werden im Kapitel “Conclusion and interpretation” diskutiert.



# Abstract

In this master thesis the observation evaluation and data reduction of two Asymptotic Giant Branch (AGB) stars, U Ant and AQ And, observed with the Herschel space telescope, is presented. The results from the data reduction will be compared with the modeling in DUSTY, which simulates the radiation transport in dusty environments around stars. With these results it is possible to draw conclusions about the current and subsequent evolution of the stars.

The first part gives the interested reader an introduction to AGB-stars and their properties. So the reader will know, why it is important to study the evolution of these late-stage-objects. AGB-stars consist of a carbon- and oxygen-rich core with surrounding hydrogen- and helium-burning shells, which dominate the energy production and luminosity of the star. The stellar envelope is extended to a few hundred sun radii and benefits the formation of molecules and dust in the outer cooler regions. Dust acts as main driver for the stellar wind because of its capacity of taking up momentum of the radiation field. Furthermore this high mass-loss of a few earth masses per year is visible in the infrared as circumstellar envelope like an attached or detached shell, which can be observed with the Herschel space telescope.

The Herschel space telescope is described in chapter 2, with special focus on the SPIRE instrument. A dedicated chapter outlines the technical functionality and data reduction part of the objects for SPIRE. The reduction process chapter presents in extended scope the data structure, the map-making as well as the final source code to support the reader's subsequent workings.

Chapter 3 "Science Objects" introduces the important properties and features of both science objects, U Ant and AQ And. In addition an overview of publications about (detached) shell-detection is given.

The final chapter outlines the results of U Ant and AQ And from the observations and the modeling. The final maps from the observation as well as the aperture photometry can be found in a separate chapter. Furthermore the modeling outcomes are summed up in one chapter per object and are discussed in chapter "Conclusion and interpretation".





# Contents

|   |           |
|---|-----------|
| <b>Danksagung und Zusammenfassung</b>             | <b>3</b>  |
| <b>Abstract</b>                                   | <b>7</b>  |
| <b>1 Introduction to AGB-stars</b>                | <b>11</b> |
| 1.1 AGB-stars in general . . . . .                | 11        |
| 1.2 Evolution to carbon stars . . . . .           | 17        |
| 1.3 Dust and mass loss . . . . .                  | 26        |
| <b>2 Herschel space observatory</b>               | <b>31</b> |
| 2.1 Mission overview . . . . .                    | 31        |
| 2.1.1 MESS consortium . . . . .                   | 38        |
| 2.2 The SPIRE instrument . . . . .                | 39        |
| 2.2.1 Technical overview . . . . .                | 39        |
| 2.2.2 Data reduction . . . . .                    | 45        |
| 2.2.2.1 Data structure . . . . .                  | 46        |
| 2.2.2.2 Reduction process . . . . .               | 48        |
| 2.2.2.3 MADMap . . . . .                          | 56        |
| 2.2.2.4 Scanamorphos . . . . .                    | 57        |
| <b>3 Science objects</b>                          | <b>61</b> |
| 3.1 U Ant . . . . .                               | 61        |
| 3.1.1 Properties and features . . . . .           | 61        |
| 3.1.2 Publication overview . . . . .              | 63        |
| 3.2 AQ And . . . . .                              | 69        |
| 3.2.1 Properties and features . . . . .           | 69        |
| 3.2.2 Publication overview . . . . .              | 70        |
| <b>4 Science data results</b>                     | <b>73</b> |
| 4.1 U Ant . . . . .                               | 73        |
| 4.1.1 PACS and SPIRE observations . . . . .       | 73        |
| 4.1.2 Photometry and flux determination . . . . . | 80        |
| 4.1.2.1 Black body estimation . . . . .           | 91        |
| 4.1.3 Model fitting with DUSTY . . . . .          | 94        |
| 4.1.4 Conclusion and interpretation . . . . .     | 105       |
| 4.2 AQ And . . . . .                              | 106       |
| 4.2.1 PACS and SPIRE observations . . . . .       | 106       |

---

|         |   |            |
|---------|---|------------|
| 4.2.2   | Photometry and flux determination . . . . . | 111        |
| 4.2.2.1 | Black body estimation . . . . .             | 114        |
| 4.2.3   | Model fitting with DUSTY . . . . .          | 116        |
| 4.2.4   | Conclusion and interpretation . . . . .     | 126        |
|         | <b>Bibliography</b>                         | <b>130</b> |
|         | <b>Curriculum vitae</b>                     | <b>131</b> |

# 1 Introduction to AGB-stars

In chapter 1.1 an overview of the key features and effects of AGB-stars is given. For the interested reader the study of AGB-stars should be addressed to explain the importance of this evolution because our sun will undergo the similar fate.

The evolution of a  $1 M_{\odot}$  and  $5 M_{\odot}$  star to a carbon star is described in detail. Last but not least the introduction in chapter 1.3 gives the reader the relation of dust and mass-loss.

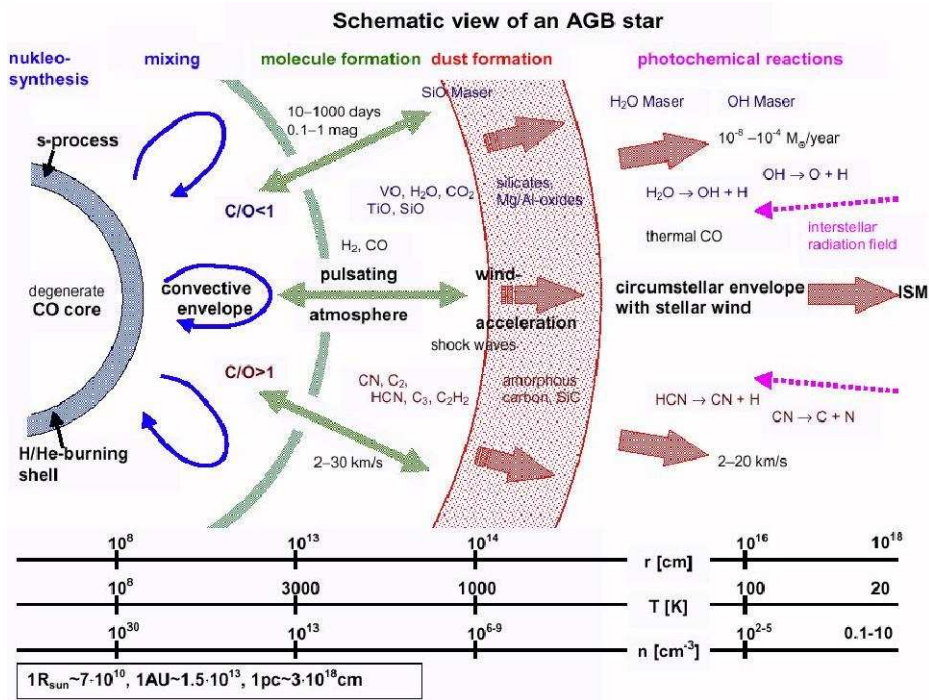
## 1.1 AGB-stars in general

A detailed introduction to AGB-stars can be found in the book “Asymptotic Giant Branch” stars from editors Harm J. Habing, Hans Olofsson and their contributors, A&A Library, publisher: Springer, [Harm J. Habing, 2003], which is the basis of this introduction.

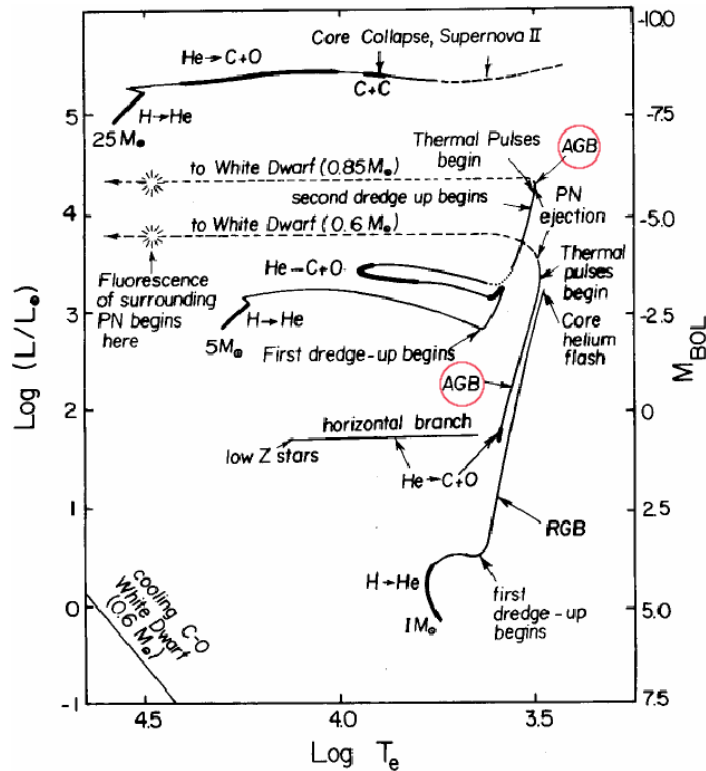
The term Asymptotic Giant Branch (AGB) is commonly used for stars with mass between  $0.8 M_{\odot}$  and  $8 M_{\odot}$  [Karakas, 2010], which are approaching asymptotically the red giant branch of the Hertzsprung-Russell Diagramm (HRD, Fig. 1.1(b)). A detailed description of the evolution can be found in chapter 1.2.

Their structure consists of four parts (Fig. 1.1):

- (1) a core: small, dense, hot
- (2) a stellar envelope: large, less dense, hot
- (3) a thin, warm atmosphere
- (4) a very large, very thin, and cool circumstellar envelope.



(a) Typical structure of an AGB-star with density, stellar radius and temperature scale, [Hron and Le Bertre, 2012].



(b) Hertzsprung-Russell diagram (HRD). Luminosity or  $M_{bol}$  versus effective temperature of the star, [Iben, 1985, Kaler, 2001]. The red circle indicates the Asymptotic Giant Branch (AGB) for a 1 and 5  $M_{\odot}$  star.

Figure 1.1: Structure (Fig. 1.1(a)) and evolution (Fig. 1.1(b)) of an AGB-star.

Until there is only carbon and oxygen left in the core ( $0.5 - 0.9 M_{\odot}$ , [Lattanzio and Wood, 2000]), the He-burning zone moves to the shell and the core contracts to white dwarf densities. In this phase the star reaches a temperature of  $10^8$  K and a diameter of  $10^6$  m. Because of the He-shell-burning, the expansion of the envelope and the contraction of the core, a rapid increase in luminosity rings up the early-AGB (E-AGB) phase. In this phase the dominant energy production is placed in the He-burning shell besides the H-burning shell (stellar envelope: 3000 K,  $10^9$  m), where the stars begin to pulsate on a timescale of about hundred to thousand days.

In the stellar atmosphere the formation of molecules is benefited because the outer part of the stellar envelope is cool. Furthermore the atmosphere is very extremely extended to several hundred  $R_{\odot}$  with a ratio of the radius of the atmosphere to the stellar radius ( $\Delta R/R$ ) of  $\approx 1$  in contrast to our Sun with  $\Delta R/R \approx 4 \cdot 10^{-4}$ .

The stellar wind transfers mechanical energy through the pulsation to the outer part, thus the star will extend more and more because of the mass-loss. The interaction with the interstellar medium (ISM) builds up a shock front, where there is the possibility in the post-shock region to form up dust grains and molecules.

Through a slow wind of  $\approx 15 \text{ km s}^{-1}$  of an AGB-star, the circumstellar envelope (CSE) or shell, which consists of gas and dust particles, can form up and shows us structures like shells and arcs. Their radii and width are dependent on their resistance against UV-photons. The gas part is mostly  $\text{H}_2$ , farther away CO and the dust grains will survive better than the molecules because of their properties (large opacities) and C/O-ratio (see AGB-star classification). The AGB-structure terminates at the contact with the ISM at  $T = 10 \text{ K}$ ,  $n = 10 \text{ cm}^{-3}$  and a distance of  $10^{16} \text{ m}$  ( $6.7 \times 10^4$  Astronomical Units (AU)).

The CSE is detectable as weak IR-excess above the stellar flux, when the AGB-star has a low mass-loss rate. A higher mass-loss causes an obscuration of the star, which can be observed as low-temperature, high-luminosity phenomenon, and appears similar to a protostar. There are spectral features too, which come from the different C/O-ratio as well as from solid particles and microscopic grains around the AGB-star. Furthermore deeper investigations show circumstellar atomic and molecular species. Additionally one can get kinematic information out of the spectral line as well as historical information about the evolution of the AGB star (e.g. mass-loss).

### Classification of AGB-stars

The classification of AGB-stars is divided in three types; M, S, C. These types reflect the dominating molecules found in the spectra. TiO, VO,  $\text{H}_2\text{O}$ , SiO, OH,  $\text{CO}_2$  for M-stars, carbon molecules ( $\text{C}_2$ , CN, HCN, CS) in C-star-spectra and ZrO molecules in S-stars. The C/O-ratio provides here the division between oxygen-rich ( $\text{C/O} < 1$ ) and carbon-rich stars ( $\text{C/O} > 1$ ) for the stellar surface. CO has a high dissociation energy of 11.1eV and so its formation is favoured. Furthermore this molecule acts as switch between the atmospheric chemistries. In M-stars all carbon is bound in CO and thus the remaining

oxygen is free for the formation of oxygen-rich-molecules like TiO, VO, OH, CO<sub>2</sub> and more. In the case of C-stars all oxygen is associated in CO and so carbon molecules like C<sub>2</sub>, CN, HCN can be built up.

The ISM and “normal” stars are enriched with C/O-ratios  $< 1$ , that makes C-stars peculiar, where the extra carbon was added, which occurs during the third dredge-up, where the convective zone reaches layers with processed material (see chapter 1.2). In addition it is assumed that S-stars (C/O  $\sim 0.95 - 1$ ) are a short-lived evolutionary phase between M- and C-stars by convective mixing of carbon up into the atmosphere during the dredge-up events [Jorgensen, 1994].

### Double-shell burning, thermal pulses and dredge-up events

When the star arrives at the tip of the Red Giant Branch (RGB) ( $M_{\text{bol}}=-4$ ,  $L=3000L_{\odot}$ ), it starts H- and He-burning in the shell and a thin He-layer around the core turns quickly into carbon, which afterwards belongs to the core’s mass. In a short period the star modulates its luminosity, which is called “thermal pulse” or “He-shell” flash. The hydrogen burning in the star is activated between thermal pulses (TP), and so there is a temporary He- and H-burning, which is known as “TP-AGB phase”.

The (third) dredge-up explains the surface enrichment with s-process elements [Herwig, 2005] (neutron capture with consecutive beta-decay) like ZrO, TiO, technetium [Little-Marenin, Little, 1979], which are produced in the interior of the star (in the intershell regions) in a slow irradiation process with neutrons at  $10^8\text{K}$ . Hybrid stars with TiO and ZrO bands are called MS-stars, which evolve first as oxygen-rich stars and after the third dredge-up with additional s-process elements. The same feature is possible in C-stars together with s-process elements, which lead to SC-stars. Another important element in the AGB-atmospheres is technetium, which can be used as a tracer of the internal production of new elements and for dredge-up events [Eggleton, Dearborn, 2008, Stancliffe, 2010], because <sup>99</sup>Tc isotopes are half-decomposed in  $\sim 2 \times 10^5$  years.

### Variability

The long-period variation (LPV) in their light curves is an important feature when talking about AGB-stars, which are divided in 4 different types of LPV in the General Catalogue of Variable Stars (GCVS).

The main 4 LPV classes are:

- Mira-like (“M”),  
with regular variations with a large amplitude in V-Band (mean wavelength: 540 nm) ( $\Delta V > 2.5$ ) with periods of 80 to 1000 days.
- Semiregular of type a (“SRa”),  
which are almost regular with smaller amplitude in V ( $\Delta V < 2.5$ ) and periods similar to Mira-types.

- Semiregular of type b (“SRb”) with poorly defined periodicity ( $\sim 20$  to 2300 days) and alternating intervals of periodic and slow irregular changes (also multi periods possible) with smaller amplitude in  $V$  ( $\Delta V < 2.5$ ).
- Irregular (“L”), irregular light curves with low amplitude, and for insufficiently studied stars.

The light curves are often not sharp, especially in the optical, therefore it is not so easy to distinguish between the different classes. Furthermore there are multi-periods and complex periods possible.

### AGB stars as probes

Globular clusters with low metallicity are excellent test labs for AGB stars, because the cluster members have the same distance to our solar system, the same chemical composition, but different masses and thus a different evolution. Its HRD can give us information about the position of the tip of the RGB and other branches like RGB, Horizontal Branch (HB), and more to study the evolution of the stars.

Furthermore AGB-stars are excellent test laboratories because they are luminous, thus easily detectable in our Galaxy and in galaxies until 10 Mpc, and they are set in the late-stage of the stellar evolution, which can show us the star formation history and the galactic structure and dynamics as well as the contribution of heavy elements to the ISM.

To identify an AGB-star on the basis of its position in the HRD (Fig. 1.1(b)), its initial mass has to be close to the turnoff masses in globular clusters of  $\sim 0.85 M_{\odot}$ . Furthermore it is assumed that red variables with large amplitude near the tip of the AGB are AGB-stars.

With the help of the LPVs in the irregular dwarf galaxies, the “Large and Small Magellanic Clouds” (LMC, SMC) [Lebzelter, 2008, Lederer, 2009], it is possible to derive the absolute magnitude based on the known distance. In addition pulsation periods together with luminosity can provide the P-L relationship to determine the AGB mass and  $M_{\text{bol}}$  limit.

Furthermore the AGB and RGB are separable through absolute magnitudes and colours. When the star is more luminous than the tip of the RGB, then it must be an AGB-star (or supergiant), but below the tip the photometry fails here, so it must be verified with other properties like thermal pulses, elemental abundances and others.

It is difficult to detect a thermal pulse during its high luminosity phase at the beginning, because the probability to observe its spike is low. So it is better to measure the follow-up events after the spike like the detection of s-elements (e.g. Zirconium (Zr)) or

the surplus of carbon or nitrogen. Another check is to look after the element lithium (dredge-up product) or technetium (Tc)-lines (recent dredge-up, half life of Tc-isotope is  $\sim 2 \cdot 10^5$  yr).

A second method is to derive linear relations between K-magnitude and  $\log P$  (period) and therefore to check for TP-AGB stars. Most TP-AGBs are similar to Mira stars, like a long period and an average  $M_{\text{bol}} < -3.9$ .

Mass-loss, as third feature, can be used to check for a special mass-loss rate of  $10^{-7} M_{\odot}$  per year, which indicates that these stars are AGB stars and LPV. The conclusion that all these stars are TP-AGB stars, suits for a majority of the stars, but not for all and the LPV supports this assumption.

### Termination of the AGB

When the mass-loss rate is higher than the growth rate in the core and mass-loss is the dominant process in the evolution, the endpoint of the AGB-phase is reached and will pass over to the post-AGB branch ( $\approx$  envelope mass  $< 0.01 M_{\odot}$ ).

The duration of the post-AGB phase is a few 1000 years, after that for a few 100 years it will transit into its final stage “a planetary nebula”, which will expand and become thinner and thinner and only the inner part “the white dwarf” will be left behind.

| AGB-star characteristics               |                       |
|--|-----------------------|
| stellar radius [ $R_{\odot}$ ]         | 200 – 600             |
| $T_{\text{eff}}$ [K]                   | 2000 – 3500           |
| $M_{\text{bol}}$ [mag]                 | $\sim 0$ – -7.5       |
| luminosity [ $L_{\odot}$ ]             | 100 – 10000           |
| mass-loss rate [ $M_{\odot}$ per year] | $10^{-8}$ – $10^{-4}$ |
| period [days]                          | 30 – 2800             |

Table 1.1: Typical properties of AGB-stars



## 1.2 Evolution to carbon stars

Evolution to the E-AGB at  $M \sim 1 M_{\odot}$

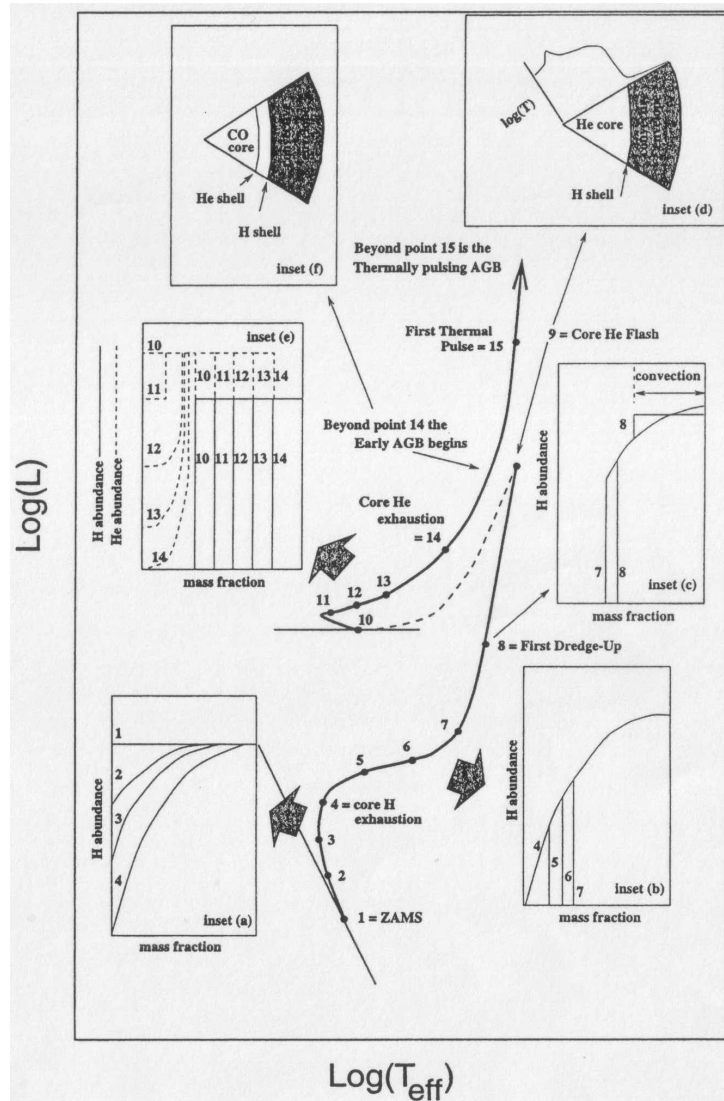


Figure 1.2: Typical AGB-star evolution with initial mass of  $1 M_{\odot}$ , luminosity vs. effective temperature on a logarithmic scale., [Lattanzio and Wood, 2000]

First the fusion process  $\text{H} \Rightarrow \text{He}$  (“H-burning”) [Izzard, 2007, Karakas, 2008] takes place on the zero age main sequence (ZAMS). As a consequence of the increasing molecular weight due to this process, the central temperature as well as the density increase until the central H-exhaustion is reached (Fig. 1.2 points 1-4). At the points 5-7 the star leaves the ZAMS to transit to the Hertzsprung gap, where H-burning is started in the shell, which surrounds the electron degenerated He core.

During this phase the hydrostatic equilibrium between gravity and gas pressure forces the star to expand and convection occurs in the outer layers. The convection envelope pushes forward to the H-burning regions deeper in the star, so the material will mix up and reach the surface, also called “first dredge-up” (point 8), where  ${}^4\text{He}$ ,  ${}^{14}\text{N}$  and  ${}^{13}\text{C}$  will be enriched on the surface.

After that the He core starts to degenerate and contracts, which causes the temperature maximum to move upwards. The triple- $\alpha$  process ( $3\alpha$ ; He-burning; three He-cores merge to carbon and oxygen) will start a violent event termed as “helium core flash” (point 9) [Iben, 1968, Thomas, 1967], where helium is ignited at  $T_{\text{max}} \sim 10^8$  K. Because of this ignition the star quickly reaches the Horizontal Branch (HB) (low metallicity:  $M < 1 M_{\odot}$ ) or the red giant clump (solar abundance). In points 10–13 in the HB He-core burning and H-shell burning occurs. In the convective core He is converted to carbon and oxygen and in the outer regions convection and semiconvection occurs [Castellani, Giannone, Renzini, 1971].

After the depletion of He (point 14) the star climbs up the giant branch again and the energy production is dominated by the He-burning shell, which lies between the degenerating core and the H-burning shell, whereas the outer layers are in the semi-/convective phase. Here the early-AGB begins.

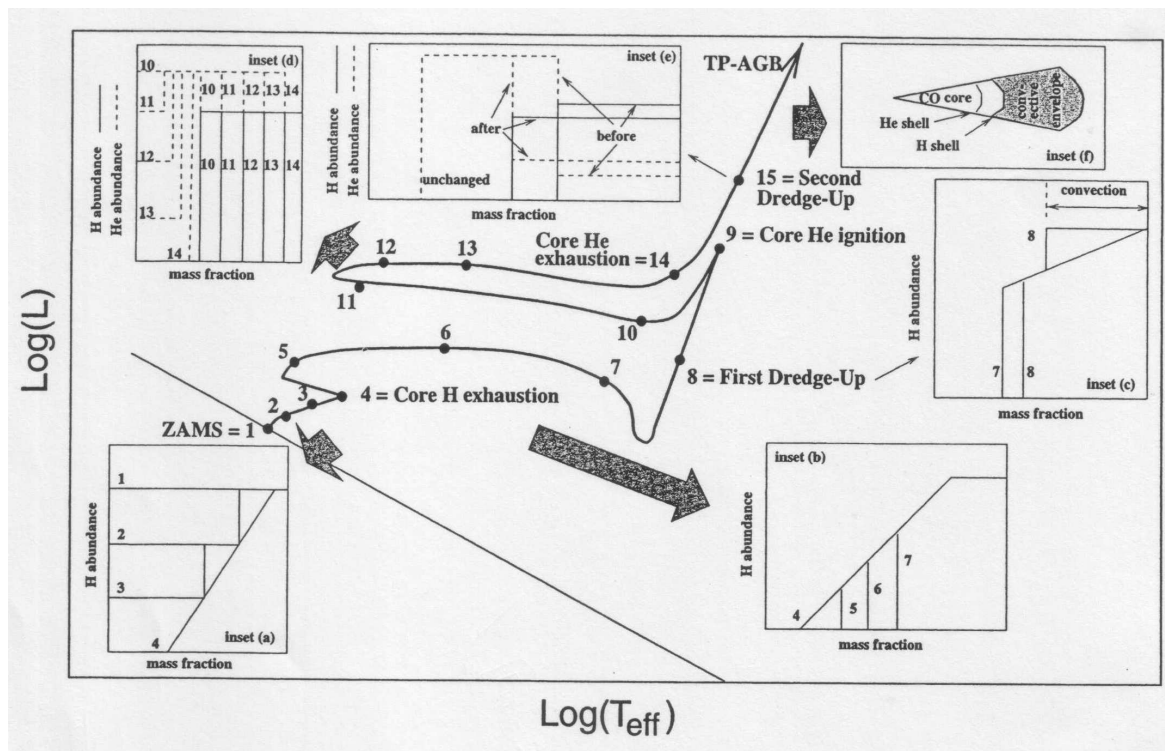
Evolution to the E-AGB at  $M \sim 5 M_{\odot}$ 

Figure 1.3: Typical AGB-star evolution with initial mass of  $5 M_{\odot}$ , luminosity vs. effective temperature on a logarithmic scale, [Lattanzio and Wood, 2000].

At  $5 M_{\odot}$  (Fig. 1.3) the star can burn hydrogen in the CNO cycle ( $^{12}\text{C}$  as catalyst for the creation of helium), because the temperature is high enough, which leads to a convective core. Through electron scattering, which is proportional to the H amount, the opacity decreases and so the core extension is stopped (points 1–4). Like in the  $1 M_{\odot}$ -case the core is depleted of hydrogen and moves to the Hertzsprung gap (points 5–7). Furthermore similar to  $1 M_{\odot}$  at point 8 the first dredge-up enriches the stellar surface with  $^{13}\text{C}$  and  $^{14}\text{N}$ .

Because of the higher mass, the ignition of He starts at the centre without any degeneration and burns helium in its convective core, along with H-burning in the shell. Also the Cepheid instability strip is reached during points 10–14. Like hydrogen, helium is exhausted in the core and He-shell burning begins with the result of a strong expansion. So the H-burning shell is turned off and the star evolves along the evolution to the AGB. The occurrence of a “second dredge-up” changes the composition of the surface again ( $^4\text{He}$ ,  $^{12}\text{C}$ ,  $^{14}\text{N}$ ) and alters the mass of the H-depleted core with new H. Only stars heavier than  $4 M_{\odot}$  have a “second dredge-up”, otherwise the core will not be reached. When the H-shell is reignited, the evolution of the AGB proceeds.

### Further stellar evolution on the AGB

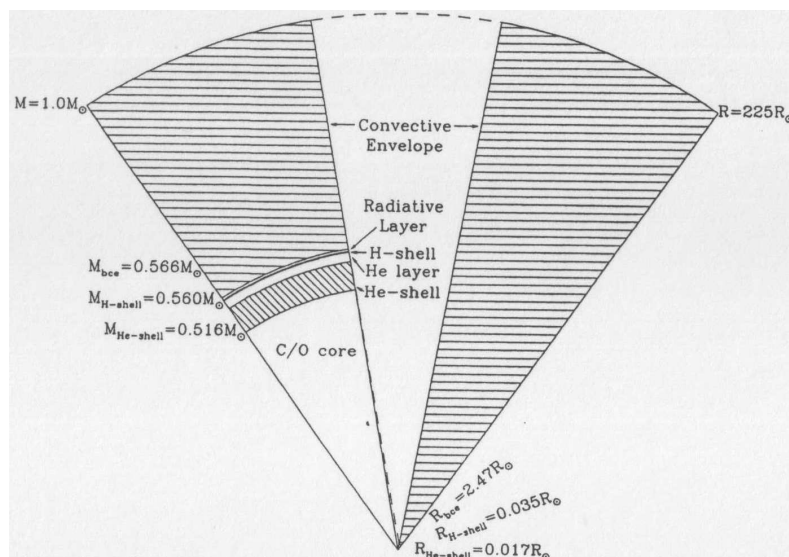


Figure 1.4: Schematic view of an AGB-star with initial mass of  $1 M_{\odot}$ , [Lattanzio and Wood, 2000]

left: Plot of the mass fraction, right: Plot against the radius;

$M_{\text{bce}}$  ... mass at the base of the convective envelope,

$M_{\text{H-shell}}$  and  $M_{\text{He-shell}}$  ... masses at the middle of the burning-shells.

Fig. 1.4 shows a typical AGB-star structure with  $1M_{\odot}$ , where H- and He-shell-burning is active simultaneously. The interior structure consists of an oxygen-carbon core with a H- and He-burning-shell around it and a convective envelope with pulsation. The CO-core is degenerated, so that no carbon burning can take place in the centre and the cooling is only possible through neutrino emission. Furthermore the degeneration of the core sets the upper mass limit of AGB-stars at  $\sim 8 M_{\odot}$ .

The centre to the H-shell structure contains approximately the half of the mass of the  $1M_{\odot}$  star and the volume of the core is very tiny compared to the convective envelope, and the core will be similar to the end phase of its evolution as white dwarf ( $0.5 - 0.85 M_{\odot}$ ) [Lattanzio and Wood, 2000].

The core is here the main interesting part for the evolution of the star because the nucleosynthesis processes take exclusively place in the centre.

During the early AGB-phase there are luminosity variations in the H- and He-shells because of thermal instabilities [Schwarzschild, Härm, 1965, Weight, 1966]. The He-shell burns through the thick helium layer (Fig. 1.4), which was the result of the H-burning shell during the core He-burning phase, when low luminosities between  $100$  and  $1000 L_{\odot}$  ( $1M_{\odot}$  star) occur. So the He-burning dominates at the luminosity of the star. During

the burning process the He-layer gets thinner, so the H-burning shell increases its luminosity. These procedure can change again in a short time, as oscillations in luminosity, which it indicates the TP-AGB phase.

As a physical explanation, a positive temperature perturbation [Schwarzschild, Härm, 1965] can take place in the He-shell, which leads to an increase in the nuclear energy production (energy rate  $\varepsilon \propto \rho^\mu T^\nu$ ) as well as an energy loss from the shell because of additional temperature gradients upcoming from the shell centre to the edge.

The increasing of the energy production overtakes the energy loss and generates a thermal instability. In the triple- $\alpha$  process large  $\nu$  values (20 – 40 at  $\mu = 2$ ) ensure that the energy production can raise at modest temperature disturbances. On the other side the energy loss can be explained through the thickness of the shell, where a thin shell holds back the loss.

Furthermore the energy production must be a thermal runaway process to enhance the increase of temperature, which occurs in a perfect gas at constant pressure.

The main aspect of the He-shell instability shows the high temperature-dependence coupled together with the low thickness of the shell.

### Surface Luminosity Variations

At the beginning of the plots (early-AGB, Fig. 1.5) the H and He luminosities are equal before reaching the TP phase.

With each thermal pulse the luminosity is growing until a maximum luminosity is reached. After a typical lifetime on the AGB of several  $10^6$  years, the H-rich convective envelope has lost all its material through the mass loss and the post-AGB phase starts.

After a thermal pulse (shell flash) there is a slow recovery pause, called “quiescent evolutionary phase”, which is defined as the interval between a thermal pulse and the reach of the “quiescent” luminosity maximum. When the luminosity is decreasing, the He-shell-burning dominates, in the recovery phase the H-shell-burning is the main energy production in the shell layers.

He burns very rapidly up to  $\approx 10^6 L_\odot$ , which leads to hydrostatic readjustment of the shell structures (expansion), and turns off the H-shell-burning immediately. The drop in luminosity is shown as dashed line in Fig. 1.6 in the right panel.

After this He-shell peak, a second, weaker He-shell flash is drawn in the dotted line (oscillation peak), which originates from the deposited energy in the stellar core. These characteristics are valid for  $1 M_\odot$  until  $2.5 M_\odot$  stars and  $5 M_\odot$  stars with envelope mass below  $1.5 M_\odot$ . In AGB-stars with higher stellar envelope masses than  $1.5 M_\odot$  and stars more massive than  $5 M_\odot$ , the stellar envelope reaches the H-shell deeply, so the variation in luminosity during the TP-AGB phase is weak but with more thermal pulses.

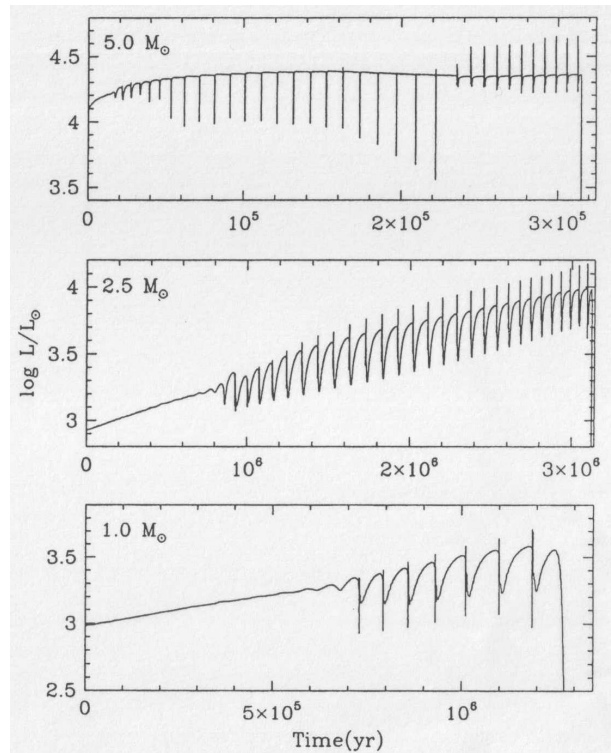


Figure 1.5: Luminosity variations; early-AGB until the end of the TP-AGB,  $1M_{\odot}$ ,  $2.5M_{\odot}$ ,  $5M_{\odot}$  with initial composition  $Y=0.25$  and  $Z=0.016$ , [Lattanzio and Wood, 2000, Vassiliadis, Wood, 1993].

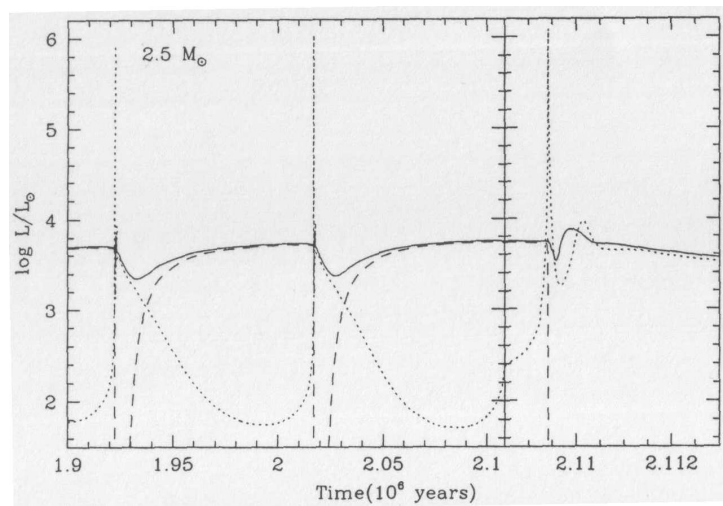


Figure 1.6: Fully developed TP for a  $2.5 M_{\odot}$  star with surface luminosity (solid line), H-burning luminosity (dashed) and He-burning luminosity (dotted), [Lattanzio and Wood, 2000].

### The interaction of evolution and pulsation

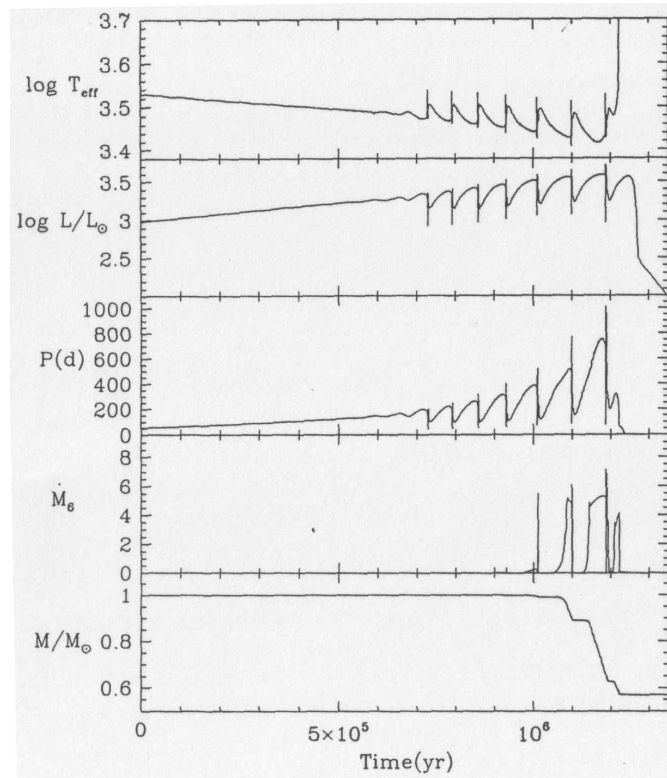


Figure 1.7: Different properties of a  $1 M_{\odot}$  star (initial composition:  $Y=0.25$ ,  $Z=0.016$ ):  $\log T_{\text{eff}}$ ,  $\log (L/L_{\odot})$ , pulsation period  $P$  in days, mass-loss in units of  $10^{-6} M_{\odot} \text{ year}^{-1}$ , [Lattanzio and Wood, 2000].

The pulsation period relation  $P \propto R^{\alpha} M^{-\beta}$  with  $\alpha \approx 1.5 - 2.5$ ,  $\beta \approx 0.5 - 1.0$  [Fox, Wood, 1982, Wood, Mennessier, Omont, 1990] shows that the change in luminosity varies the stellar radius and mass, which in turn alters the pulsation period.

In Fig. 1.7 the time variation of the fundamental mode period of a  $1 M_{\odot}$  star is shown, where the period begins to grow rapidly at  $\sim 10^6$  years with presence of the “superwind”. When the mass decreases, the effective temperature of the AGB-star decreases as well. Another fact is the mass dependence, which leads to a high mass loss of the superwind. More massive stars have higher mass loss rates due to these relations and thus longer periods ( $> 1000$  days), which form up a circumstellar envelope with gas and dust grains [Herman, Habing, 1985, Wood, Whiteoak, Hughes, 1992].

### The third dredge-up: Making carbon stars

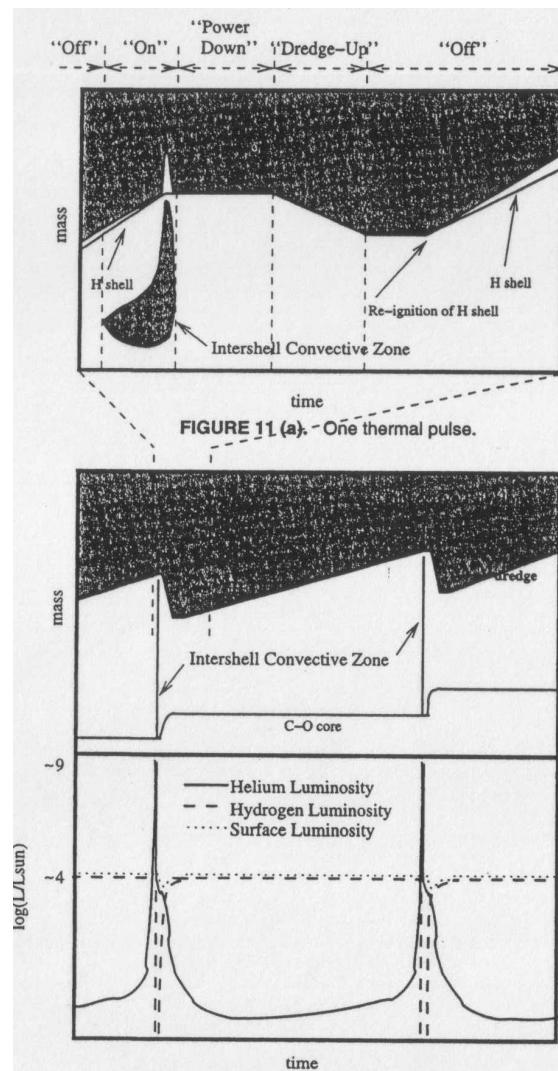


Figure 1.8: Interior evolution during a thermal pulse, [Lattanzio and Wood, 2000].

Fig. 1.8 illustrates the evolution of the thermal pulse phase with quantities of luminosity and mass together with H- and He-shell-burning [Iben, 1975, Sugimoto, Nomoto, 1975]. There are four phases known in a thermal pulse cycle [Iben, Renzini, 1981]: “Off”, “On”, “Power Down”, “Dredge-up”.

In the “Off”-phase the He-burning shell is nearly inactive, that’s why the H-burning shell dominates. The “On”-stage indicates the active phase of the He-shell ( $\approx 10^8 L_{\odot}$ ), where a convective shell above the He-region establishes because the radiation cannot be transported through radiation transport alone. This convective shell, which consists of about 75% He and  $\approx 22\%$  carbon, expands to the H-shell. Its lifetime is highly core



mass dependent and is estimated to be a few hundred years. After that in the “Power Down”-phase the He-shell burns less helium and the intershell vanishes too. The energy from the previous phase broadens the intershell regions and so pushes the H-shell. So the temperature and the density of the H-shell is decreasing and powers down.

In the last phase “Dredge-up”, the produced energy from the shell flash increases the luminosity in the core, which in turn heats up the convection zone, which expands into the intershell region. Because of that the material( $^{12}\text{C}$ ) from the He-burning in the shell will mix up with the stellar surface, called “third dredge-up”. An effective dredge-up parameter is defined as  $\lambda = \Delta M_{\text{dredge}} / \Delta M_{\text{c}}$ .

( $\Delta M_{\text{dredge}}$  ... mass, dredged up by the convective envelope in one TP,

$\Delta M_{\text{c}}$  ... mass, which was moved by the H-shell during “Off” phase).

$\lambda = 0$  : early flashes,  $\lambda \lesssim 0.3$  for lower mass stars ( $\lesssim 2.5 M_{\odot}$ ),  $\lambda \lesssim 1.0$  ( $M \gtrsim 5 M_{\odot}$ ): strong thermal pulses.

Unfortunately values of  $\lambda$  are uncertain, because the determination of the convective mass  $\Delta M_{\text{dredge}}$  is difficult.

| $M_i$           | $M_f$           | $M_{\text{bol}}$ | $t_{\text{MS}}$ | $t_{\text{EAGB}}$ | $\frac{t_{\text{EAGB}}}{t_{\text{MS}}}$ | $t_{\text{TPAGB}}$ | $\frac{t_{\text{TPAGB}}}{t_{\text{MS}}}$ |
|-----------------|-----------------|------------------|-----------------|-------------------|---|--------------------|--|
| [ $M_{\odot}$ ] | [ $M_{\odot}$ ] |                  | [Gyr]           | [Myr]             | [%]                                     | [Myr]              | [%]                                      |
| Z=0.016         |                 |                  |                 |                   |   |                    |  |
| 1.0             | 0.57            | -4.0             | 11.3            | 12                | 0.16                                    | 0.50               | 0.004                                    |
| 1.5             | 0.60            | -4.5             | 2.7             | 9.2               | 0.34                                    | 0.83               | 0.03                                     |
| 2.0             | 0.63            | -4.9             | 1.2             | 7.9               | 0.66                                    | 1.20               | 0.10                                     |
| 2.5             | 0.67            | -5.1             | 0.62            | 1.1               | 0.18                                    | 2.20               | 0.35                                     |
| 3.5             | 0.75            | -5.7             | 0.23            | 2.8               | 1.2                                     | 0.43               | 0.19                                     |
| 5.0             | 0.89            | -6.2             | 0.10            | 1.2               | 1.2                                     | 0.26               | 0.27                                     |
| Z=0.004         |                 |                  |                 |                   |   |                    |  |
| 1.0             | 0.59            | -4.5             | 6.7             | 8.0               | 0.12                                    | 0.87               | 0.01                                     |
| 1.5             | 0.64            | -4.9             | 2.1             | 6.3               | 0.30                                    | 0.97               | 0.05                                     |
| 2.0             | 0.67            | -5.2             | 0.89            | 6.7               | 0.75                                    | 1.60               | 0.18                                     |
| 2.5             | 0.69            | -5.5             | 0.46            | 5.2               | 1.1                                     | 1.30               | 0.27                                     |
| 3.5             | 0.85            | -6.0             | 0.18            | 2.2               | 1.2                                     | 0.25               | 0.14                                     |
| 5.0             | 0.94            | -6.5             | 0.08            | 0.6               | 7.3                                     | 0.31               | 0.39                                     |

Figure 1.9: Typical model predictions; time scales for main sequence-, early-AGB-, and TP-AGB-stars, [Lattanzio and Wood, 2000], [Vassiliadis and Wood, 1993].

A summary of AGB time scales is shown in Fig. 1.9, [Vassiliadis and Wood, 1993]. These data are obtained from sets of AGB-stars with known distance near the Galactic centre and the Magellanic clouds.

## 1.3 Dust and mass loss

Dust consists of small solids, which have a 3D-internal structure with 2D surfaces [Sedlmayr, 1988] and condensed from atoms/molecules at  $\sim 10 - 100$  K. Only about 10% of the circumstellar dust is crystalline, which is the energetically most favourable configuration.

The formation of dust begins with bounding of atoms and molecules ( $\sim 0.1$  nm) to clusters. Clusters ( $\sim 1$  nm to 10 nm; 3 to 50.000 atoms) are a transition state of dust grains and start to show collective phenomena like absorption and reflectance features and electromagnetic properties like electric conductivity and ferro-magnetism. The resulting dust grains have a size of  $\sim 10$  nm to several  $1 \mu\text{m}$ .

For the growth of a particular dust species, it is necessary that its predecessor atoms are abundant and that thermodynamic stability is given. In addition an efficient reaction pathway is a mandatory precondition.

To obtain information on the properties of dust, there are different methods to analyse dust.

The most promising method uses meteorites and comet debris after earth entry to extract information of structure, abundance and further properties with electron microscopes and mass spectrometry. Furthermore the comparison of thermodynamical and chemical calculations of synthetic spectra, and astronomical (infrared) spectra gives us a theoretical overview of the properties of dust grains.

In C-stars (C/O ratio  $> 1$ , non-solar) the dominated species is amorphous carbon, which has no crystalline structure. Carbides like titanium carbide (TiC), silicon carbide (SiC), and sulphides such as magnesium sulphide can also be found.

Silicates like crystalline forsterite ( $\text{Mg}_2\text{SiO}_4$ ), crystalline enstatite ( $\text{MgSiO}_3$ ), amorphous olivine ( $\text{Mg}_2\text{Fe}_2\text{SiO}_4$ ) and amorphous pyroxene ( $\text{Mg}_x\text{FeSiO}_3$ ) are mainly produced at M-stars (C/O ratio  $< 1$ , solar) [Ferrarotti, Gail, 2003].

The main functions of dust in the ISM and in circumstellar shells are described as followed.

- Thermodynamic as redistribution of the radiation energy from short to long wavelengths (e.g. from the ultra-violet and the visual to the infrared) and dust acts as cooling agent.
- Chemical reactions; Dust grains support chemical reactions as catalysts because of their surfaces. Simple molecules like  $\text{H}_2$  cannot form without dust grains.
- Hydrodynamic effects like taking up momentum from the radiation field [Wickramasinghe, 1966, Gehrz, Woolf, 1971, Gauger, 1990] and emitting it to the surrounding environment gas to act as main driver for mass-loss with only 1% of the mass, because the opacity of dust grains is 10 000 times larger than the opacity of the comparable gas mass [Gustafsson, Höfner, 2004].

Mass loss is an essential process to learn more about AGB-stars and their properties, because it stops the evolution on the AGB due to the material loss. The dependence of mass loss on the stellar properties is only poorly understood, but there are recent studies with a combination of pulsation and radiation pressure involving dust grains [Wood, 1979, Bowen, 1988]. When the luminosity of the star is rising, the mass loss is increasing rapidly too (Fig. 1.7). Furthermore the largest mass loss [numerical approaches, Woitke, 2003] occurs in the quiescent evolution phase during the luminosity peaks (from thermal pulse to thermal pulse increasing) because of the short duration.

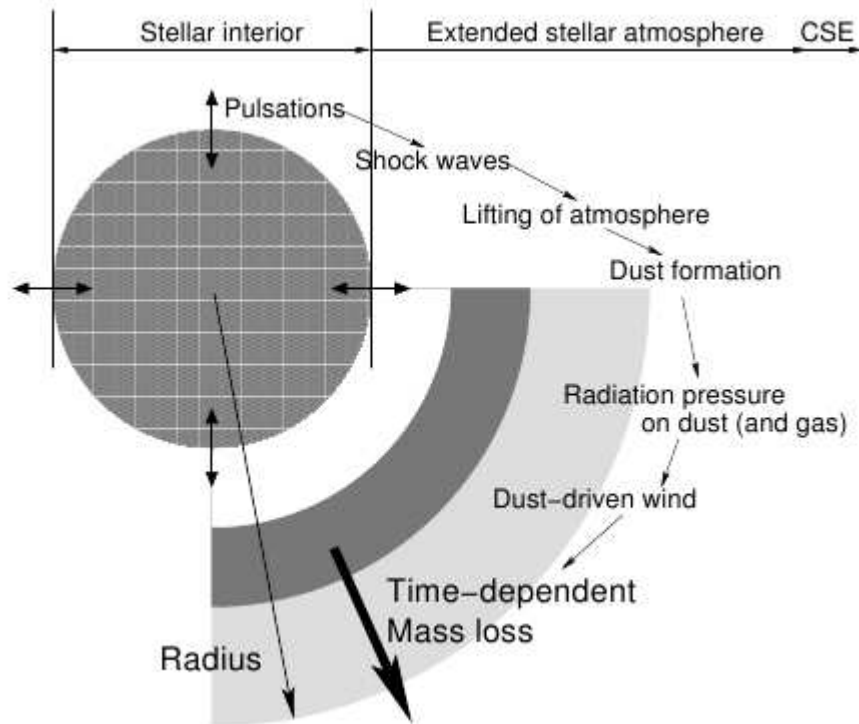


Figure 1.10: Schematic overview of the stellar atmosphere and CSE with important mass loss processes for driving a stellar wind. Image from C. Sanders, Sandin

To discuss the processes, which are responsible for mass loss, the stellar atmosphere and the ambient material are divided into three zones:

- Zone A: “Innermost layers of the extended stellar atmosphere”
- Zone B: “Transition region with a complex, time-dependent structure”
- Zone C: “Circumstellar envelope”

In Zone A the density is decreasing exponentially and the hydrostatic atmosphere is sending out shock waves due to the pulsation (approximately ballistic outflow of gas). Stellar pulsation levitates the outer atmospheric layers and increases the density, and the radiation pressure on the dust grains converts the stellar radiation into momentum. At the CSE the final wind velocity is reached and its density distribution is almost stationary proportional to  $r^{-2}$  (simple model).

The interzone C sets the condition for mass loss by acceleration of the wind.

### Driving mechanism

To drive a stellar wind a source of momentum is required to overcome the gravity force, which binds the gas to the star. Two types of winds are distinguished:

#### (1) Thermal winds

The gradient of gas pressure drives the wind with high pressure originating from the dissipation of sound waves and by radiative heating of gas.

#### (2) Radiation-driven winds

Outward-directed radiation is absorbed and re-emitted in all directions through photons and these process accelerates the radiation-driven wind.

Other accelerating mechanisms for wind from stellar surfaces are sound waves, shocks and magneto-hydrodynamic waves. These processes are almost inefficient, but they are the dominant contributor to create thermal winds due to heating and decreasing of gas pressure, and also for radiation-driven winds, by which molecules and dust grains can be form because of the enhancement of the density of the outer atmosphere.

### Characteristics of AGB-star winds

The typical wind velocity of AGB-stars ranges from 10 to 20 km s<sup>-1</sup>. In these outflows a common component is dust, which condensates in dust grains and thus the wind is driven by radiation on the dust grains.

An important characteristic parameter of mass loss is the ratio of momentum from the wind outflow to momentum of the radiation field, written as  $\beta$ .

$$\beta = \frac{v_{\infty} \cdot \dot{M}}{L/c} \quad (1.1)$$

$v_{\infty}$  ... terminal velocity of the wind

$\dot{M}$  ... mass loss rate

$L$  ... stellar luminosity

$c$  ... speed of light

An optically thin wind, which is accelerated by the radiation pressure on dust grains, has  $\beta$  values smaller than 1, which is also supported by observations. For optically thick wind,  $\beta$  is greater than 1 because photons and dust grains can interact many times during the outflow.

Although the terminal wind velocity of AGB-stars is slow, the mass loss rate is high ( $\sim 10^{-7}$  to  $10^{-4} M_{\odot} \text{ yr}^{-1}$ , Sun: wind speed:  $500 \text{ km s}^{-1}$ , Mass loss:  $10^{-14} M_{\odot} \text{ yr}^{-1}$ ).

### **Pulsation-enhanced dust-driven winds**

The common mass loss scenario is the combination of the occurrence of shock waves due to pulsation and radiation pressure on dust grains and molecules as driving mechanism of the wind.

During the internal pulsation the outer layers of the star expand, leading to waves in the atmosphere and thus to strong radiating shocks. When the shock wave arrives at the gas, it will be heated up, compressed and pushed outwards. After gathering of a dense gas shell, the temperature drops due to the radiative cooling and the formation of dust grains in the gas is started.

Solid particles (in particular amorphous carbon (AmC) grains) have higher absorption coefficients than gas, so the radiation pressure is more intense. The momentum is transferred outwards by grain-gas collisions and so gas and dust grains arrive at the outer regions. The lower temperature in the outer region favours the condensation of dust grains, but the decreasing gas density slows down the formation of dust.

Furthermore the time-dependent formation, growth and evaporation of dust grains can lead to shell-like structures of the CSE like arcs, detached and attached shells. The mass loss rate increases during the evolution in the AGB phase.



---

## 2 Herschel space observatory

The first part (2.1) of the chapter is primarily concerned with the Herschel telescope's aims and technical structure in general.

In chapter 2.2 the SPIRE instrument as technical part and its data reduction will be introduced and discussed in detail.

### 2.1 Mission overview

The description and images are based on the publication from [Pilbratt et al., 2010] and the Herschel ESA Website, [ESA, 2012a].

#### A little bit of history

In 1993 the Herschel Space Telescope was first discussed as the Far InfraRed and Sub-millimetre Space Telescope (FIRST) (fourth corner-stone of ESA).

In that year the all-sky survey Infrared Astronomical Satellite (IRAS) was started by a US, British and Dutch collaboration and imaged 250 thousand cosmic infrared sources and large areas of extended emission at wavelengths of 12, 25, 60 und 100  $\mu\text{m}$ . As a successor in 1995 ESA launched the Infrared Space Observatory (ISO), which observed 26 thousand science objects in a wavelength range of 2.4 to 240  $\mu\text{m}$ .

NASA launched the Spitzer Space Telescope (all-sky survey) as cryogenically cooled infrared observatory in 2003, which covers wavelengths from 3 to 180  $\mu\text{m}$ .

Out of the cooperation between Japan (JAXA; Japan Aerospace Exploration Agency), Europe (with ESA participation) and Korea arose the AKARI (all-sky survey) infrared telescope in 2003 (wavelength: 1.7 to 180  $\mu\text{m}$ ).

To extend ESA's observations in the infrared and submillimetre-range (55 to 671  $\mu\text{m}$ ) the Herschel Space Telescope, named after the discoverer of the infrared spectrum and planet Uranus, Sir William Herschel, was launched on 14 May 2009 by an Ariane 5 launcher from the Guiana Space Centre, French Guiana, South America (together with the Planck telescope).

The mission lifetime is estimated to be 3.5 years, which depends on the helium consumption of the cryostat. The current (Dec 2011) elapsed time after the launch is 2.6 years, that's why nearly 75 percent of its lifetime is reached.

## Orbit

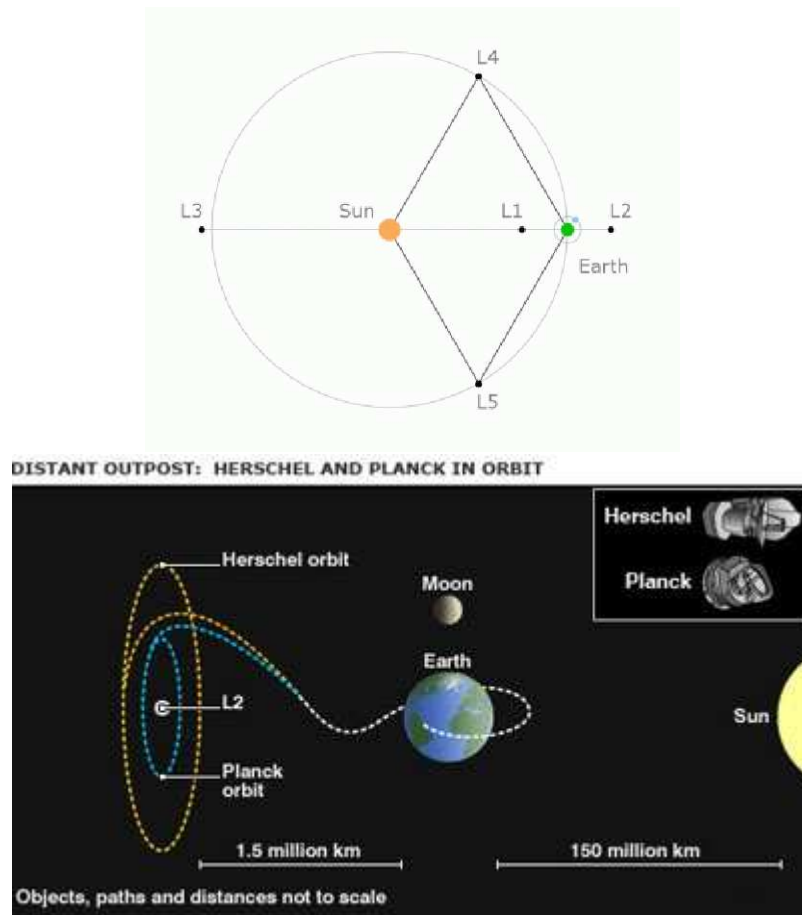


Figure 2.1: Lagrange L2 position of the Sun-Earth-System, [ESA, 2012a].

After a sixty-days journey the Herschel spacecraft reached the Lagrange point (L2) of the Sun-Earth system (Fig. 2.1). The orbit is a large Lissajous motion and so the spacecraft must not perform as many correction manoeuvres as a halo orbit, because of the less momentum change of Lissajous orbits [ESA, 2012a]. The distance varies by 300 thousand kilometres from the Lagrange point 2, respectively 1.2 to 1.8 million kilometres (orbital period about 178 days). Its orbit isn't in the plane of the ecliptic, but a minimal and maximal distance of 500 thousands kilometres below and above the ecliptic. Because of this labile stability point (L2), maintenance manoeuvres are required each month.

A further advantage for choosing this point was the reduction of straylight and thermal sources to reach temperatures below 100 K. That's why a near-Earth orbit was excluded because of the large thermal influence. Further constraints are the line of sight of the telescope, the telecommunications to the ground, the transfer-to-orbit costs and



the shielding against the thermal flux from the Sun, Earth and Moon. So the Lagrange point L2 is the optimal place for Herschel's observations to achieve thermal stability and well-balanced observation time.

The communication of Herschel with earth is managed within three hours per day in 24-hour cycles. In these 3 hours the gathered data can be downloaded as well as new commands and maintenance manoeuvres are executed. The rest of the time is reserved for the science observations. From L2 to earth the two-way communication takes approximately 10 seconds.

The mission is controlled by the Mission Operations Centre (MOC) at the ESA's European Space Operations Centre (ESOC) in Darmstadt (Germany). Further maintenance contact is performed via ESA's New Norcia (Australia) and Cebreros (Spain) stations.

### **Why observing in IR?**

Cooler material (5 to 500 K) like dust in AGB-stars, protostellar objects and dust in galaxies radiates at far-infrared to submillimetre wavelengths. The study of these objects is only possible through the observation of the appropriate infrared spectrum. Objects with a temperature of 5 to 50 K show emission peaks in Herschel's wavelengths as well as gases with 10 K to a few hundred K have their brightest molecular and atomic lines there.

Dust is also present around early-stage stars, AGB-stars and galactic planes, remnants and as dust-molecular clouds. In visible light most of these objects are hidden, enshrouded by the dust, and so observations are inhibited. At infrared wavelengths (1 to 1000  $\mu\text{m}$ ) the efficiency of scattering and absorption in dust clouds is less than in the visible and so the infrared radiation can penetrate the cloud.

### **Herschel's primary objectives**

- Studying the formation of galaxies in the early universe and their evolution
- Study the protostellar objects and their interaction with the interstellar medium
- Observe the chemical composition of the atmospheres and surfaces of comets, planets and satellites
- Investigate the molecular chemistry of the Universe

## Spacecraft and telescope



Figure 2.2: Herschel Space Telescope, artists impression, bottom left: cryo tank with focal plane units inside, bottom right: impressions from the building phase, [Pilbratt et al., 2010], [ESA, 2012a].

The spacecraft (Fig. 2.2, Fig. 2.3) consists of three modular parts; the Payload Module (PLM) with the mirror mounted on the top of cryostat, the sunshield/sunshade and the Service Module (SVM).

The main component in the PLM is the cryostat vacuum vessel (CVV, 1.7 – 4.5 K), which contains the superfluid liquid helium for the cooling purposes. In addition the tank ( $\approx 2367$  litres of helium) is protected against heat loads by three vapour-cooled

| Spacecraft                                |  |
|---|--|
| Size height/width                         | 7.4 / 4.0 m  |
| Mass wet (incl. helium) / dry             | 3400 (335)/2800 kg                                       |
| (incl. telescope/science instruments)     | 315/426 kg   |
| Power total/science instruments           | 1200/506 W   |
| Science data rate (max. average)          | 130 kbps   |
| Solar aspect angle (wrt tel. boresight)   | 60°–110°(120°)   |
| Absolute pointing (68%)                   | ~2"  |
| Telescope                                 |  |
| Primary physical/effective diameter       | 3.5/3.28 m   |
| Secondary diameter                        | 30.8 cm  |
| System/primary f-number                   | 8.70/0.5   |
| Wave front error best-focus (centre/edge) | 4.8/5.5 $\mu\text{m}$                                    |
| Angular resolution                        | $\sim 7'' \times (\lambda_{\text{obs}}/100 \mu\text{m})$ |
| Operational temperature                   | $\sim 85 \text{ K}$                                      |

Figure 2.3: Spacecraft and telescope features, [Pilbratt et al., 2010].

shields, which have the possibility to free the vapour into space. Through a phase separator the liquid can be evaporated into cold gas. On the top of the CVV the optical bench is fixed with the focal plane units (FPU), which houses the three instruments (HIFI, PACS, SPIRE).

The FPUs with the three instruments are connected to thermal pipes with the cryostat tank to supply the required temperatures for the observations at each instrument.

The controlling and communication of the telescope are provided by the warm (295K) electronics on the SVM. This infrastructure handles the attitude and orbit control as well as the instrument control and data reduction, the command execution and much more. Furthermore the SVM provides mechanical (main mechanical load) and thermal stability with the sunshield/sunshade to decouple PLM and SVM.

The requirements of the Herschel telescope were to have a construction (mirror) as large as possible, but it should be light-weight and compatible to the other flight structures and cooling devices. The total wavefront error should not exceed 6  $\mu\text{m}$ , thermal and mechanical stability presumed.

A classical Cassegrain telescope was chosen for the optical part with a primary mirror of 3.5 m and a secondary with 30.8 cm diameter. The entire telescope consists of 90 percent by mass of silicon carbide (SiC). The primary mirror was brazed together out of 12 segments to get a monolithic mirror and the secondary is a single piece of SiC. Both mirrors are polished with aluminium and coated with silicon oxide (“plasil”) to get high reflectivity and low emissivity.

## Onboard Instruments, Fig. 2.4

|   |   |
|---|---|
| HIFI  | Heterodyne spectrometer                           |
| Wavelength coverage                                 | 157–212 & 240–625 $\mu\text{m}$                   |
| Field-of-view (FOV)                                 | single pixel on sky                               |
| Detectors   | 5 $\times$ 2 SIS & 2 $\times$ 2 HEB mixers        |
| Spectrometers                                       | auto-correlator & acousto-optical                 |
| Spectral resolving power                            | typically $10^6$                                  |
| PACS  | 2-band imaging photometer                         |
| Wavelength coverage                                 | 60–85 or 85–130, 130–210 $\mu\text{m}$            |
| Field-of-view (FOV)                                 | $0.5F\lambda$ sampled $1.75' \times 3.5'$         |
| Detectors   | 64 $\times$ 32 & 32 $\times$ 16 pixel bol. arrays |
| PACS  | integral field spectrometer                       |
| Wavelength coverage                                 | 55–210 $\mu\text{m}$                              |
| Field-of-view (FOV)                                 | (5 $\times$ 5 pixel) $47'' \times 47''$           |
| Detectors   | two 25 $\times$ 16 pixel Ge:Ga arrays             |
| Spectral resolving power                            | 1000–4000   |
| SPIRE   | 3-band imaging photometer                         |
| Wavelength bands ( $\lambda/\Delta\lambda \sim 3$ ) | 250, 350, 500 $\mu\text{m}$                       |
| Field-of-view (FOV)                                 | $2F\lambda$ sampled $4' \times 8'$                |
| Detectors   | 139, 88 & 43 pixel NTD bol. arrays                |
| SPIRE   | imaging fourier transf. spectrometer              |
| Wavelength coverage                                 | 194–324 & 316–671 $\mu\text{m}$                   |
| Field-of-view (FOV)                                 | $2F\lambda$ sampled circular $2.6'$               |
| Detectors   | 37 & 19 pixel NTD bol. arrays                     |
| Spectral resolving power                            | 370–1300 (high) / 20–60 (low)                     |

Figure 2.4: Specifications of the onboard instruments, [Pilbratt et al., 2010].

## SPIRE: Spectral and Photometric Imaging REceiver

SPIRE is discussed in chapter 2.2. In addition the publication [Griffin et al., 2010] and the observer's and user's guide at the ESA Herschel Website [ESA, 2012a] provide a detailed description.

## PACS: Photodetector Array Camera and Spectrometer

A PACS description can be found in the publication [Poglitsch et al., 2010], in the user's manual and observer's guide on the ESA Herschel Website [ESA, 2012a] and in the master thesis of Marko Mecina (2012), [Mecina, 2012].

## HIFI: Heterodyne Instrument for the Far Infrared

HIFI was not used in this master thesis. For further information a publication by [Graauw et al., 2010] and manuals on the ESA Herschel website [ESA, 2012a] are provided.

## Contributions

The Herschel mission runs under the authority of ESA. The technical and industrial part was executed by Thales Alenia Space Industries in Cannes (France), who leads a consortium of industrial partners like Astrium (Friedrichshafen, Germany), who are responsible for the PLM and the Thales Alenia Space Industry (Torino, Italy) has constructed the SVM. There are of course many other subcontractors spread over the World.

### PACS:

Design and construction led by Max Planck Institute for Extraterrestrial Physics (MPE), (Garching, Germany), contributions from Germany, Belgium, Austria, France, Italy, and Spain.

### SPIRE:

Design and construction led by the University of Wales (Cardiff, United Kingdom), contributions from United Kingdom, France, Canada, China, Italy, Spain, Sweden, and USA.

### HIFI:

Design and construction led by the Netherlands Institute for Space Research (SRON) (Groningen, The Netherlands), contributions from the Netherlands, France, Germany, and USA, Canada, Ireland, Italy, Poland, Russia, Spain, Sweden, Switzerland, and Taiwan.

### 2.1.1 MESS consortium

A detailed target list and further information can be found in the publication MESS (Mass-loss of Evolved StarS), a Herschel Key Program, [Groenewegen et al., 2011].

MESS is an abbreviation for Mass-loss of Evolved StarS, which acts as a consortium (started in 2003) to spend guaranteed observation time on the Herschel Space Telescope using two of the three instruments (PACS and SPIRE). Members, which are involved in the observation and science, come from Belgium, Austria and Germany, the SPIRE Specialist Astronomy Group 6 and further contributions from the Herschel Science Centre. This observation time is used for evolved objects like AGB-stars, post-AGB stars, red supergiants, luminous blue variables, Wolf-Rayet stars and final stage objects like planetary nebulae and supernova remnants.

The total amount of objects embraces 150 objects in imaging and approximately 50 objects in spectroscopy. Three hundred hours of observation time is assigned to the whole project, where imaging required 170 hours and the rest has been spectroscopy.

With new technology and space telescope missions like IRAS (Neugebauer et al., 2004), ISO (Kessler et al., 1996) as well as Spitzer (Werner et al., 2004) and AKARI (Murakami et al., 2007) a lot of data could be acquired to study many basic questions about the time evolution of the mass-loss rate, its geometry and the influence of the shaping of planetary nebulae as well as the interaction with the interstellar medium. A further important question concerns the chemical composition of the dust species, its physical and chemical processes and the influence on the mass-loss process.

#### Target selection: AGB-stars

A consequence of mass-loss are mostly spherical, shell-like structures around the AGB-stars called “circumstellar envelopes” (CSEs). These shell structures were detected by PACS and SPIRE and therefore analysed in the reduction processes. Out of the data we conclude the global evolution of the mass-loss phenomena. At a distance of one kpc a shell-like structure can be traced with a radius of  $3 \times 10^{14}$  km or 10 pc or 30 arcmin. In which the outer shell is thinner due to its slowing down and wind-ISM interaction.

The compilation of the objects was based on the ISO archive, where first all objects, which were marked as “stellar objects”, were chosen and additional sources with AGB stars. In special, stars with extended emission, which were already detected with IRAS, were added. The final sample should represent various spectral types (from M-subclasses, S-stars, carbon-stars), different variability types (L, SR, Mira) and extreme mass-loss rates (low to high). All objects with regions of high background were avoided and within the subclasses the brightest one was selected.

The sample for observing with PACS and SPIRE includes 30 oxygen-rich AGB- and RSG (Red SuperGiant)-stars, 9 S-Stars and 37 C-stars. A detailed list of objects divided into PACS and SPIRE is given in [Groenewegen et al., 2011].

## 2.2 The SPIRE instrument

### 2.2.1 Technical overview

In this chapter an overview of the technical part of SPIRE is given. Further information can be obtained from the observer's manual ([spire\\_om.pdf](http://spire.om.pdf)) on the ESA Herschel Website under <http://herschel.esac.esa.int> [ESA, 2012a] and the publication [Griffin et al., 2010].

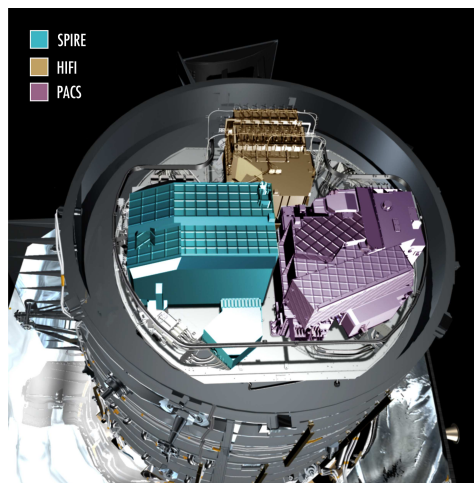


Figure 2.5: PACS, SPIRE and HIFI instruments on the top of the cryotank, [ESA, 2012a].

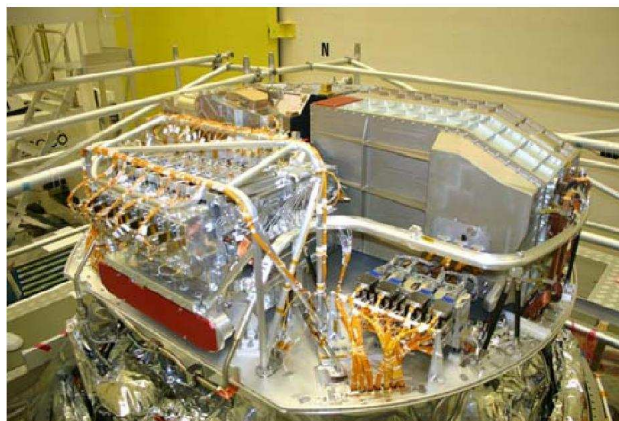


Figure 2.6: Left side: HIFI, right side: SPIRE, behind the two instruments: PACS, [Griffin et al., 2010].

SPIRE is an acronym for Spectral and Photometric Imaging REceiver and provides a three-band photometer (250  $\mu\text{m}$  (blue), 350  $\mu\text{m}$  (green), 500  $\mu\text{m}$  (red), field of view: 4 x 8 arcmin) and an imaging Fourier Transform Spectrometer (FTS, 194-671  $\mu\text{m}$ ). Only the photometer part was used and will be described in this master thesis.

The measurements of the SPIRE box are 70 x 40 x 40 cm in size and the box is mounted onto the cryostat to provide temperatures of 1.7 K to 4.5 K, which are connected with high thermal conductance straps. The box contains all of the instrument optics, the detector arrays (photometer: 3, spectrometer: 2) and an extra  $^3\text{He}$  cooler to reach temperatures of 0.3 K for the detectors, filters, internal calibrators and thermometers.

### The basic features and principles of a bolometer

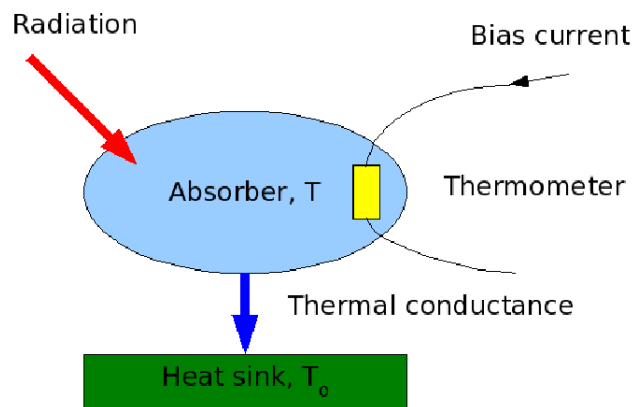


Figure 2.7: Typical function of a bolometer, [ESA, 2012a].

The radiation (Fig. 2.7) reaches the absorber with heat capacity  $C$  and dissipates to the heat sink, which is held at a fixed temperature  $T_0$  ( $\sim 0.3$  K) by a thermal conductance  $G$  (a higher  $G$  leads to a rapid heat dissipation).

To measure the temperature, a thermometer is built-in in the absorber. In addition a bias current  $I$  flows through the thermometer with the corresponding voltage  $V$ . The electrical power from the current  $I$  heats up the bolometer to a temperature  $T$  ( $T > T_0$ ). The temperature  $T$  is based on the absorbed radiant power  $Q$  (radiant and electrical power). When the radiation heats up the absorber a temperature change is caused and leads to a resistance change and so a different voltage is measurable.



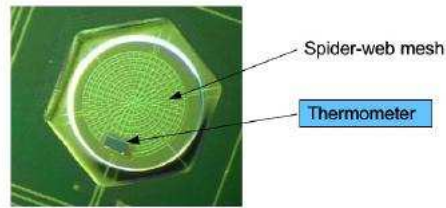


Figure 2.8: Absorber as spider-web mesh with thermometer, [ESA, 2012a].

The absorber (Fig. 2.8) is implemented as spider-web mesh composed of silicon nitride with a thin resistive metal coating. Furthermore the thermometers (size:  $10 \times 100 \times 300 \mu\text{m}$ ) are made of crystals of Neutron Transmutation Doped (NTD) germanium.

All five detector arrays are built of hexagonally close-packed feedhorn-coupled spider-web Neutron Transmutation Doped (NTD) bolometers.



Figure 2.9: SPIRE detector  $500 \mu\text{m}$ , 43 holes, [ESA, 2012a].

As an example, the  $500 \mu\text{m}$  (red) detector array (Fig. 2.9) is shown and its 43 holes lead to the feedhorns, where direct light can travel onto the actual detectors behind.

Each photometer bolometer array (Fig. 2.10) consists of different amounts of feedhorns. The blue feedhorns represent the overlapping bolometers in each array, which see the same sky position (rightmost Figure). The dead bolometers already on earth are shown as black circle. Furthermore the field of view of  $4 \times 8$  arcmin is indicated as red dashed rectangle.

## Scanmap

The construction of the map is performed by scanning with the telescope (motion of the telescope) at a nominal scan speed of 30 arcsec per second or in the fast mode at 60 arcsec per second.

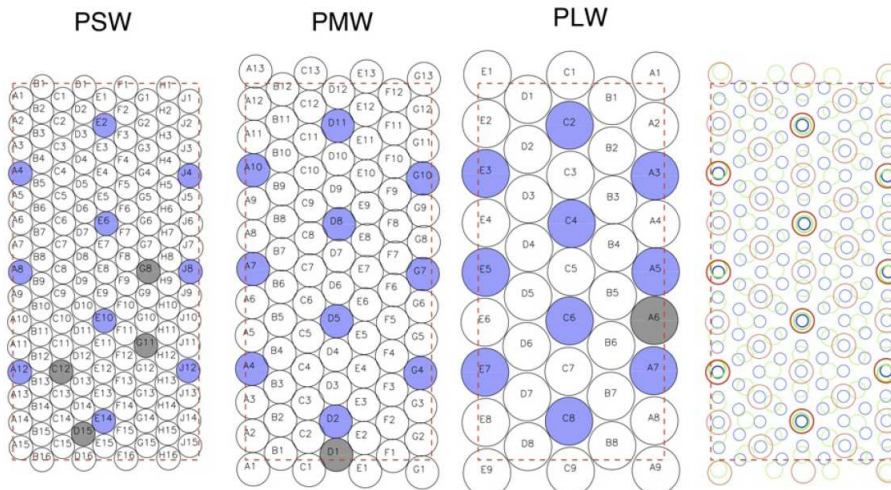


Figure 2.10: Detectors: blue: PSW ( $250 \mu\text{m}$ ) FWHM: 18.2 arcsec, green: PMW ( $350 \mu\text{m}$ ) FWHM: 24.9 arcsec, red: PLW ( $500 \mu\text{m}$ ) FWHM: 36.3 arcsec. The circle on the right side with the corresponding colour imagines the FWHM of the beam. The total amount of working bolometers of each array/channel is 104 of 139 (blue), 83 of 88 (green), 31 of 43 (red), [ESA, 2012a].

Logical operations like configuring the instrument, initialisation and science data taking of the observation are grouped into building blocks (BB). These operations are of course repeated several times to achieve a better S/N ratio and better map coverage. Except the configuring of the instrument (e.g. setting bias) is only done at beginning of the observation. During the observation the photometer calibration source, PCAL, is started at the end of an observation to track any brightness drifts, which adds  $\approx 20$  seconds to each photometer observation.

The SPIRE photometer can observe in all three photometer bands simultaneously with different modes:

- Large area maps (Fig. 2.11):  
The coverage of these maps exceeds areas larger than 5 arcmin in diameter, which is executed by scanning with the telescope (motion of the telescope).
- Small area maps:  
Areas smaller than 5 arcmin are scanned by two short cross-scans with the telescope.
- Point source photometry:  
Isolated point sources are observed by chopping, jiggling and nodding all the time to provide spatial information by using the Beam Steering Mirror (BSM) to modulate the beam.

For the two objects, U Ant and AQ And, the large area map mode was used in the observations, which will be described in the next passages.

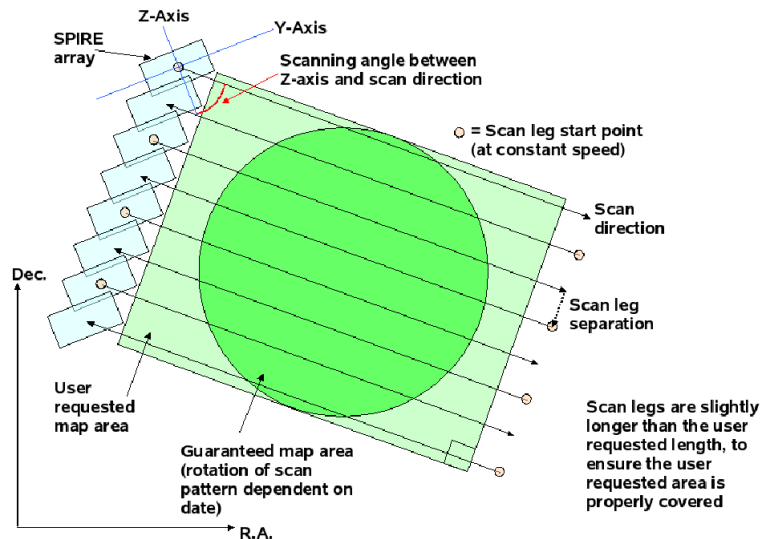


Figure 2.11: Typical SPIRE scanmap, [ESA, 2012a].

The scanning speed of the telescope is either nominal (30 arcsec/s) or fast (60 arcsec/s). For the two AGB-objects the nominal speed was applied.

The SPIRE arrays cover a 4 x 8 arcmin field, in which the telescope scanning is aligned at an angle of  $\pm 42.4$  degree with respect to the Z-axis of the arrays. Furthermore the scan lines are separated by 5.8 arcmin (348 arcsec) to overlap with the different scan-lines. This provides a good coverage for all three bands. Each scan line is stored in one building block.

To reach a better information content of the target object, cross-linked scanning (cross-scans, Fig. 2.11) is executed by scanning at  $+42.4$  degree (Scan A angle) and then at  $-42.4$  degree (Scan B angle). The limit for cross-scans is 4 square degree. But for single scans up to 20 degree areas in scan direction and 4 degree in the other direction can be covered.

The scan map of U Ant (Fig. 2.12) is  $\sim 1$  square degree in size and the observation integration was  $\sim 81$  minutes. Three cross-scans were performed, where one cross-scan consists of  $2 \times 6$  scanlines (total: 36 scanlines).

In Fig. 2.12 “Begin, 1. Scanline” indicates the beginning of the observation at the first scanline, which lasts to the beginning of the second scanline. Here the scanleg separation of  $\sim 6$  arcmin ( $0.1^\circ$ ) between two scanlines is recognizable. At the end of the sixth scanline one side-scan was finished and the telescope turned around and began with the next single-side scan (from 7. scanline to end of 12. scanline) until reaching the end of 1 cross-scan. This was performed three times until the end of 3 cross-scans was reached.

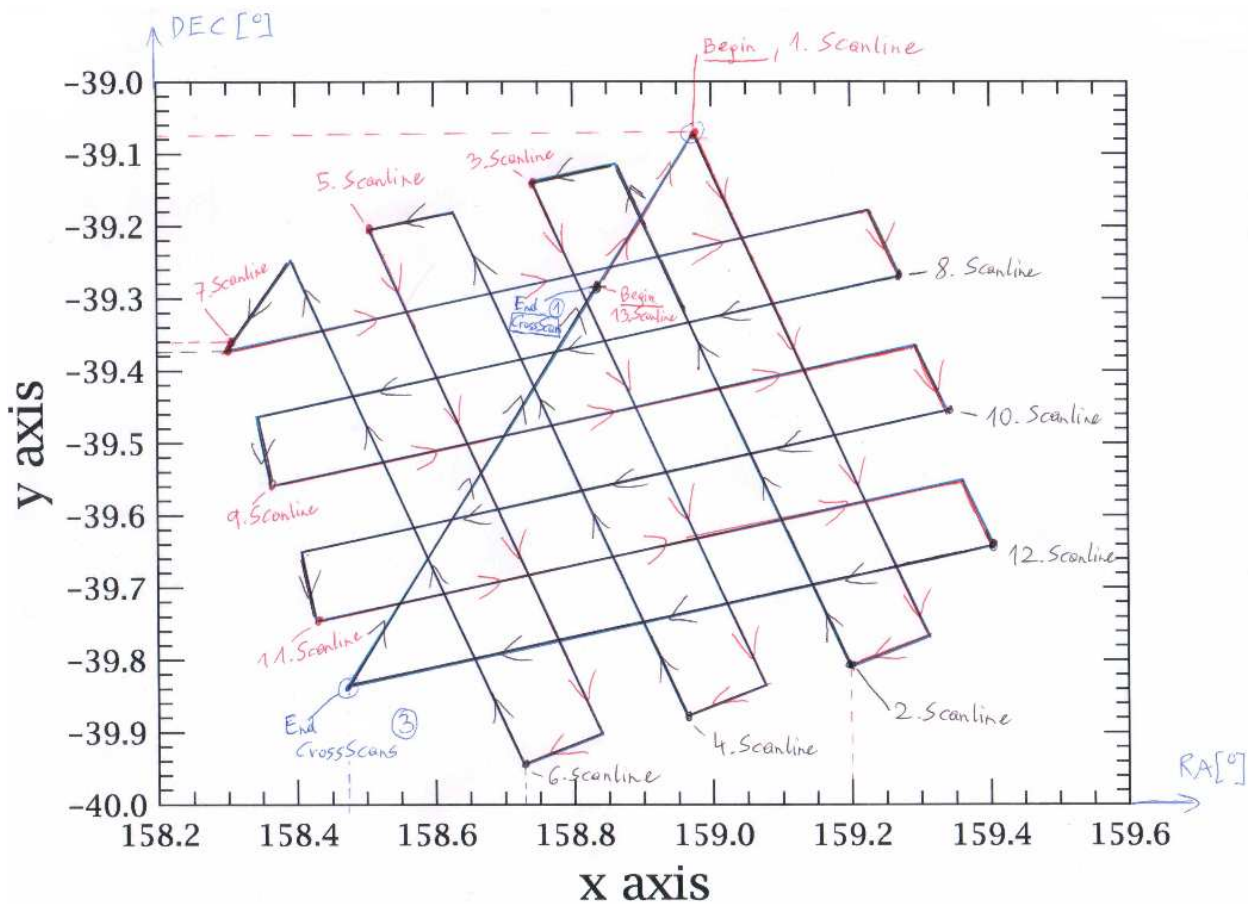


Figure 2.12: U Ant scan map (DEC [°] vs. RA [°]) of one blue bolometer (PSWF1), map size  $\sim 1 \times 1^\circ$ , 1 cross-scan =  $2 \times 6$  scanlines, total: 3 cross-scans,  $t \sim 81$ min.

For the object AQ And the scan map construction needed  $\sim 20$  min integration time because 1 cross-scan consists of  $2 \times 2$  scanlines. In total 4 cross-scans (16 scanlines) were required to cover the object.

## 2.2.2 Data reduction

### HIPE

The description consists of parts from the Herschel Data Processing Guide (Herschel\_DP\_howtos\_v1.2.pdf), from the ESA Herschel Website [ESA, 2012a]. Further information on HIPE can be retrieved from publications from [Ott, 2010] and [Science Ground Segment Consortium et al., 2011].

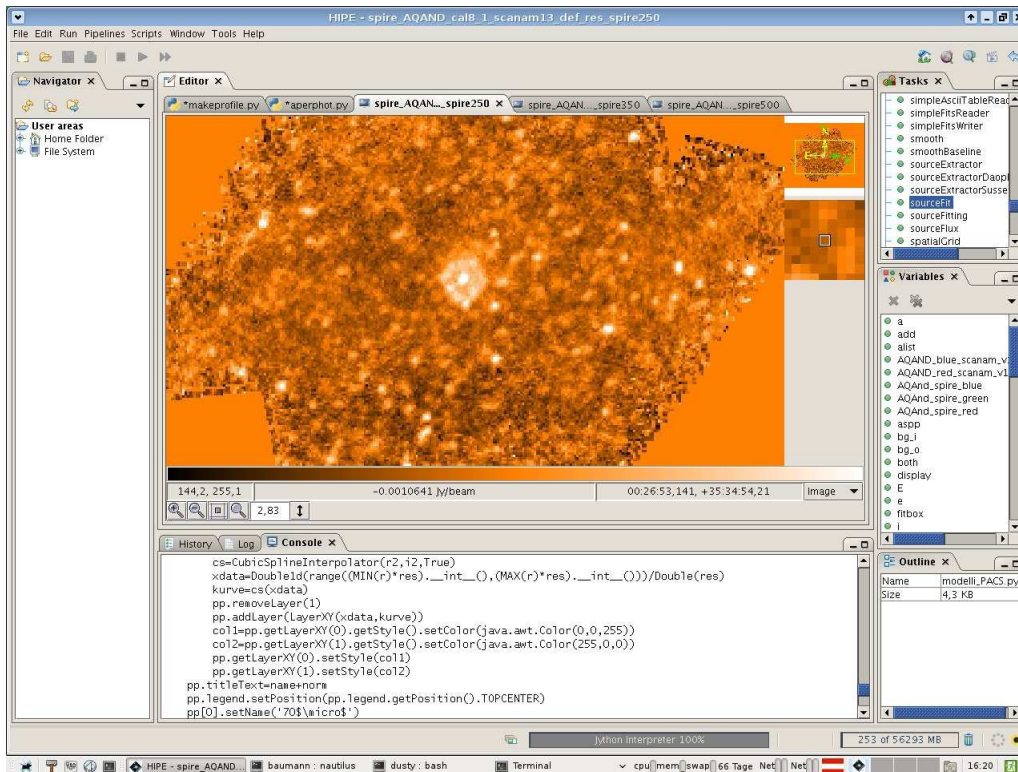


Figure 2.13: HIPE - Herschel Interactive Processing Environment, [ESA, 2012a].

Herschel Interactive Processing Environment (HIPE, Fig. 2.13) is a graphical user interface, which helps the user to take a look at the data easily and to process low-level data to scientific images. Furthermore HIPE provides many tools to analyse the images, for example the aperture photometry, which can be applied interactively through a GUI or the command line. Jython (version 2.1), which is the Java implementation of the Python language, is used as input language in the built-in editor and also on the command console.

The user can easily import Java and Python packages to extend the user's needs at the programming tasks and can use python syntax to simplify the data processing work. A browser for the different data types (variables), a history browser and a task browser support the processing of data and give an overview of the running tasks.

After the observation of an object has been done, it becomes available on the Herschel Science Archive (HSA). Through a unique observation id, each object can be selected when the access is authorized.

The data of the observation are stored in pools, which can be either retrieved through the HSA or as http streaming or as whole tar file. In our case all relevant object data (MESS; Groenewegen) were stored on a local server to get fast access to the data.

In the local pool the different observations are stored as products, which contain raw and processed detector data (different levels of processed data), timelines, calibration data, auxiliary (e.g. pointing) data, image cubes, data contexts, history data and a lot more.

### 2.2.2.1 Data structure

A detailed description of the data structure can be found in the SPIRE Data Reduction Guide (`spire_dum.pdf`) on the ESA Herschel Website, [ESA, 2012a].

### Astronomical Observation Templates (AOTs)

The SPIRE observational data consist of Building Blocks (BB) (Timeline Data Products, Fig. 2.14), which reflect the operations (logical operations; configuring the instrument, initialisation and science data taking) during the observations (e.g. a scan line in a map or a segment of housekeeping scans and others). Astronomical Observation Templates (AOTs) are a combination of these Building Blocks.

Each dataset contains several contexts (e.g. for level 1 data), which act like a catalogue index to group the coherent data. These contexts can be built up of BB and other products and for example each product in the SPIRE pipeline has its own context.

To access the whole observation of an object, the Observation Context (Master Context, ObsC, Fig. 2.14) is used.

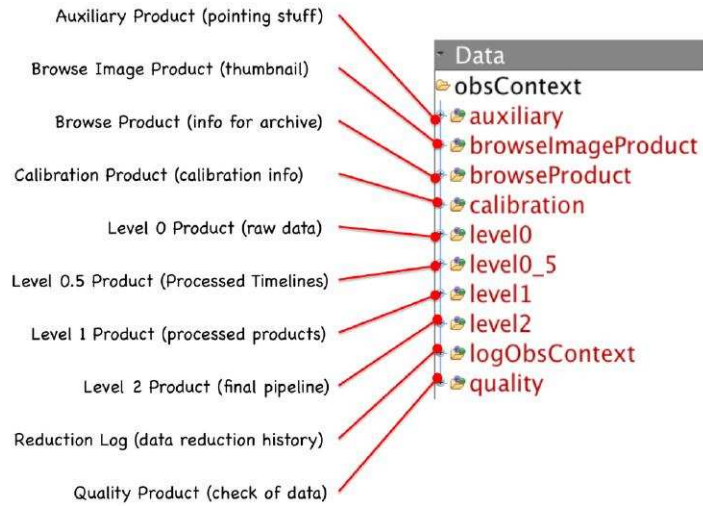
The command syntax and the call of the observation context will be explained in the next chapter “Reduction Process”.

Furthermore a summary entry, meta-data blocks and data blocks are stored in the ObsC.

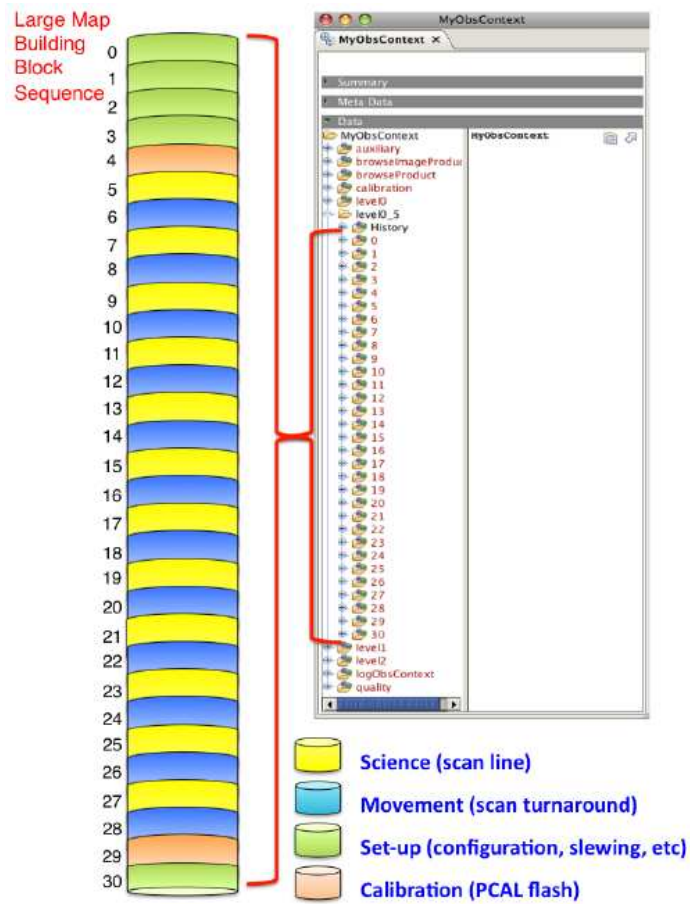
The summary entry lists all relevant information for the observation like instrument type, target position, ObservationID, operational day and observation mode and much more.

In addition the meta-data block stores the information on the product, which are necessary to describe and process the pipeline.

In the data part all levels of data, including the calibration, pointing and auxiliary products are grouped and accessible through their context pointers.



(a) ObsContext for SPIRE data.



(b) Building blocks of Level 0.5 data.

Figure 2.14: ObsContext for SPIRE data (Fig. 2.14(a)) and BBs Level 0.5 data (Fig. 2.14(b)), where each BB represents one scanline, [ESA, 2012a].

### 2.2.2.2 Reduction process

In this thesis only the SPIRE Photometer part (no Spectrometer) of reduction is described. See the master thesis of Marko Mecina (2012) for a description of the PACS pipeline and additional information can be obtained from [Poglitsch et al., 2010] and [ESA, 2012a].

The SPIRE pipeline, which represents the reduction process of the SPIRE Raw Data to the final SPIRE maps, was developed and implemented in Java by the Herschel Science Center (HSC) and Herschel Instrument Control Centres (ICCs). It supports the user to convert raw data to high-level science images, where the instrumental effects should be removed as much as possible. In addition the Jython scripts to reduce the data are distributed with HIPE and can run step by step or all at once.

#### Short description of the reduction process, Fig. 2.15

The pipeline user already gets the processed data as different Levels (0, 0.5, 1, 2) through an automated process.

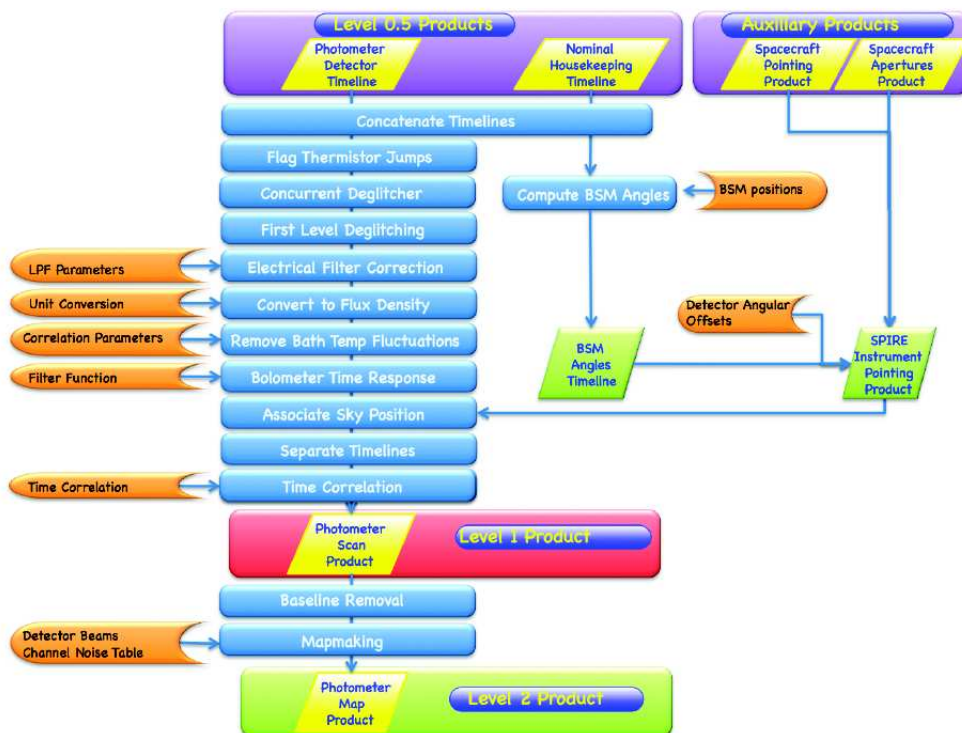


Figure 2.15: Data level overview, [ESA, 2012a].



**Spire Data Overview (accessible through the Observation Context):**

- Level 0:  
Level 0 data originate from the raw telemetry direct from the telescope without any pipeline processing.
- Level 0.5:  
To get the Level 0.5 data, the pipeline converts the timelines in engineering units (temperature, voltages, ...).
- Level 1:  
The Level 1 data is produced through AOT specific pipeline processing like correction of thermistor jumps, optical and electronic crosstalk and sky position association and many more.
- Level 2:  
The final maps for each detector are ready for the analysis and photometry and can be stored as fits files.
- calibration:  
The calibration context pointing to all calibration products required for the processing of SPIRE data.
- auxiliary:  
Spacecraft pointing, auxiliary files required for processing.
- logObsContext:  
Processing history of the data.
- quality:  
Quality control products for this observation.
- browseImageProduct:  
Thumbnail products from the automated processed maps.

In the next paragraph the jython script code for the SPIRE data reduction is described, which is available directly in HIPE under the menu Pipelines => SPIRE => SPG Scripts => Photometer Large Map Pipeline script (POF5). The script was adapted for the reduction and the objects.

**Standard Pipeline Processing Script in Jython; distributed with HIPE v8:**

```
# ... Comments
\  
 \ ... line break

# Import classes and definitions:
from herschel.spire.all import *
from herschel.spire.util import *
from herschel.ia.all import *
from herschel.ia.task.mode import *
from herschel.ia.pg import ProductSink
from java.lang import *
from java.util import *
from herschel.ia.obs.util import ObsParameter
from herschel.ia.pal.pool.lstore.util import TemporalPool
from herschel.spire.ia.pipeline.scripts.POF5.POF5_tasks import *
from herschel.spire.ia.pipeline.scripts.POF5.POF5_input import *
```

Many Java classes and functions are imported, which are required during the processing task.

```
# UANT
myObsid=1342188161
```

This is the unique observation id from the object U Ant.

```
# read-in obs data from local pool
poolLocation="/supp/mess/lstore/"
obs = getObservation(myObsid, poolLocation="/supp/mess/lstore/")
```

The variable obs stores the Observation Context, which is the pointer to the observation.

```
# show cal version
print "Default caltree from Obs: " + str(obs.calibration.version)

cal = spireCal(jarFile="/home/mess/Downloads/spire_cal_8_1.jar")

obs.calibration.update(cal)

print "Default caltree from HIPE: " + str(obs.calibration.version) \  
 + " => is set"
```

The version of the Calibration Tree (CalT) of the observation is printed and then updated to the latest version, which can be found on the website <http://wakefield.bnsc.rl.ac.uk/icc/CalibrationTrees.html>.

The CalT should be replaced by the latest available calibration to get the best correction results for the flux density and other improvements.

That's why for new observed objects there is no CalT in the SPIRE data shipped, and so it is required to provide a CalT.

```
# --- for AQ AND
obs.calibration = cal
```

For example, for the object AQ And it is mandatory to add a CalT, because no “obs.calibration.update(cal)” is possible due to the missing CalT.

```
# Extract the calibration products from the observation context:
bsmPos=obs.calibration.phot.bsmPos
lpfPar=obs.calibration.phot.lpfPar
detAngOff=obs.calibration.phot.detAngOff
elecCross=obs.calibration.phot.elecCross
optCross=obs.calibration.phot.optCross
chanTimeConst=obs.calibration.phot.chanTimeConst
chanNum=obs.calibration.phot.chanNum
fluxConvList=obs.calibration.phot.fluxConvList
tempDriftCorrList=obs.calibration.phot.tempDriftCorrList

# Extract the auxiliary products from the observation context:
hpp=obs.auxiliary.pointing
siam=obs.auxiliary.siam
timeCorr = obs.auxiliary.timeCorrelation
```

Different calibration data are stored in variables, which will be used by the following functions below.

```
# start from level0: (raw data)
level0_5=engConversion(obs.level0,cal=obs.calibration, \
tempStorage=Boolean.FALSE)

# start from level0.5 instead: # for AQAND

level0_5=obs.level0_5
```

All the raw data from the spacecraft and the SPIRE instrument relevant for the observation are converted to engineering units. For example, the bad bolometers of each channel are masked or the voltages of the bolometers are calculated and others.

For object AQ And it is necessary to start from Level 0.5, because there is only Level 0.5 data available.

```

bbids = level0_5.getBbids(0xa103)
nsubscans = len(bbids)
if nrep == 0:
    nscans = 1
    nlegsperscan = nsubscans
else:
    nscans = 2*nrep
    nlegsperscan = nsubscans/nscans
print "number of scans: ", nscans
print "number of subscans: ", nsubscans
print "number of legs per scan = ", nlegsperscan

```

The building blocks from the Level 0.5 data are stored and the number of scans (the whole observation process) and the amount of subscans (scanlines) are printed.

```

# Create Level1 context:
level1_allscans = Level1Context(myObsid)

```

A new Level 1 Context is created to have access to the Level 1 data after processing.

With the next step the data will be attached together per scanline and BB.

```

# Loop over scan legs:
counter = 0
for bbid in bbids:
#
    block=level0_5.get(bbid)
    print "processing BBID="+hex(bbid)
    # engineering data products:
    pdt = block.pdt
    nhkt = block.nhkt
    if pdt == None:
        logger.severe("Building block "+hex(bbid)+" doesn't contain \
a PDT. Cannot process this building block.")
        print "Building block "+hex(bbid)+" doesn't contain a PDT. \
Cannot process this building block."
        continue
    if nhkt == None:
        logger.severe("Building block "+hex(bbid)+" doesn't contain \
a NHKT. Cannot process this building block.")
        print "Building block "+hex(bbid)+" doesn't contain a NHKT. \
Cannot process this building block."
        continue

```

```

    # attach turnaround data:
    bbCount=bbid & 0xFFFF
    pdtLead=None
    nhktLead=None
    pdtTrail=None
    nhktTrail=None
    if bbCount > 1:
        blockLead=level0_5.get(0xaf000000L+bbCount-1)
        pdtLead=blockLead.pdt
        nhktLead=blockLead.nhkt
        if pdtLead != None and pdtLead.sampleTime[-1] \
            < pdt.sampleTime[0]-3.0:
            pdtLead=None
            nhktLead=None
    if bbid < MAX(Long1d(bbids)):
        blockTrail=level0_5.get(0xaf000000L+bbCount)
        pdtTrail=blockTrail.pdt
        nhktTrail=blockTrail.nhkt
        if pdtTrail != None and pdtTrail.sampleTime[0] \
            > pdt.sampleTime[-1]+3.0:
            pdtTrail=None
            nhktTrail=None
    pdt=joinPhotDetTimelines(pdt,pdtLead,pdtTrail)
    nhkt=joinNhkTimelines(nhkt,nhktLead,nhktTrail)

```

Nominal House Keeping Timeline (NHKT) stores the Beam Steering Mirror (BSM) sensors values.

```

    # BSM angles:
    bat=calcBsmAngles(nhkt, bsmPos=bsmPos)

```

The BSM Angles Module (`calcBsmAngles`) links the angles of the Beam Steering Mirror (BSM) to decimal degrees on the sky. The data from the calibration table are interpolated, where spacecraft angles Y and Z axes and the BSM chop and jiggle axes are given.

```

    # pointing product:
    spp=createSpirePointing(detAngOff=detAngOff, bat=bat, \
        hpp=hpp, siam=siam)

```

The BSM position, the global spacecraft pointing, the relative position of each bolometer, and the information of the SIAM matrix (Spacecraft-Instrument Alignment Matrix) are collected and stored in one product.

```

    # electrical crosstalk correction:
    pdt=elecCrossCorrection(pdt, elecCross=elecCross)

```

The electrical cross talk is removed from the detector timelines. In the building phase of Herschel there was no electrical crosstalk or only measured at low-levels.

```
# optical crosstalk correction:
pdt=photOptCrossCorrection(pdt,optCross=optCross)
```

```
# deglitching:
pdt=waveletDeglitcher(pdt, scaleMin=1.0, scaleMax=8.0, \
scaleInterval=5, holderMin=-1.9, holderMax=-0.3, \
correlationThreshold=0.69)
```

The concurrent deglitcher module detects and removes glitches (cosmic rays in the electronics) from all photometer arrays (PSW, PMW and PLW) by a running median of the input signal.

```
# electrical filter response correction:
pdt=lpfResponseCorrection(pdt,lpfPar=lpfPar)
```

This module is responsible for removing the response of the electrical filter (low-pass filter) from individual photometer detector time-lines (PDT).

```
# flux conversion:
fluxConv=fluxConvList.getProduct(pdt.meta["biasMode"].\
value,pdt.startDate)
pdt=photFluxConversion(pdt,fluxConv=fluxConv)
```

A correction is applied against the nonlinear bolometer responsivity (photometer detector voltage timeline (PDT)) The module returns the in-beam flux density timeline.

```
# temperature drift correction:
tempDriftCorr=tempDriftCorrList.getProduct(pdt.meta["biasMode"].\
value,pdt.startDate)
pdt=temperatureDriftCorrection(pdt,tempDriftCorr=tempDriftCorr)
```

Low frequency ( $< 1$  Hz) noise is subtracted with help of empirical correlations between detectors and thermistors, which was caused by variations of the detector array bath temperature.

```
# bolometer time response correction:
pdt=bolometerResponseCorrection(pdt,chanTimeConst=chanTimeConst)
```

There is a transient response of each bolometer, which should be removed.

```
# add pointing:
psp=associateSkyPosition(pdt,spp=spp)
```

This module associates the RA and Dec positions of each bolometer at a given time

(SpirePointingProduct).

```
# remove duplicate turnaround data:  
psp=cutPhotDetTimelines(psp,extend=True)
```

The turnaround is linked together with the scan line detector timelines and doubled scanline turnaround data are removed.

```
# apply the time correlation  
psp=timeCorrelation(psp,timeCorr)  
  
# store product in level 1 product storage:  
level1_allscans.addProduct(psp)  
  
print "Completed BBID="+hex(bbid)  
counter = counter +1  
nsubsinit = nsubscans - counter  
if nsubsinit > 0:  
    print str(nsubsinit) + " subscan(s) to process"
```

The next step depends on the map making algorithms, which are described in the next chapters MADMap and Scanamorphos(ScanAm).

### 2.2.2.3 MADMap

The MADMap map maker was only used for testing purposes and as comparison. The final maps are produced with the ScanAm algorithm.

For more details to the MADMap algorithm a publication “MADMap: A Massively Parallel Maximum-Likelihood Cosmic Microwave Background Map-Maker” by C. M. Cantalupo, [Cantalupo et al., 2010], is provided.

With the MADMap algorithm maximum-likelihood images of the sky from timeline data including noise, which are retrieved and collected from Cosmic Microwave Background (CMB) experiments (e.g. Planck, EBEX), can be created. It is based on a preconditioned conjugate gradient solver, fast Fourier transform and sparse matrix operations, so the MADMap supports the reduction of massive data sets.

MADMap assumes a piecewise stationary Gaussian noise with the noise spectral density as input.

```
# Create a list of scan lines to be used as input for the map making
scans=SpireListContext()

# Run baseline removal and populate the map making input
for i in range(level1.count):
    psp=level1.getProduct(i)
    psp=removeBaseline(psp,chanNum=chanNum)
    scans.addProduct(psp)
```

The brightness drift (baseline removal) was removed.

```
print 'Starting Mad Mapper'
chanNoise=obs.calibration.phot.chanNoiseList.getProduct \
(level1.getProduct(0).meta["biasMode"].value,level1. \
getProduct(0).startDate)
# requires Channel Noise Table Calibration Product
# red
mapPlw=madScanMapper(scans, array="PLW",\
chanNoise=chanNoise,resolution=14)

# green
mapPmw=madScanMapper(scans, array="PMW",chanNoise=\
chanNoise, resolution=10)

# blue
mapPsws=madScanMapper(scans, array="PSW",\
chanNoise=chanNoise, resolution=6)
```

Creates the final maps for each detector with appropriate standard resolutions 6, 10 and 14 arcsec.



#### 2.2.2.4 Scanamorphos

Scanamorphos (ScanAm) is an external reduction method, which is not part of HIPE and is implemented in IDL (Interactive Data Language), which supports the user to analyse and visualize the data.

Website: <http://www2.iap.fr/users/roussel/herschel/>

Publication: Scanamorphos : a map-making software for Herschel and similar bolometer arrays used in scan mode, H. Roussel, 2010, [Roussel, 2010]

The term ScanAmorphos is a combination of “scan” and “anamorphosis”, which is the mathematical and optical transformation of an image. Furthermore the algorithm to post-process Herschel data from the instruments PACS and SPIRE, can also be used for similar bolometer arrays (e.g. P-Artemis on the APEX telescope).

As basis in the post-processing the total low-frequency noise (thermal and non-thermal) is removed as good as possible and cosmic rays (glitches) are masked. The data are observed multiple times with different bolometers in PACS and SPIRE and so the redundancy is high enough to reconstruct the effective data, and so to remove the noise without assumption of a noise model or Fourier-space filtering.

The script needs no interaction during the reduction, only the input files and additional parameters like resolution and others are needed. Because of its mapping efficiency nature, the script is attended in fields larger than a few arcminutes and for extended Galactic regions, galaxies in the neighbourhood and high-redshift surveys.

ScanAm removes the additive brightness drifts caused by the low-frequency noise as well as the flicker noise. The glitches, which are left from the HIPE pipeline processing, will be masked. Out of the projection of the data onto a spatial grid, the creation of additional maps for the error and weight is supported. In addition the ScanAm algorithm can handle compact sources and extended sources on different spatial scales, which is a big advantage compared to the MADMAP algorithm. Another advantage is the unified and adaptable analysis and processing algorithm, which requires only minimal knowledge of the instrument properties.

Due to the cross-scanning in PACS and SPIRE during the observation the drift per each bolometer can be analysed and characterized to remove its effects and to achieve the desired sensitivity.

The low-frequency noise (LFN) (PACS:  $\sim 1$  Hz, SPIRE:  $\sim 0.1$  Hz) is recognisable in the maps as stripes parallel to the scan direction. The removal is non-trivial because the noise also alters the photometric and structural source properties, which limits the sensitivity to faint objects.

As a consequence of temperature fluctuations of the cryogenic tank, the fluctuations

introduce noise in each bolometer, which is correlated with the other bolometers (first component (thermal) of low-frequency noise). Due to the existence of blind bolometers, which are unaffected by the sky signal, these probes can be used as calibration data. The second part of the low-frequency noise is non-thermal origin, uncorrelated from bolometer to bolometer and summed in a term named “flicker noise”. Unfortunately the second component cannot be calibrated and so must be estimated by the detector physics and readout electronics. These two sources of noise are mainly the origin of the brightness drifts and purely additive.

The step before the low-noise removal is the zero-order removal. Each bolometer has an in-beam flux density with a reference to a fixed voltage, which represents a perfect dark sky during an observation. But these fixed voltages cannot be calibrated because the signal of each bolometer is a combination of the true sky signal, the noise and a large offset, which will be removed during the zero-order baseline removal, whereas the offset varies strongly between the different detectors. So a constant value is derived per bolometer and per scan leg, and is used for further linear baseline removal.

### Overview of the algorithm

- 1.) derive map coordinates from the sky coordinates
- 2.) compute the scan speed and tagging the nominal data and non-zero acceleration data (on the turnarounds)
- 3.) create the space and time grids
- 4.) divide signal by the relative gains
- 5.) measure high-frequency noise and start first-pass glitch masking
- 6.) subtract the linear baseline effectively with timescales equal or larger of the scanleg duration (brightness drift removal)
- 7.) subtract the average drift on short timescales and glitch making
- 8.) subtract individual drifts and glitch masking
- 9.) project the signal, error, total drifts and weight maps on a fine pixel grid
- 10.) optional: mosaicking of spatial blocks separately

First the Level 1 data per each scanline must be exported as fits files through HIPE with the following script:

(without baseline removal, which is performed in ScanAm!)

```

path = "/output/path"

# Save level 1 data as fits files:

if nlegsperscan > 99:
    prefix_1="00"
    prefix_2="0"
else:
    prefix_1="0"
    prefix_2=""

for iscan in range(nscans):
    scan = first_scan_num + iscan
    if scan < 10 and nscans > 9:
        str_scan = "0"+str(scan)
    else:
        str_scan = str(scan)

    root_filename = path + "level1_scan_"
    for ileg in range(nlegsperscan):
        bbid = ileg+iscan*nlegsperscan
        product = level1_allscans.getProduct(bbid)
        subs = bbid+1
        if subs < 10:
            str_subs = prefix_1+str(subs)
        else:
            if subs < 100:
                str_subs = prefix_2+str(subs)
            else:
                str_subs = str(subs)
        filename = root_filename+"_leg"+str_subs+"nrep"+"fits"
        fits.save(filename,product)
    print filename

```

Now all scanlines are stored as fits files in the output directory. (E.g. U Ant: 36 scanlines, AQ And: 16)

The next step is the creation of the file named "scanlist\_spire" in the output directory: Contents: U Ant sample – "scanlist\_spire"

First line: output path of the fits/xdr

Next Lines: fits-file names with extension written as xdr for each scanline (no rename!)

```

/output/path/
stru_level1_scan__leg01nrep.xdr
stru_level1_scan__leg02nrep.xdr
....
stru_level1_scan__leg36nrep.xdr

```

After this creation, idl can be started with command “idl”, and a prompt opens:

Now the two for-loops can be executed:

```

for i=1, 9 do convert_hcssfits_spire, dir_in='/output/path',\
  root='level1_scan__leg0'+ strcompress(string(i), /remove_all) + 'nrep'

for i=10,36 do convert_hcssfits_spire, dir_in='/output/path/',\
  root='level1_scan__leg'+ strcompress(string(i), /remove_all) + 'nrep'

```

Now all 36 fits files are converted to xdr files, which are compatible with the ScanAm script.

With the next idl command the final maps for SPIRE will be created.

```

scanamorphos, /spire, nobs=1, dir_scanmap="/output/path/", /one_plane_fits

```

This ScanAm script reduces the Level 1 data to the final maps.

Each detector map can be created separately or all maps at once and with different resolutions.

The results are four maps:  
drifts, error, weight, signal map.

The signal map is the final map.

## 3 Science objects

In this chapter the properties and features of both science objects, U Ant and AQ And, are outlined. For each object there is also a publication overview, which highlights the important publications due to (detached) shells and similar structures.

### 3.1 U Ant

#### 3.1.1 Properties and features

The object is classified as carbon star with spectral type C5,3 ([Eggen, 1972], [Sloan et al., 1998] General Catalog of Variable Stars (GCVS)) and an effective temperature of 2810 K with a C/O-ratio of 1.44 [Bergeat and Chevallier, 2005]. Furthermore the AGB-star belongs to the slow irregular variable group (Lb, [Sloan et al., 1998]), which are mostly giants with poorly defined periods and only erratic variations ([Eggen, 1972], 365 days suggested, but uncertain).

As progenitor star a three to five sun mass ZAMS-star is assumed by [Izumiura et al., 1997]. Revised Hipparchos measurements show a distance of 320 pc [Bergeat and Chevallier, 2005]. In the publication by [Kerschbaum et al., 2010] the luminosity  $L = 8000 L_{\odot}$  was determined by fitting the synthetic SED to the observed SED and photometry from the literature [Sloan et al., 2003]. The absolute bolometric magnitude is calculated to -4.93 [Bergeat and Chevallier, 2005].

The star U Ant is located in the constellation Antlia with a right-ascension (RA) of 10 h 35 m 12.85153 s and a declination (DEC) of  $-39^{\circ} 33' 45.3180''$  (ICRS, J2000, [van Leeuwen, 2007]) with proper motions [van Leeuwen, 2007] in RA of -31.02 mas/yr and in DEC of 3.50 mas/yr. In addition the radial velocity is estimated to 37 km/s (General catalog of radial velocities (GCRV), [Wilson, 1953]) and revised by [Walker, 1979] to 48.4 km/s.

U Ant is a well studied object going back to the 1980s, where intensive CO-observations [Olofsson et al., 1988] revealed a circumstellar envelope. With new space telescope missions like IRAS (Infrared Astronomical Satellite, started in 1983), there were new opportunities to detect extended missions around AGB-stars. [Izumiura et al., 1997] revealed two dust shells (Fig. 3.2) at 46 arcsec and 180 arcsec (3 arcmin), which were partly detected by Herschel-PACS (70  $\mu\text{m}$ , [Kerschbaum et al., 2010]). These dust shells are assumed to be short high mass-loss events.

[González Delgado et al., 2001] performed imaging with scattered light and at least one shell at 43 arcsec with possible inner and outer shells at 25 arcsec, 37 arcsec and 46 arcsec were found. With additional polarisation filters it was assumed that the 46" shell is mainly dust, where the 43" shell is gas-dominated.

A re-observation by [Maercker et al., 2010] in scattered light and CO-lines verified the shell at 43 arcsec, which was also detected by [Kerschbaum et al., 2010] in the Herschel-PACS and SPIRE instruments, and an outer shell at 50 arcsec. Additional arc-like structures at 25 and 37 arcsec, which are not centred to the star, are tentative. These structures could be superimposed with detached shell at 42 arcsec, because the radial profile of SPIRE observations indicates a flattened peak at  $\sim 36$  arcsec. There was also no indication of a 46 or 50 arcsec shell with PACS, but a suggestion is that gas and dust shells are co-spatial. The shell at 42 arcsec (Fig. 3.5 and Fig. 3.7) suggests a brief mass-loss some 2800 years ago with additional wind-wind and wind-ISM interactions. Additional output parameters by modeling by [Kerschbaum et al., 2010] estimate the dust temperature of the 42 arcsec shell to 39.3 K with a mass-loss of  $7 \cdot 10^{-7} M_{\odot}$  per year by assuming an optically thin detached shell.

Recent studies of AKARI-observations by [Arimatsu et al., 2011] verified the two dust shells at 43" and 50" in the mid-IR (15 and 24  $\mu\text{m}$ ), which were already found by [Maercker et al., 2010] in scattered light. The dust shell at 42" or 43" was also visible in PACS- and SPIRE-observations. Furthermore the assumption that the shell at 42"/43" is gas-rich, is supported by fitting and modeling the SED-profile of PACS and AKARI observations ([Arimatsu et al., 2011]). [Arimatsu et al., 2011] presumed that the separation in gas and dust is the effect of drift motion of submicron-sized dust grains relative to the gas. The hotter (104K) 50" shell is associated with the gas-rich 42" shell (60 K), which consists of very small grains that are strongly coupled with the gas.

### 3.1.2 Publication overview

The available publications about shell detection and other extended structures for the science object “U Ant” are discussed in this chapter.

#### SEST CO (J=1-0) observations of carbon-rich circumstellar envelopes

[Olofsson et al., 1988]

The first evidences of shell-like structures have been observed with SEST (Swedish ESO Submillimetre Telescope at La Silla) in the CO-line ( $J = 1-0$ ) profile at the sub-millimetre range.

With the help of the spectral lines of CO (Fig. 3.1), the author measured a double-peaked line shape (main beam brightness temperature  $T_{\text{mb}}$  [K] vs.  $v_{\text{LSR}}$  [km/s]), which indicates on optically thin, spatially resolved circumstellar envelope (CSE) or “optically thin shell”. In this publication there is no mass-loss determination because of lack of

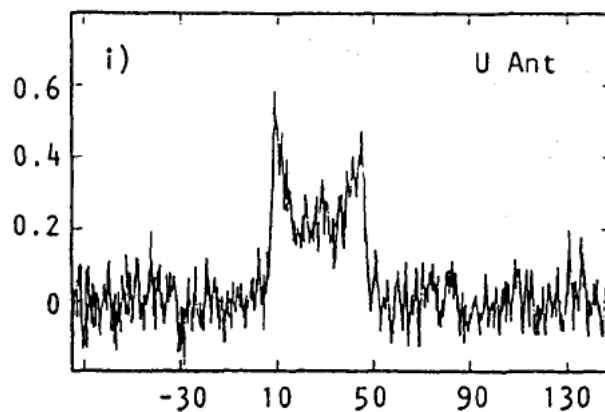


Figure 3.1: Double-peaked line shape;  $T_{\text{mb}}$  [K] vs.  $v_{\text{LSR}}$  [km/s], velocity resolution: 0.22km/s, [Olofsson et al., 1988].

data, and too uncertain measurements. But an existence of a detached shell is mentioned as a cold dust shell with very little hot dust close to the star. Furthermore the dependence of He shell flashes (thermal pulses) with ceasing of mass-loss was assumed.

#### A double dust shell surrounding the carbon star U Antliae

[Izumiura et al., 1997]

With the help of IRAS (Infrared Astronomical Satellite) an investigation of the carbon star U Ant was started. IRAS wavelength range covers 12, 25, 60, and 100  $\mu\text{m}$ , where 250 thousand infrared sources were observed. For the science object only the 60 and 100 micrometer band was used. Izumiura et al. discovered two dust shells at 46 arcsec and 3 arcmin, which are probably two detached shells, correlated with two consecutive thermal pulses during the AGB evolution.

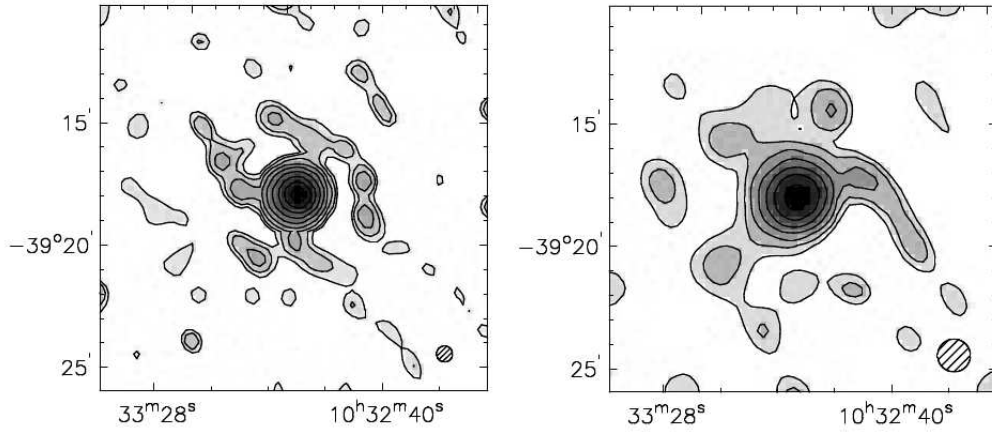


Figure 3.2: High resolution IRAS images (HIRAS) at 60  $\mu\text{m}$  (left) and 100  $\mu\text{m}$  (right), [Izumiura et al., 1997].

The high-resolution IRAS (HIRAS) image (Fig. 3.2) has a resolution of  $39 \text{ arcsec} \pm 2 \text{ arcsec}$  at 60 micron and  $80 \text{ arcsec} \pm 10 \text{ arcsec}$  at 100 micron. In Fig. 3.2, the contour levels start at  $1 \text{ MJy sr}^{-1}$  with steps of the power of 2. The circle in the bottom-right corner indicates the appropriate FWHM of a point source.

The double dust shell is recognisable at 60 micron as extended central component with a FWHM of 55 arcsec and a well-defined ring-like structure is shown (inner shell at  $\sim 46 \text{ arcsec}$ ). The second component is at about 3 arcmin radius around the central region. At 100 micron the central shell has a FWHM of about 90 arcsec, but fainter emission than at 60 micron. A more asymmetric distribution of the shell region exists due to the not flattened background.



### Imaging of detached shells around the carbon stars R Scl and U Ant through scattered stellar light

[González Delgado et al., 2001]

U Ant was observed (Fig. 3.3) in scattered light in narrow band filters (resonance lines of K and Na) and in Strömgren *b* filter. The K filter revealed a geometrically thin ( $\sim 3$  arcsec) shell with spherical geometry at 43 arcsec radius, which is at least partially optically thin. These results are in agreement with the observation in CO. Furthermore in the Na filter the shell at 43 arcsec seems to be more optically thick and in addition at least one, possibly two shell structures are detected inside the shell as weak scattering. This multiple-shell structure was not detected in CO observations, but the explanation might be the low mass of these weak shells. Another weak presence of an outer shell after 43 arcsec can be assumed.

| Filter        | component   | $R$ (") | $\Delta R$ (") |
|---------------|-------------|---------|----------------|
| Gunn <i>z</i> | total shell |         |                |
|               | star        |         |                |
| KI            | shell1      | 25:     | 3:             |
|               | shell2      | 36.5    | 6:             |
|               | shell3      | 43.2    | 3.2            |
|               | shell4      | 46.1    | 10.0           |
|               | total shell |         |                |
|               | star        |         |                |
| NaD           | shell1      | 25:     | 8:             |
|               | shell2      | 36.5    | 6.4            |
|               | shell3      | 43.4    | 3.5            |
|               | shell4      | 46.1    | 10.0           |
|               | total shell |         |                |
|               | star        |         |                |
| <i>b</i>      | shell4      | 46.1    | 10.0           |
|               | star        |         |                |

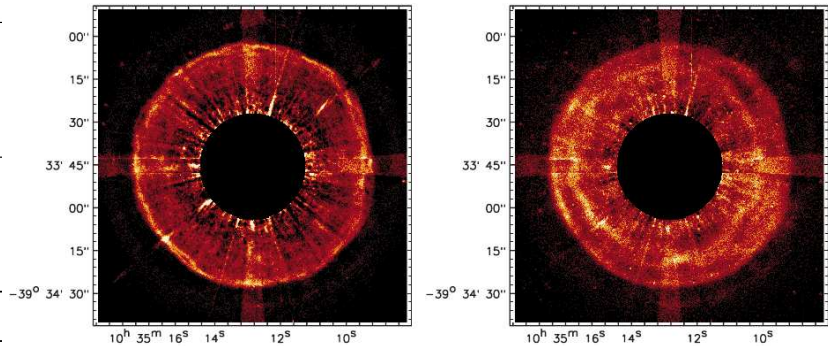


Figure 3.3: Table of detected shells in different filters and observations of U Ant in scattered light in the KI (left) and NaD filters with black masked regions, [González Delgado et al., 2001].

### Imaging polarimetry of stellar light scattered in detached shells around the carbon stars R Scl and U Ant

[González Delgado et al., 2003]

A re-observation of U Ant with imaging polarimetry was done in the filter of resonance lines of Na and K. The dominating shell at radius 43 arcsec, which is known from observations in CO and scattered light, is verified again. In addition with the gathering of polarized scattered light a further shell at  $\sim 50$  arcsec was detected.

### The detached dust and gas shells around the carbon star U Antliae

[Maercker et al., 2010]

Two detached shells with overall spherical geometry were found around the carbon star U Ant and further arc-like structures at 25 arcsec and 37 arcsec were also detected. The inner shell is located at a radius of  $\sim 43$  arcsec (width  $\sim 2$  arcsec) and the outer shell at  $\sim 50$  arcsec (width  $\sim 7$  arcsec).

Previous observations in CO radio line data confirm the inner shell, but not the outer shell. Furthermore the method to detect the detached shells consists of polarization data on stellar light scattered in the circumstellar material around the target star. Additionally the filters contain no strong lines, which make it possible to determine between two scattering agents like dust and gas. To derive the expansion velocity of the shells the echelle spectrograph with KI (Kalium) and NaD lines on the ESO New Technology Telescope (NTT) was used.

With all these observations a schematic overview (Fig. 3.4) of the shells can be made:

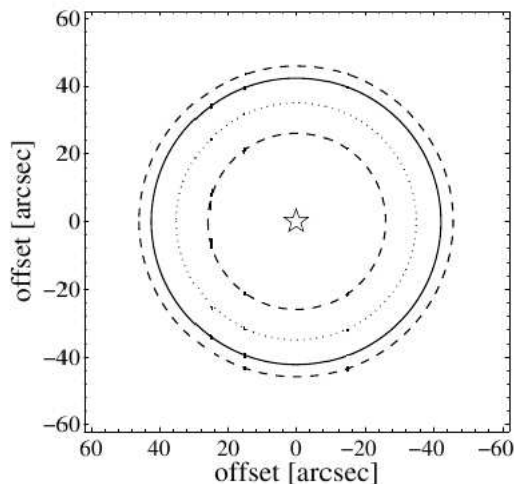


Figure 3.4: Four main shells after [Maercker et al., 2010].

Shell 1 (25 arcsec) and 2 (37 arcsec) are shell-like structures like arcs, which are close to the star, but not centred to it. The interpretation of these shells is currently (2009) unknown and they can be assumed in the SPIRE radial profiles (chapter Science data results at section radial profiles of U Ant).

Shell 3 (43 arcsec) consists mainly of gas with an estimated shell mass of  $2 \times 10^{-3} M_{\odot}$  with an expansion velocity of  $19.5 \text{ km s}^{-1}$ , which was also derived with the CO-line. The shell age is estimated to 2700 years.

Shell 4 (50 arcsec) is a dust shell with a mass of  $5 \times 10^{-5} M_{\odot}$ .

Both shells (3 and 4) show a clumpy structure due to their variations in the intensity.

The existence of gas and dust shell can be explained as single event, where the dust is moving in front of the gas shell with a slightly larger expansion velocity [Gonzalez Delgado et al., 2003] (drift velocity  $\sim 2.8 \text{ km s}^{-1}$ ).

As it was already proposed by [Olofsson et al., 1990] that geometrically-thin and detached shells have to form during a thermal pulse by a stellar temperature and luminosity change leading to an increased mass-loss.

But hydrodynamical models by [Steffen et al., 1998] showed that these shells will diffuse. A more promising interpretation would be a wind-wind interaction, where a stellar wind collides with an old wind of lower velocity [Steffen and Schönberger et al., 2000].

**The detached dust shells of AQ Andromedae, U Antliae, and TT Cygni**  
[Kerschbaum et al., 2010], Baumann also as co-author

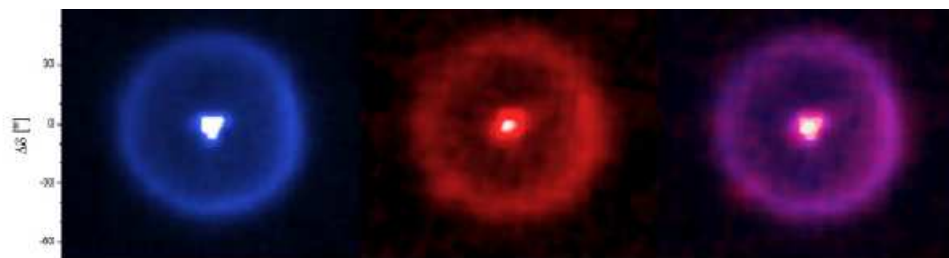


Figure 3.5: Herschel-PACS U Ant observations (left to right) in blue ( $70 \mu\text{m}$ ), red ( $160 \mu\text{m}$ ) and the composite, [Kerschbaum et al., 2010].

U Ant was observed (Fig. 3.5) with the instrument PACS (Photodetector Array Camera and Spectrometer) on the Herschel Space Telescope at 70 and 160 micron. The detached shell, which was intensively studied using CO-line radio data and imaging in scattered light, was also confirmed with PACS.

Furthermore the detection of gas and dust at the same location indicates that both scatter agents occupy the same space. The detached shell (Fig. 3.7) is located at 42 arcsec (shell 3: [Kerschbaum et al., 2010]; mainly gas) and probably originates from a brief increase in mass-loss 2800 years ago.

[Izumiura et al., 1997] traced an extended emission (Fig. 3.6) at 3 arcmin at 100 micron (IRAS), but this emission is only partly visible in PACS (70 micron). A DUSTY modeling with amorphous carbon with grain radius  $0.05 \mu\text{m}$  (1D radiative transfer code) and external radiation [Aringer et al., 2009] leads to the fitting results shown in Table 3.1.

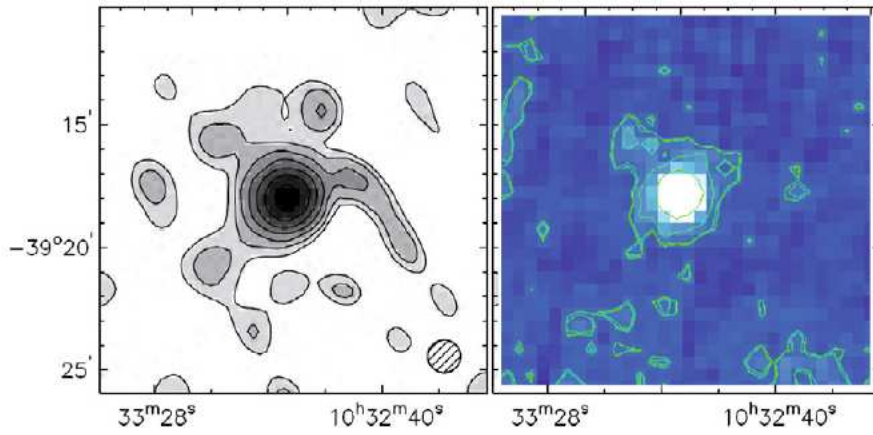


Figure 3.6: Extended emission of U Ant ( $\sim 3$  arcmin): left: HIRAS image ( $100 \mu\text{m}$ ), right: rebinned PACS image ( $70 \mu\text{m}$ ), [Izumiura et al., 1997] and [Kerschbaum et al., 2010].

| $\dot{M}_a$ [ $M_{\odot} \text{ yr}^{-1}$ ] | $\dot{M}$ [ $M_{\odot} \text{ yr}^{-1}$ ] | L [ $L_{\odot}$ ] | M [ $M_{\odot}$ ]   |
|---|---|-------------------|---------------------|
| $1 \cdot 10^{-10}$                          | $7 \cdot 10^{-7}$                         | 8 000             | $3.8 \cdot 10^{-5}$ |

Table 3.1: DUSTY fitting results of U Ant, [Kerschbaum et al., 2010]

$\dot{M}_a$  ... actual mass-loss rate,  $\dot{M}$  ... mass-loss rate of the detached shell,  
L ... luminosity, M ... total dust and gas mass-loss.

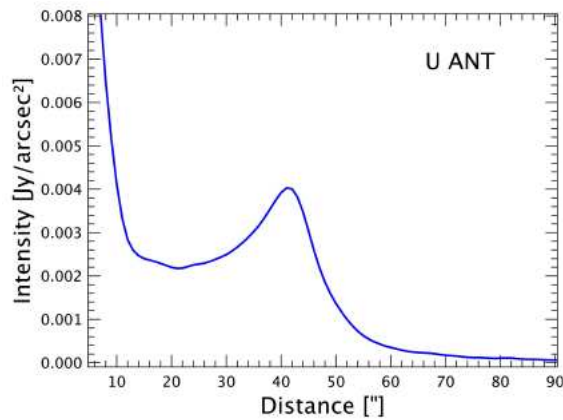


Figure 3.7: Radial profile of U Ant; Intensity [ $\text{Jy per arcsec}^2$ ] vs distance [arcsec] detached shell intensity peak at 42 arcsec.

## 3.2 AQ And

### 3.2.1 Properties and features

The spectral type of AQ And is C5,4 (carbon star, GCVS), which has an effective temperature of 2660 K [Bergeat and Chevallier, 2005]. In addition its variability is classified as semi-regular variable (SRB), which defines poorly periodicity with alternating intervals of periodic and slow irregular changes. Its period is estimated to a multi period of 169 and 346 days [Kiss et al., 1999]. Revised Hipparchos measurements by [Bergeat and Chevallier, 2005] result in a distance of 1015 pc. The luminosity was calculated to  $12000 L_{\odot}$  in the same way as U Ant through SED fitting by [Kerschbaum et al., 2010]. In the publication by [Bergeat and Chevallier, 2005] the absolute bolometric magnitude is -5.24.

The location of AQ And is the constellation Andromeda at coordinates RA 00 h 27 m 31.68373 s and DEC  $+35^{\circ} 35' 14.5034''$  (ICRS, J2000, [van Leeuwen, 2007]). In addition the proper motions are estimated to -4.09 mas/yr in RA and -12.49 mas/yr in DEC. The value for the radial velocity was obtained from the General Catalogue of Radial Velocities (GCRV) [Wilson, 1953] and amounts to -14 km/s.

[Young et al., 1993] detected an extended emission at 3.3 arcmin in IRAS 60  $\mu\text{m}$ , but this emission is very weak, so it is at the detection limit.

In the year 1996 to 2003 CO-observations by [Olofsson, priv. comm.] led to a non-detection of shell-like structures. For the first time the Herschel-PACS observations [Kerschbaum et al., 2010] revealed a detached shell at 52 arcsec. Further extended emission was detected in 60  $\mu\text{m}$  with ISO (Fig. 3.10) but only with low resolution. The 52'' shell suggests a brief mass-loss some 19 000 years ago with a mass-loss variation every 2000 and 5000 years due to the intensity peaks in the radial profile (Fig. 3.11). Additional output parameters through modeling by [Kerschbaum et al., 2010] estimate the dust temperature of the 52 arcsec shell to 27.9 until 44.8 K with a mass-loss of 0.3 until  $152 \cdot 10^{-7} M_{\odot}$  per year by assuming an optically thin detached shell.

### 3.2.2 Publication overview

The available publications about shell detection and other extended structures for the science object AQ And are listed and discussed.

CO observations and re-observations by Olofsson et al. in 1996 until 2003 [Olofsson, priv. comm.] showed no detached shells around AQ And. This could be explained due to photo dissociation and resolution problems in connection with the far distance.

#### Circumstellar Shells Resolved in the IRAS Survey Data. I. Data Processing Procedure, Results, and Confidence

[Young et al., 1993]

The IRAS data was analysed by fitting a central unresolved source with a resolved isothermal dust shell.

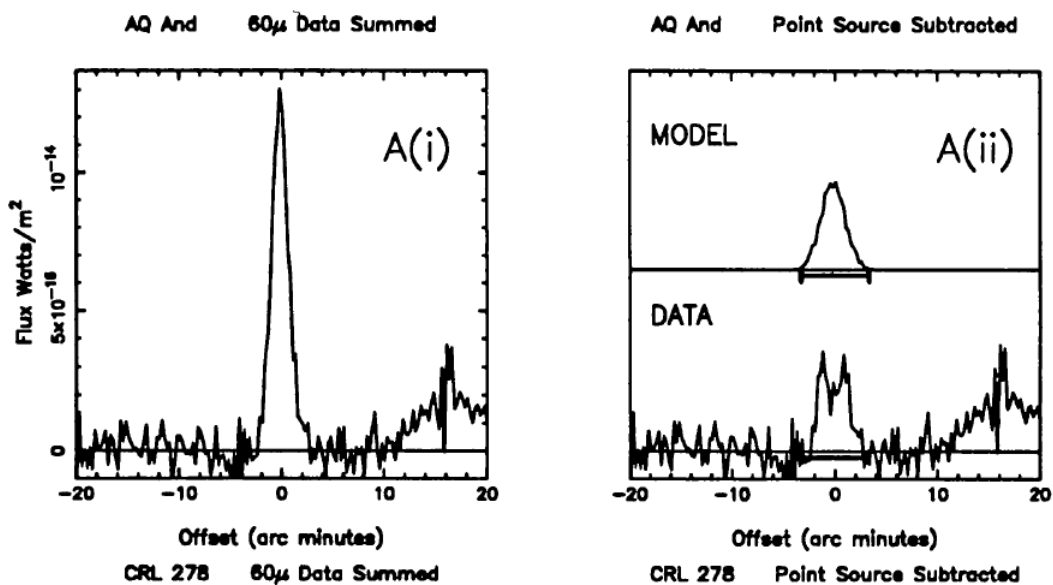


Figure 3.8: Fitted IRAS data ( $60 \mu\text{m}$ ) with the Model Fitting Program (MFP), [Young et al., 1993].

In the left plot (flux vs offset distance) in Fig. 3.8 the raw data is shown with 0.25 arcmin bins. The right panel is the best-fit model for extended emission compared with the Calibrated Raw Detector Data (CRDD) data from IRAS (with point source subtracted). As a result extended emission at  $\sim 3.3$  arcmin radius at  $60 \mu\text{m}$  is detected.

**The detached dust shells of AQ Andromedae, U Antliae, and TT Cygni**  
 [Kerschbaum et al., 2010], Baumann Bernhard also as co-author

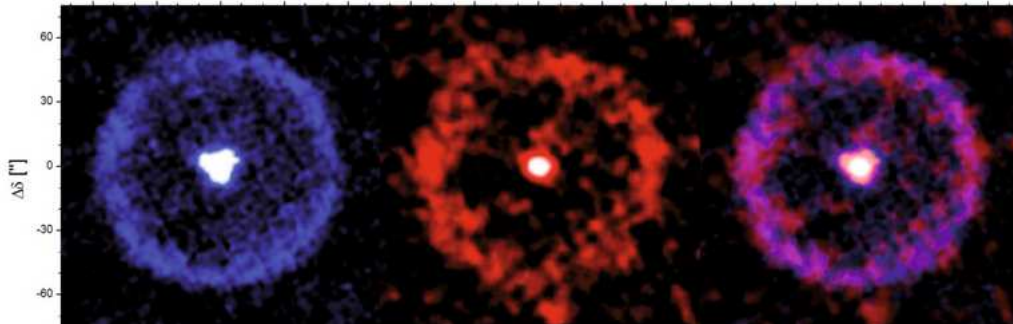


Figure 3.9: Herschel-PACS AQ And observations (left to right) in blue ( $70 \mu\text{m}$ ), red ( $160 \mu\text{m}$ ) and the composite, [Kerschbaum et al., 2010].

Through PACS-imaging a thin detached shell (Fig. 3.9) at 52 arcsec radius was detected, but CO observations and re-observations by Olofsson et al (priv. comm., 1996 - 2003) showed no shells or shell-like structures. An interpretation may be the occurrence of photo-dissociation or the detection limitation due to the large distance and large physical extension of the shell.

There was also no detection of extended emission at 3.3 arcmin [Young et al., 1993], which could be either caused by the PACS reduction process, in which the faint emission was removed, or by background contamination of the IRAS maps. On an ISO-PHOT map (Fig. 3.10) at  $60 \mu\text{m}$  extended emission is comparable with the shell found at 52 arcsec, keeping in mind ISO-PHOT's lower resolution.

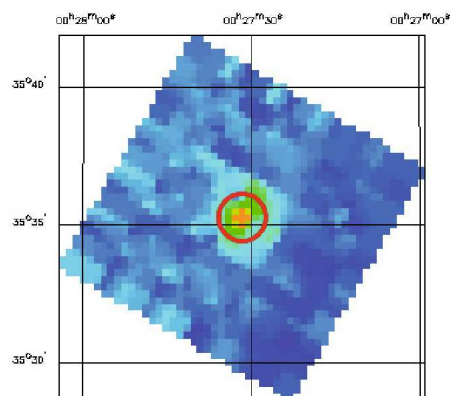


Figure 3.10: ISO-PHOT (PHT22) observation (FWHM  $\sim 35 - 40$  arcsec) of AQ And: the red circle indicates the detached shell at 52 arcsec from PACS.

The radial profile (Fig. 3.11) of AQ And is not smooth at all, there are intensity peaks at

the inner part of the ring, which could be explained by variation in mass-loss over time. Furthermore the old mass-loss is estimated to an age of 19000 years with a variation every 2000 and 5000 years.

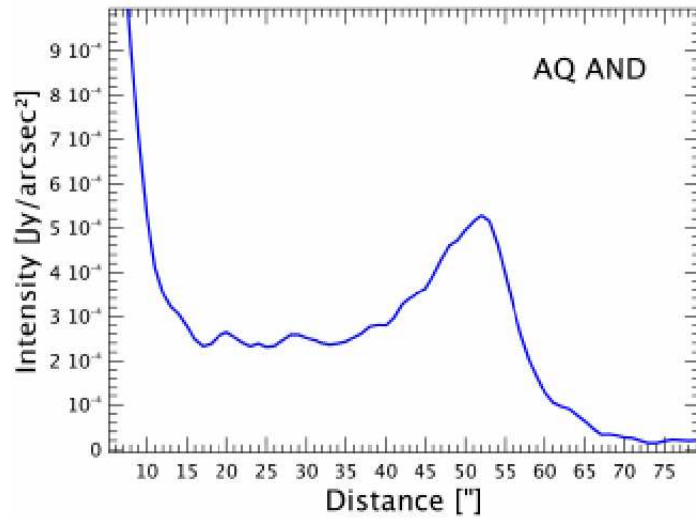


Figure 3.11: Radial profile of AQ And; Intensity [Jy per arcsec<sup>2</sup>] vs distance [arcsec] detached shell intensity peak at 52 arcsec.

A DUSTY modeling with amorphous carbon with grain radius  $0.05 \mu\text{m}$  (1D radiative transfer code) and external radiation (Aringer et al., 2009) leads to the following fitting results as shown in Table 3.2.

| $\dot{M}_a$ [ $M_\odot \text{ yr}^{-1}$ ] | $\dot{M}$ [ $M_\odot \text{ yr}^{-1}$ ] | L [ $L_\odot$ ] | M [ $M_\odot$ ]    |
|---|---|-----------------|--------------------|
| $1 \cdot 10^{-10}$                        | 0.3 to $152 \cdot 10^{-7}$              | 12 000          | $20 \cdot 10^{-3}$ |

Table 3.2: DUSTY fitting results of AQ And, [Kerschbaum et al., 2010]

$\dot{M}_a$  ... actual mass-loss rate,  $\dot{M}$  ... mass-loss rate of the detached shell,  
L ... luminosity, M ... total dust and gas mass-loss.



## 4 Science data results

For each object the chapter “PACS and SPIRE observations” presents the reader the final maps from SPIRE and PACS observations and their radial profiles, which are used to compare the observation with the DUSTY modeling (chapter 4.1.3 and 4.2.3). The chapter “Photometry and flux determination” describes how the aperture photometry was performed and how the flux density was calibrated and measured. After the modeling chapter the conclusion and interpretation per object is discussed.

### 4.1 U Ant

#### 4.1.1 PACS and SPIRE observations

The PACS final maps (Fig. 4.1(a) and Fig. 4.1(c)) in Fig. 4.1 were created by ScanAm version 13 with the built-in calTree provided in the object data.

The SPIRE maps were reduced with HIPE (version 8.0.3282, calTree 8.1) and ScanAm (version 13) in the highest possible resolution without visible artefacts like stripes.

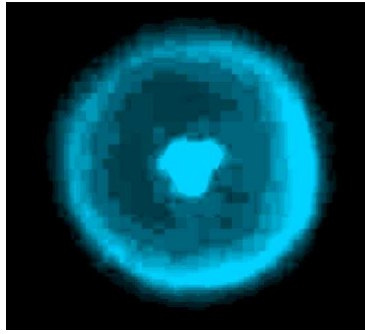
The radial profiles of PACS (Fig. 4.1(b) and Fig. 4.1(d)) and SPIRE (Fig. 4.3(b), Fig. 4.3(d) and Fig. 4.3(f)) are created by taking the azimuthal averaged value from all the pixels in the appropriate radius.

First the task sourceFitting (description; chapter 4.1.2) was started to derive the accurate centre. The end product is the plot of the intensity per square arcsec versus the distance in arcsec.

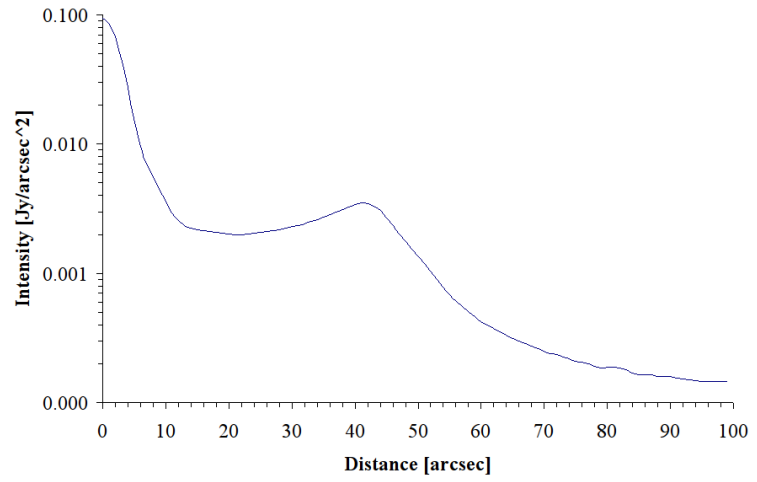
The blue map of PACS (Fig. 4.1(a)) and the radial profile (Fig. 4.1(b)) show a clearly recognizable detached shell at 42 arcsec radius, which was confirmed several times by [Kerschbaum et al., 2010], [González Delgado et al., 2001] and [Maercker et al., 2010]. On the right side the shell is thicker, but this is not due to its proper motion into the ISM.

At the red channel (Fig. 4.1(c) and Fig. 4.1(d)) the detached shell is comparable to the blue one, but it is more fainter and knotty.

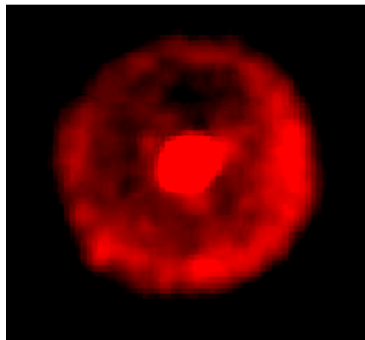
Additional shells at 46” ([Izumiura et al., 1997], [González Delgado et al., 2001]), 50” ([Arimatsu et al., 2011], [Maercker et al., 2010]) were not detected and no intensity peaks were found. Arc-like structures at 25” and 37” as found by [González Delgado et al., 2001] and [Maercker et al., 2010] are not visible in the radial profiles (Fig. 4.1(b) and Fig. 4.1(d)) and in the maps Fig. 4.1(a) and Fig. 4.1(c) the inner parts of the star until  $\sim 15$ ” are dominated by the PSF of Herschel (Fig. 4.2) and thus not informative.



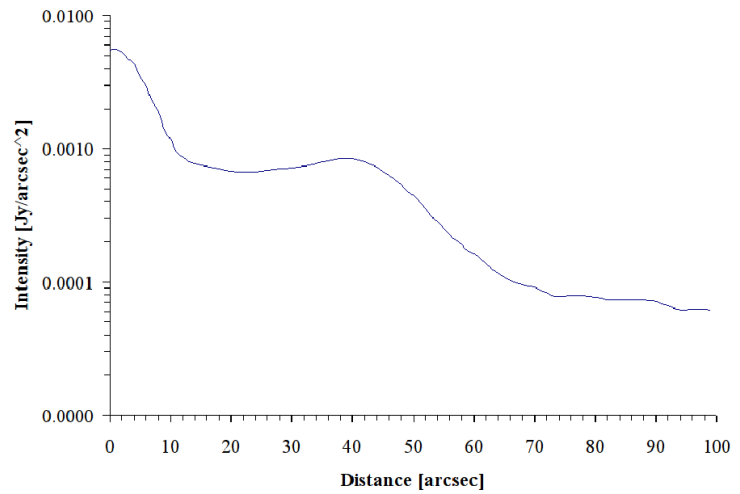
(a) blue:  $70 \mu\text{m}$ , detached shell at  $42''$ , 1 pixel = 1 arcsec, FOV:  $\sim 2$  arcmin.



(b) Radial profile in blue ( $70 \mu\text{m}$ ).



(c) red:  $160 \mu\text{m}$ , detached shell at  $42''$ , 1 pixel = 2 arcsec, FOV:  $\sim 2$  arcmin.



(d) Radial profile in red ( $160 \mu\text{m}$ ).

Figure 4.1: PACS observations of U Ant in  $70 \mu\text{m}$  (Fig. 4.1(a)) and  $160 \mu\text{m}$  (Fig. 4.1(c)) and their corresponding radial profiles (Fig. 4.1(b) and Fig. 4.1(d)).

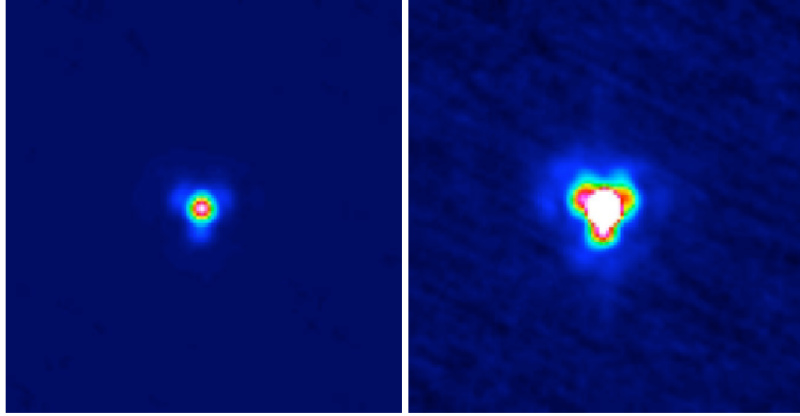


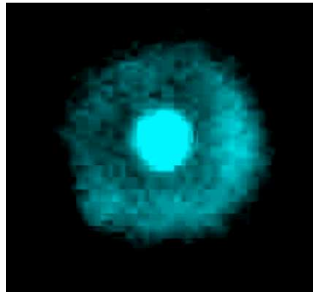
Figure 4.2: Herschel PSF in blue ( $70 \mu\text{m}$ ) at PACS, tri-lobe pattern of the point spread function (PSF) of the herschel optics, left: a linear scale up to the peak, right: 10 % of the peak is shown, others are saturated

In Fig. 4.3 the detached shell is recognisable, but is more flattened and flocculent than in the PACS maps because of the low resolution, the bigger FOV and the sky background contamination. An important point is that the detached shell in the radial profile (Fig. 4.3(b)) is located at  $\sim 36''$ , not at  $42''$ . Thus it could indicate a shell-like structure like in [González Delgado et al., 2001] and [Maercker et al., 2010], which is super-positioned with the shell at  $42''$ .

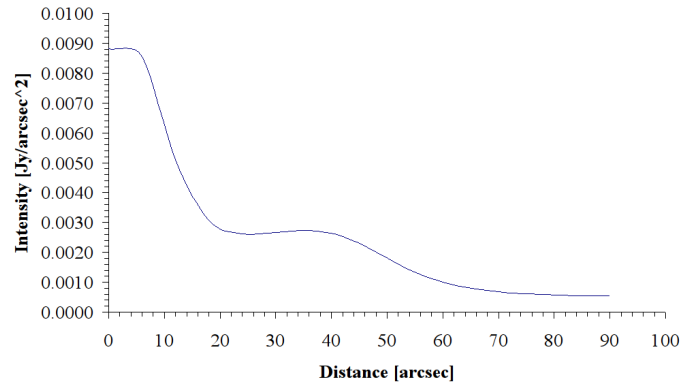
In Fig. 4.3(d) a weak peak at  $40''$  indicates the faint detached shell. There are no additional peaks present, which would indicate additional shells or arcs.

The detached shell is only rudimentarily visible in Fig. 4.3(e) and thus not visible in the radial profile (Fig. 4.3(f)), only a flattened descent to the sky background. Furthermore it is difficult to distinguish between star and shell intensity in Fig. 4.3(e).

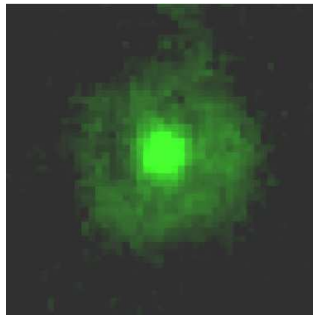
In addition no further shells, mentioned in the discussion of the PACS observations, were visible in Fig. 4.3(a), Fig. 4.3(c) and Fig. 4.3(e) and their radial profiles (Fig. 4.3(b), Fig. 4.3(d) and Fig. 4.3(f)).



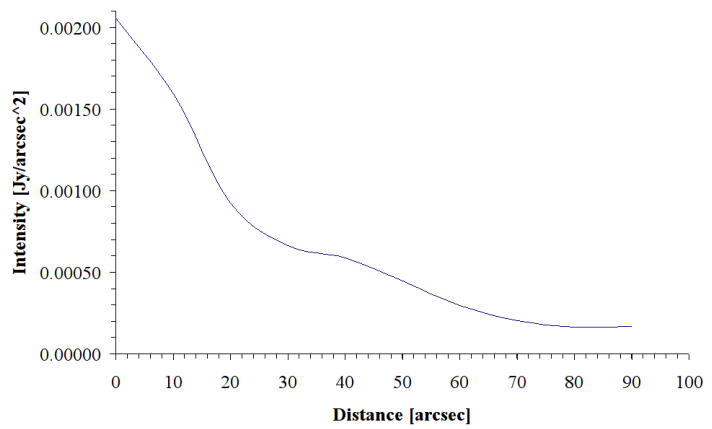
(a) blue: 250  $\mu\text{m}$ , detached shell, 1 pixel = 3 arcsec, FOV:  $\sim 2$  arcmin



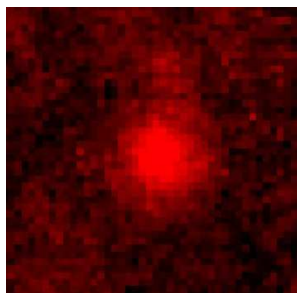
(b) Radial profile in blue (250  $\mu\text{m}$ ).



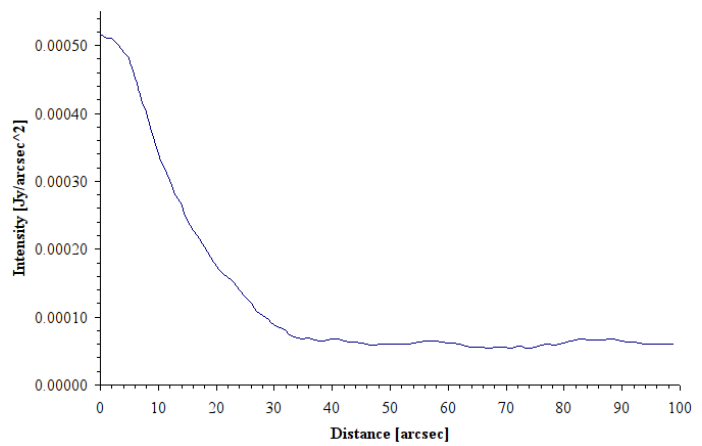
(c) green: 350  $\mu\text{m}$ , detached shell, 1 pixel = 4 arcsec, FOV:  $\sim 2$  arcmin.



(d) Radial profile in green (350  $\mu\text{m}$ ).



(e) red: 500  $\mu\text{m}$ , detached shell, 1 pixel = 7 arcsec, FOV:  $\sim 2$  arcmin



(f) Radial profile in red (500  $\mu\text{m}$ ).

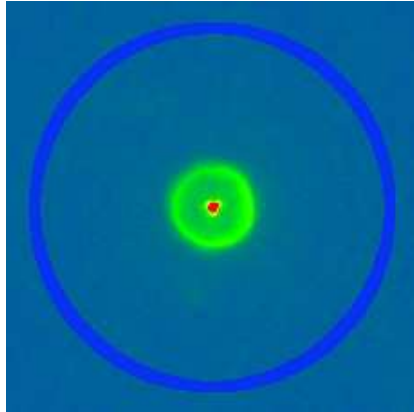
Figure 4.3: SPIRE observations of U Ant in 250  $\mu\text{m}$  (Fig. 4.3(a)), 350  $\mu\text{m}$  (Fig. 4.3(c)) and 500  $\mu\text{m}$  (Fig. 4.3(e)) and their corresponding radial profiles (Fig. 4.3(b), Fig. 4.3(d) and Fig. 4.3(f)).

The cut levels (pixel value distribution) in the images in Fig. 4.4 were set accordingly to saturate the science object and to reveal the background emission.

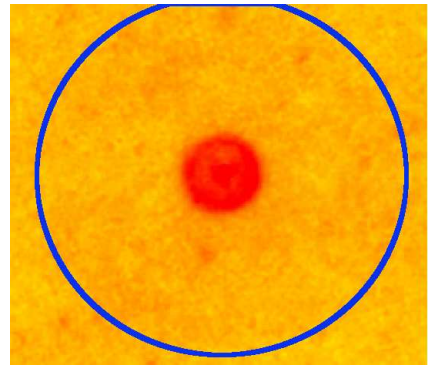
The sky background in Fig. 4.4(a) and Fig. 4.4(b) is very flattened and no extended emission ([Izumiura et al., 1997], Fig. 3.2) at the outside at 3 arcmin (blue circles; Fig. 4.4) is recognizable. The PACS background is generally very smooth in both objects, so there is the possibility that the extended emission was removed during the reduction process, because in [Kerschbaum et al., 2010] the extended emission is partly visible.

Furthermore the SPIRE observations (Fig. 4.4(c), Fig. 4.4(d) and Fig. 4.4(e)) revealed faint extended emission around the object together with back- and foreground stars. But this extended emission cannot be determined with certainty because of the faintness. That's why the SPIRE maps were recreated and rechecked with the lower resolution (30") of the IRAS mission.

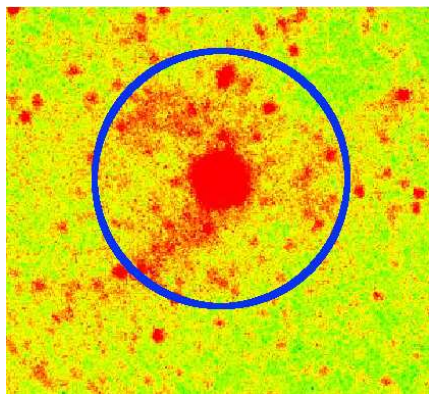
In Fig. 4.5 the rebinned SPIRE maps reveal partly the extended emission at 3 arcmin, which was detected by [Kerschbaum et al., 2010] in PACS and by [Izumiura et al., 1997] in IRAS. The appearance of the emission is a (red) arc, which can be observed in SPIRE blue Fig. 4.5(a) at strongest and fainter in Fig. 4.5(b) and Fig. 4.5(c).



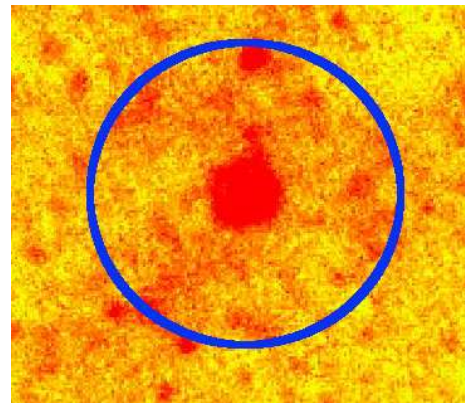
(a) blue:  $70 \mu\text{m}$ , 1 pixel = 1 arcsec, FOV:  $\sim 7$  arcmin.



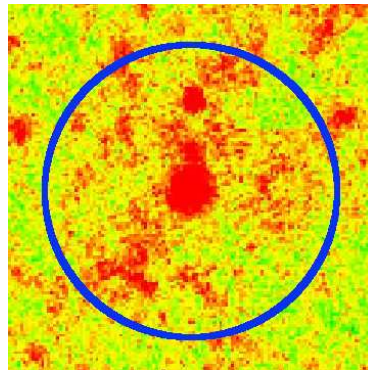
(b) red:  $160 \mu\text{m}$ , 1 pixel = 2 arcsec, FOV:  $\sim 7$  arcmin.



(c) blue:  $250 \mu\text{m}$ , 1 pixel = 3 arcsec, FOV:  $\sim 10$  arcmin.

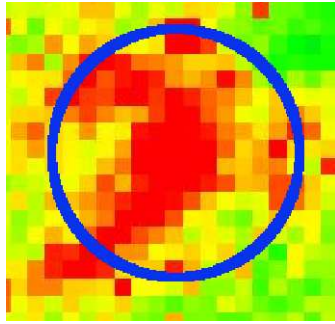


(d) green:  $350 \mu\text{m}$ , 1 pixel = 4 arcsec, FOV:  $\sim 8$  arcmin.

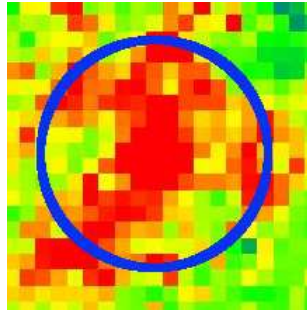


(e) red:  $500 \mu\text{m}$ , 1 pixel = 7 arcsec, FOV:  $\sim 7$  arcmin

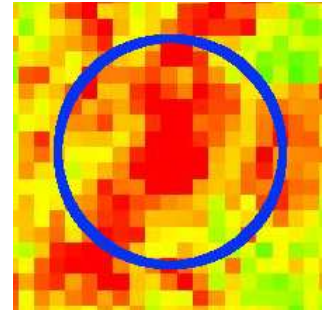
Figure 4.4: Sky background around U Ant of PACS (Fig. 4.4(a) and Fig. 4.4(b)) and SPIRE (Fig. 4.4(c), Fig. 4.4(d) and Fig. 4.4(e)) observations. The blue circle indicates the extended emission at 3 arcmin (Fig. 3.2) of the IRAS mission by [Izumiura et al., 1997].



(a) blue: 250  $\mu\text{m}$ ,  
1 pixel = 30 arcsec, FOV:  
 $\sim 8$  arcmin.



(b) green: 350  $\mu\text{m}$ ,  
1 pixel = 30 arcsec, FOV:  
 $\sim 8$  arcmin.



(c) red: 500  $\mu\text{m}$ ,  
1 pixel = 30 arcsec, FOV:  
 $\sim 8$  arcmin

Figure 4.5: Sky background around U Ant of SPIRE-observations (Fig. 4.5(a), Fig. 4.5(b) and Fig. 4.5(c)) rebinned to the lower resolution of IRAS. The blue circle indicates the extended emission at 3 arcmin (Fig. 3.2) of the IRAS mission by [Izumiura et al., 1997].

### 4.1.2 Photometry and flux determination

The flux calibration was obtained from the SPIRE Observer’s manual, which is provided at the ESA Herschel Website, [ESA, 2012a].

The calibration is performed at the stage of the detector timelines (Level 1 data) under assumptions of a point source observation in each monochromatic detector array (250  $\mu\text{m}$ , 350  $\mu\text{m}$ , 500  $\mu\text{m}$ ).

In the final maps (Level 2 data) from the SPIRE pipeline the flux density’s unit is not like as for PACS in Jansky(Jy) (summed pixel unit in the photometry) or Jy per pixel (single pixel unit), but in Jy  $\cdot$  pixel per beam (averaged pixel unit in the photometry) or Jy per beam (single pixel unit).

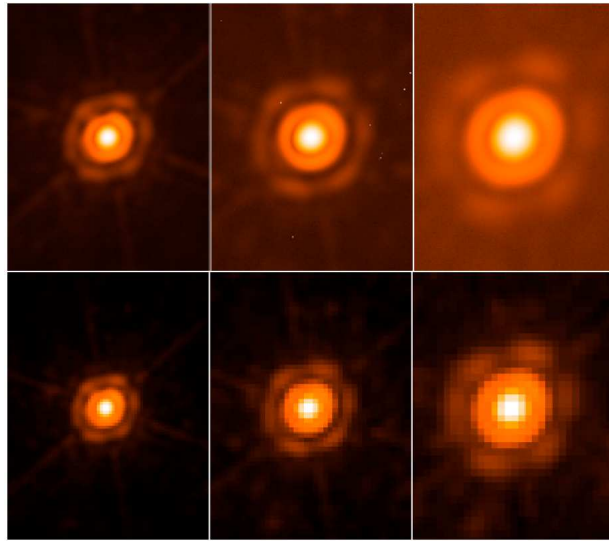


Figure 4.6: Beam models (10 x 30 arcmin) from the planet Neptune for 250  $\mu\text{m}$ , 350  $\mu\text{m}$ , 500  $\mu\text{m}$  (left to right), upper panel: high resolution beam with 1 arcsec, bottom panel: standard resolution: 6, 10, 14 arcsec.

The calibrated beam maps for each detector(Fig. 4.6) were performed by a fine scan of the planet Neptune, where each bolometer scanned Neptune in four different directions to derive two sets of maps for each bolometer. Because of the gathering of this data the point source response function per bolometer and additional scanning artefacts could be calculated by the technicians.

The Full Width Half Maximum (FWHM) (Fig. 4.7) values are derived by fitting an asymmetric 2D Gaussian to the beam maps. As noticeable in Fig. 4.7 the FWHM and beam area increase with the pixel size, and so it is dependent on the pixel scale.

When the beam area is increasing, the photometry for measuring the surface brightness is less reliable at larger pixel scales and so correction factors must be applied.



| Pixel size | Band              | Major FWHM         | x | Minor FWHM | Geometric mean FWHM | Ellipticity | Average beam area                            |
|------------|-------------------|--------------------|---|------------|---------------------|-------------|--|
| (arcsec)   | ( $\mu\text{m}$ ) | (arcsec)           |   | (arcsec)   | (arcsec)            | (%)         | (arcsec) <sup>2</sup> (sr $\times 10^{-8}$ ) |
| 1          | 250               | 18.3 $\times$ 17.0 |   | 17.6       | 17.6                | 8.1         | 423 0.9942                                   |
| 1          | 350               | 24.7 $\times$ 23.2 |   | 23.9       | 23.9                | 6.6         | 751 1.765                                    |
| 1          | 500               | 37.0 $\times$ 33.4 |   | 35.2       | 35.2                | 10.9        | 1587 3.730                                   |
| 6          | 250               | 18.7 $\times$ 17.5 |   | 18.1       | 18.1                | 7.4         | 447 1.051                                    |
| 10         | 350               | 25.6 $\times$ 24.2 |   | 24.9       | 24.9                | 6.1         | 816 1.918                                    |
| 14         | 500               | 38.2 $\times$ 34.6 |   | 36.4       | 36.4                | 10.1        | 1711 4.022                                   |

Figure 4.7: Basic beam parameters (uncertainties under 1 %) for high-resolution maps (1 arcsec) and standard resolution: 6, 10, 14 arcsec.

The flux density value depends on the square of the ratio of the FWHM of the beam and the pixel size of the map. Each pixel in the SPIRE map represents the averaged Jy per beam flux density (PACS: summed Jy per pixel) which was measured by the detector during the pointing.

It is highly recommended to use the standard resolutions and appropriate beam sizes per detector array (6, 10, 14 arcsec) for the photometry because of the calculation of the correction factors and accuracy.

X ... measured flux density in Jy  $\cdot$  pixel per beam

Y ... wanted flux density in Jy

### Symmetric Gaussian beam

$$Y = X \cdot \frac{4 \cdot \ln(2)}{\pi \cdot \left(\frac{\text{FWHM}}{\text{pixel size}}\right)^2} \quad (4.1)$$

where:

$$\text{beam area} = \frac{\pi \cdot \left(\frac{\text{FWHM}}{\text{pixel size}}\right)^2}{4 \cdot \ln(2)} \quad (4.2)$$

The needed parameters for the flux calibration for each detector are summarized in Table 4.1.

| detector | wavelength [ $\mu\text{m}$ ] | pixel size [arcsec] | beam size [arcsec] | corr. multiplier |
|----------|------------------------------|---------------------|--------------------|------------------|
| blue     | 250                          | 6                   | 18.1               | 1.02             |
| green    | 350                          | 10                  | 25.2               | 1.05             |
| red      | 500                          | 14                  | 36.6               | 0.94             |

Table 4.1: SPIRE detector properties and correction multipliers.

### Accuracy

The absolute calibration accuracy depends on the beam maps, which were obtained from the calibration source Neptune =>  $\approx \pm 5\%$ .

Furthermore the relative calibration uncertainty results from the comparison of a science observation and the calibrator Neptune, which is done in the SPIRE pipeline process (voltage to flux density parameters and much more). It is assumed as random contribution with less than 2 % in all bands.

For the calibration an overall accuracy of  $\pm 7\%$  for the SPIRE photometer is advisable.

Another uncertainty belongs to the photometric part, which relies mostly on the user's settings (e.g. aperture size, sky annulus).

In the timeline products there are random detector noise and additional noise from astrometric errors due to the combining in map making.

But the dominant part in photometry is the choice of the parameters in the aperture photometry and source fitting problems in crowded regions. As well as different types of deglitching and baseline removal can change the flux density to an amount of a few percent. When there are no sky background fluctuations and an undisturbed science object without fore- and background stars or interstellar clouds, the calibration error will dominate in this situation. Otherwise at crowded regions and with a noisy sky, the user can enhance the photometry with the choice of the best fit parameters in the aperture photometry and sourcefitting task.

The overall uncertainty of the flux density can be estimated to  $\pm 10\%$  until  $\pm 15\%$ .

### Determination of the flux density with the aperture photometry

For testing and validation purposes of the flux calibration a SPIRE publication with performed aperture photometry by [van Hoof et al., 2010] was consulted. The different flux densities for 250  $\mu\text{m}$ , 350  $\mu\text{m}$  and 500  $\mu\text{m}$  with the given aperture sizes were measured, calibrated and compared with the values of the publication.

The essentials of this publication are given below.

A ring nebula NGC 6720 was observed with the Herschel PACS and SPIRE instruments, which revealed a similarity between dust distribution and the  $\text{H}_2$  emission. That could be an evidence for forming  $\text{H}_2$  on dust grains.

The data from the publication were reduced with the calibration tree version 5 and with HIPE functions.

For the flux density comparison the SPIRE images were processed, but with calibration tree version 8.1 and the ScanAmorphos package version 13. The difference of the calibration version and reduction method should only vary under 1 % and this is in range of the flux density uncertainty (10 - 15 %).

### Aperture photometry of NGC 6720 for the SPIRE detectors

The standard reduction process was performed and then ScanAmorphos was used for creating the maps with standard resolution in each detector.

Example: Object: NGC 6720 (Ring Nebula)

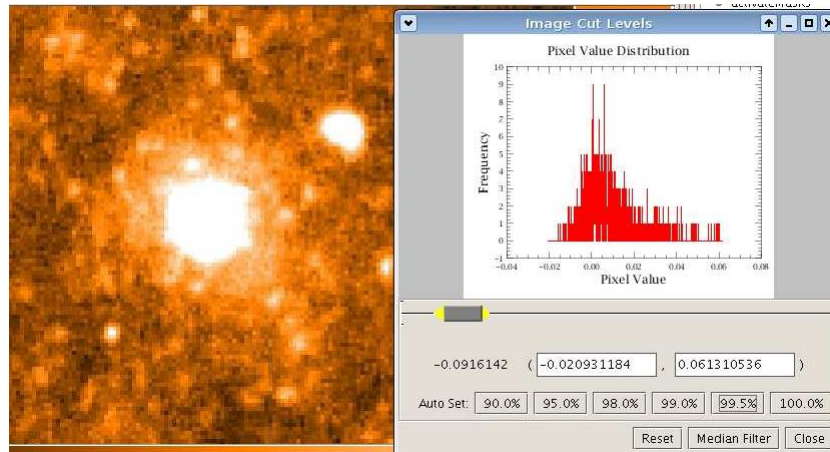


Figure 4.8: SPIRE map blue: 6 arcsec per pixel, FOV:  $\sim 39 \times 44$  arcmin with the pixel value distribution, default: 99.5 % pixels included.

Map Fig. 4.8 shows the object NGC 6720 (ring nebula) within a field of view (FOV) of  $\sim 39 \times 44$  arcmin and the HIPE cut level selection window (pixel value distribution), in which different pixel values can be included and excluded to detect faint emission (default: 99.5 pixels are included). In the map the standard setting is not optimal, whereas in Fig. 4.9 at cut level 100 % the ring nebula is visible.



Figure 4.9: SPIRE map blue: 6 arcsec per pixel, FOV:  $\sim 31 \times 27$  arcmin

HIPE (version 8.0.3282) with task “annularSkyAperturePhotometry” is applied on all three final maps.

The photometry can be either measured with the GUI through target selecting with the mouse or in the command line.

For the photometry the parameters like the aperture radius (in pixel or arcsec), the sky annulus (start and end point in pixel), the algorithm for the sky estimation (average, median, mean-median, the synthetic mode and daophot) and of course the image map, must be supplied.

The mean-median was used, which calculates the average of all the values closer to the median.

In the GUI (Fig. 4.10) the choice “centroiding” selects the target’s centre (pixel) with a mouse click (for the commandline input the centre coordinates are required too).

Commandline: Task “annularSkyAperturePhotometry”:

The centre coordinates can be either determined by hand in the picture with the mouse pointer and read out from the picture display at HIPE or with the task “sourceFitting”.

A 2D Gaussian will be fitted to the desired source and the user selects the appropriate rectangular region in the map.

Further parameters can be set for the shape (elongated or circular Gaussian) and the background (slope or drop).

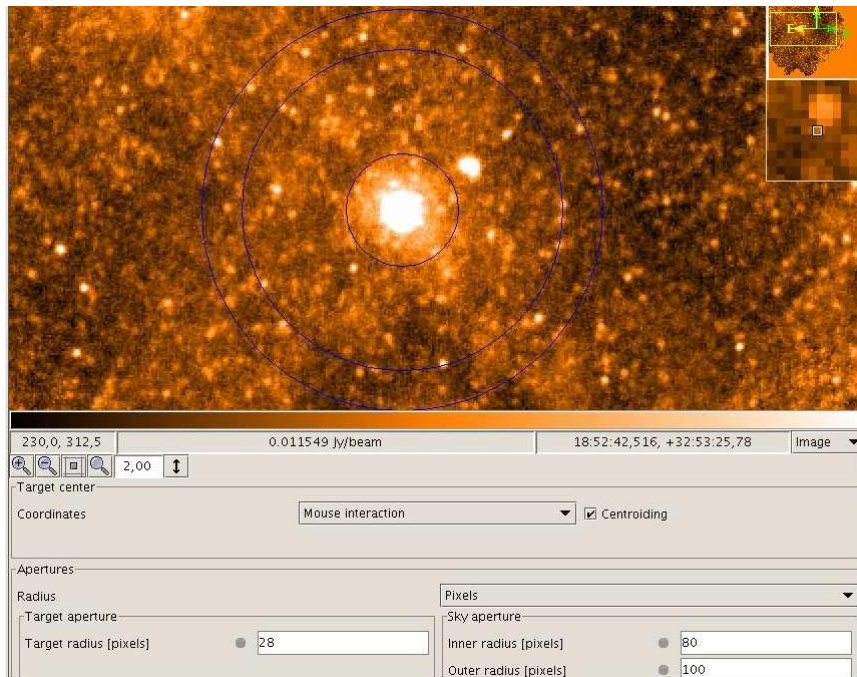


Figure 4.10: Aperture photometry of NGC 6720 with an aperture of 168 arcsec (28 pixel).

This is an example for the sourceFitting process:

```
parameters = sourceFitting(elongated = True, slope = False, \
image = myImage, minX = 74.19, minY = 116.65, width=29.67, \
height = 26.60)
```

In the variable “parameters” the properties of the fitted 2D Gaussian (e.g. the centre coordinates) are stored.

With the next command, the aperture photometry is performed.

```
# The target centre specified in pixel coordinates, the radii in pixels
# and using fractional pixels
result = annularSkyAperturePhotometry(image=NGC6720_spire250, \
centerX=202.7932030703474, centerY=314.0991469646303, centroid=True, \
radiusPixels=28.0, innerPixels=80.0, outerPixels=100.0, fractional=1, \
algorithm=2)
```

The averaged pixel will be summed up within the aperture radius in relation to the sky estimation. As result a data structure with the target-, sky-flux density and their subtraction is stored.

The measured flux density can be used for further analysis (flux density in Jy · pixel per beam).

| detector | wavelength [ $\mu\text{m}$ ] | pixel ["] | beam ["] | aperture ["] | corr. multiplier |
|----------|------------------------------|-----------|----------|--------------|------------------|
| blue     | 250                          | 6         | 18.1     | 168          | 1.02             |
| green    | 350                          | 10        | 25.2     | 150          | 1.05             |
| red      | 500                          | 14        | 36.6     | 154          | 0.94             |

Table 4.2: SPIRE detector properties, aperture sizes of the publication by [van Hoof et al., 2010] and correction multipliers.

| detector | wavelength [ $\mu\text{m}$ ] | $Y_{\text{Lit}}$ [Jy] | $Y$ [Jy] |
|----------|------------------------------|-----------------------|----------|
| blue     | 250                          | $13 \pm 6$            | 14.59    |
| green    | 350                          | $8 \pm 4$             | 5.78     |
| red      | 500                          | $2.2 \pm 1.5$         | 2.2      |

Table 4.3: Results from the flux density comparison

$Y$  ... measured and calibrated flux density

$Y_{\text{Lit}}$  ... flux density from the publication literature, [van Hoof et al., 2010].

In Table 4.3 the literature flux density  $Y_{\text{Lit}}$  and the measured flux density  $Y$  is comparable within the uncertainty for the three detectors. Further properties of the detectors and the correction can be obtained from Table 4.2.

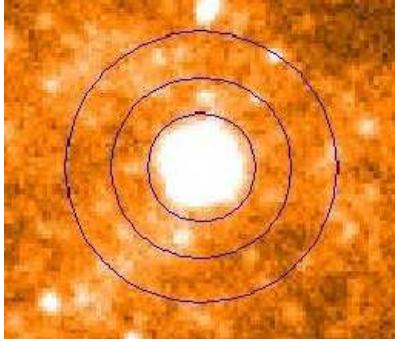
These excellent results indicate the working calibration and measurement of the SPIRE aperture photometry.

So there is nothing in the way to perform the SPIRE aperture photometry for the objects, U Ant and AQ And.

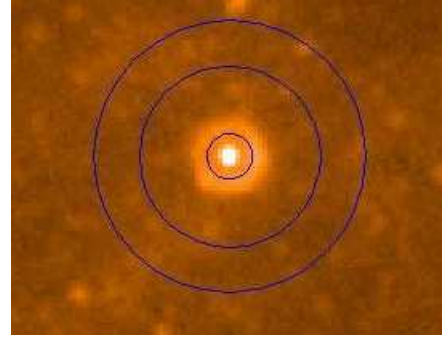
For PACS there is no correction necessary, because the measured flux density is already in the unit Jansky.

### Aperture photometry of U Ant

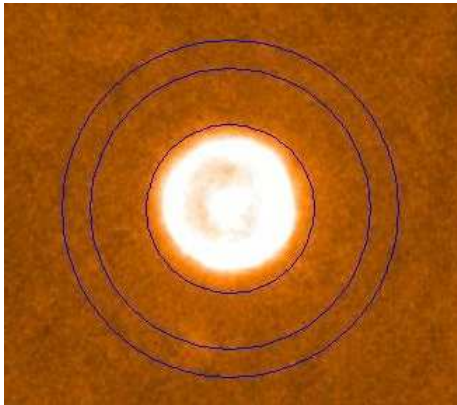
All SPIRE maps were reduced with the method described in chapter 2.2.2.2 (calibration version 8.1 and Scanamorphos 13). The PACS blue ( $70\ \mu\text{m}$ ) and red ( $160\ \mu\text{m}$ ) maps were created with the ScanAm version 13 and the built-in calTree.



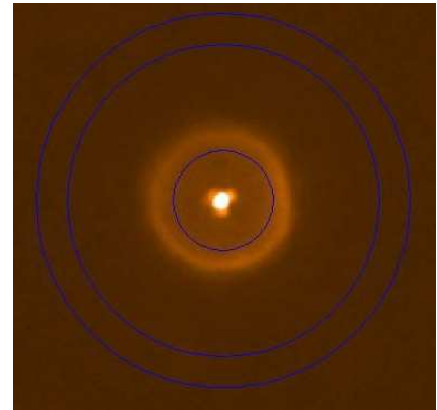
(a) entire object  $\sim 72$  arcsec, SPIRE ( $250\ \mu\text{m}$ ), 1 pixel = 6 arcsec.



(b) inner part  $\sim 30$  arcsec, SPIRE ( $250\ \mu\text{m}$ ).



(c) entire object  $\sim 60$  arcsec, PACS ( $70\ \mu\text{m}$ ), 1 pixel = 1 arcsec.



(d) inner part  $\sim 32$  arcsec, PACS ( $70\ \mu\text{m}$ ).

Figure 4.11: Aperture photometry of U Ant in SPIRE (Fig. 4.11(a) and Fig. 4.11(b)) and PACS (Fig. 4.11(c) and Fig. 4.11(d)). In Fig. 4.11(a) and Fig. 4.11(c) the entire object is measured, in Fig. 4.11(b) and Fig. 4.11(d) only the inner part without detached shell.

Fig. 4.11 illustrates the aperture photometry of U Ant in SPIRE ( $250\ \mu\text{m}$ ) and PACS ( $70\ \mu\text{m}$ ) as an example. The measurements for the other detectors were performed in a similar way.

In Fig. 4.11(a) the flux density from the entire object in  $250\ \mu\text{m}$  (SPIRE) is measured by the task `annularAperturePhotometry`. The aperture size is 72 arcsec (12 pixel) and the sky background was measured in a sector with as few as possible disturbance sources.

The total flux density of entire object in 250  $\mu\text{m}$  (SPIRE) is  $24.16 \pm 5$  Jy  $\cdot$  pixel per beam and the corrected flux density  $Y_{\text{object}}$  amounts to 2.39 Jy. The similar task was performed for the inner part ( $\approx 30''$ , 5 pixel) of U Ant (Fig. 4.11(b)).

In addition the total flux density of the inner part ( $\sim 30''$ , 5 pixel) results in a corrected flux density of 1.066 Jy in 250  $\mu\text{m}$  (SPIRE).

For the total detached shell flux density the subtraction of the entire object and the inner part was calculated and amounts to a detached shell total flux density of 1.32 Jy in 250  $\mu\text{m}$  (SPIRE).

In 70  $\mu\text{m}$  (PACS, (Fig. 4.11(c))) for an aperture of 60 arcsec the flux density from the entire object is 24.4 Jy (compare with  $27.1 \pm 4.1$  Jy, [Kerschbaum et al., 2010]), which is in the range of uncertainty of the publication (10 - 20 %).

The inner region (Fig. 4.11(d)) of U Ant ( $\sim 32''$ ) was measured to be 11.3 Jy. Furthermore the resulting detached shell flux density amounts to be 13.1 Jy.

A summary of the results from the aperture photometry is shown in Table 4.4.

The flux density measurement of the entire object of 6.198 Jy in PACS (160  $\mu\text{m}$ ) can be compared with [Kerschbaum et al., 2010] of  $7.4 \text{ Jy} \pm 1.2 \text{ Jy}$ , which is in agreement within the uncertainty.

| wavelength [ $\mu\text{m}$ ] | pixel ["] | aperture ["] | inner part ["] | $Y_{\text{object}}$ [Jy] | $Y_{\text{shell}}$ [Jy] |
|------------------------------|-----------|--------------|----------------|--------------------------|-------------------------|
| SPIRE: 250                   | 6         | 72           | 30             | 2.39                     | 1.32                    |
| 350                          | 10        | 70           | 30             | 0.8253                   | 0.478                   |
| 500                          | 14        | 70           | -              | 0.0855                   | -                       |
| PACS: 70                     | 1         | 70           | 32             | 24.4                     | 13.1                    |
| 160                          | 2         | 60           | 32             | 6.198                    | 3.729                   |
| IRAS: 12                     | $\sim 30$ | -            | -              | 167.53                   | -                       |
| 25                           | $\sim 30$ | -            | -              | 44.81                    | -                       |
| 60                           | $\sim 30$ | -            | -              | 27.11                    | -                       |
| 100                          | $\sim 30$ | -            | -              | 21.14                    | -                       |

Table 4.4: Summary of the aperture photometry of the SPIRE, PACS and IRAS [Izumiura et al., 1997] observations. The aperture was laid over the entire object and the inner part was measured without the detached shell.

$Y_{\text{object}}$  ... calibrated and corrected flux density in Janskys

$Y_{\text{shell}}$  ... flux density of the detached shell in Janskys.



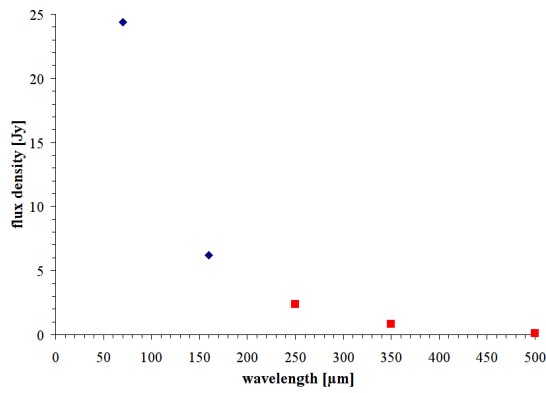
In Fig. 4.12 the data results from the photometry are plotted as flux density versus wavelength, which represent the spectral energy distribution (SED) at the appropriate wavelengths.

The flux densities of the detached shell are shown in Fig. 4.12(b).

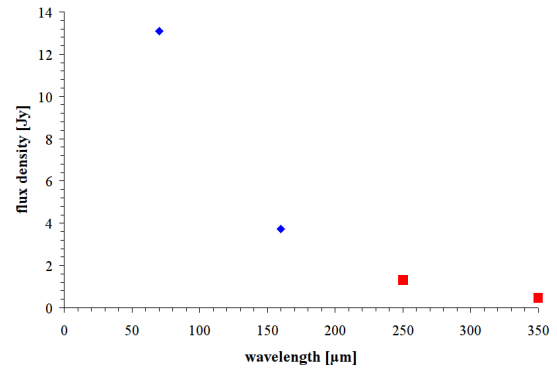
Additional flux densities (Fig. 4.12(c)) are obtained from the IRAS mission [Izumiura et al., 1997] to extend the SED.

These data results can be compared with the black body radiation described with the Planck law to get the best fitting and thus a temperature estimation.

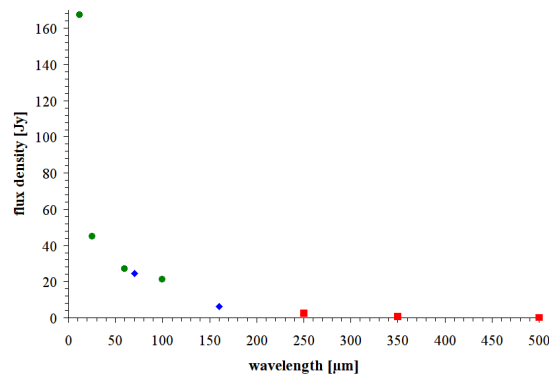
Further assumption of the dusty species and its optical properties must be estimated. In the next chapter this temperature estimation is described.



(a) Flux density vs wavelength of the entire object; PACS (blue diamond) + SPIRE (red square).



(b) Flux density vs wavelength of the detached shell; PACS (blue diamond) + SPIRE (red square).



(c) flux density vs wavelength of the entire object; PACS (blue diamond) + SPIRE (red square) + IRAS (green circle).

Figure 4.12: U Ant:

Fig. 4.12(a): SED of the entire object from the PACS and SPIRE photometry.

Fig. 4.12(b): SED of the detached shell from the PACS and SPIRE photometry.

Fig. 4.12(c): SED of the entire object from the PACS, SPIRE and IRAS photometry [Izumiura et al., 1997].

### 4.1.2.1 Black body estimation

In this chapter the black body radiation is estimated with two different approaches for the temperature determination.

First the Planck fitting with absorption coefficients from amorphous carbon (AmC) is derived with flux density ratios.

The second method works similarly like the first method, but in addition it uses the filter response from PACS and therefore can be only applied to flux densities of PACS.

#### Planck fitting with amorphous carbon

The object and the shell is assumed to radiate as black body and dominated by dust emission, so this is only a rough estimate of the temperature. A further assumption is that the dust contains mainly amorphous carbon with all its optical properties (absorption coefficient).

The dust emissivity  $F_\nu$  in equation 4.3 (e.g. the measured flux density in Janskys) is calculated by:

$$F_\nu = Q_\nu \cdot B_\nu(T) \quad (4.3)$$

Q ... Q-factor: absorption coefficient at a specified wavelength for amorphous carbon (ratio of the absorption cross section to the geometrical cross section)

$B_\nu(T)$  ... Planck function, dependent on the frequency or the wavelength and the temperature. [ $\text{W} \cdot \text{m}^{-2} \cdot \text{Hz}^{-1}$ ]

Q-factors for the appropriate wavelength are obtained from [Draine, 1981], which are derived from laboratory measurements on carbon smoke. Starting at 200  $\mu\text{m}$  the sampling points of the Q-factor have large gaps, that's why the accuracy is decreasing and using (linear interpolation) of Q-factors until 250  $\mu\text{m}$  is recommended.

With the help of equation 4.3 the temperature estimation of dust can be performed through the ratio of this formula with two different wavelengths.

Example: Comparison of PACS wavelengths:

$$\frac{F_{\nu,70}}{F_{\nu,160}} = \frac{Q_{\nu,70} \cdot B_{\nu,70}(T)}{Q_{\nu,160} \cdot B_{\nu,160}(T)} \quad (4.4)$$

The ratio of  $F_{\nu,70}$  and  $F_{\nu,160}$  in equation 4.4 is known through the measured flux density values, and the Q-factors are derived from the interpolation (Table 4.5).

As result the ratio of  $B_{\nu,70}(T)$  and  $B_{\nu,160}(T)$  is constant value.

For the next step the calculation of the appropriate  $B_{\nu,70}(T)$  and  $B_{\nu,160}(T)$  with an initial temperature is done. The temperature is altered until the constant ratio is reached and so the temperature estimation of the dust is performed.

| wavelength [ $\mu\text{m}$ ] | Q-factor |
|------------------------------|----------|
| 70                           | 493.8    |
| 160                          | 255      |
| 250                          | 132.2    |

Table 4.5: Interpolated Q-factors (absorption coefficients) for PACS and SPIRE by [Draine, 1981].

| wavelength ratio | $T_{\text{object}}$ [K] | $T_{\text{shell}}$ [K] |
|------------------|-------------------------|------------------------|
| 70/160           | 78.3                    | 72                     |
| 160/250          | 35.5                    | 40.5                   |

Table 4.6: Results for the temperature of the entire object and the detached shell from the Planck fitting with AmC.

The results of the temperature estimation are summarized in Table 4.6.

### Planck fitting with amorphous carbon and PACS filter response

The method simulates the black body radiation convolved with the PACS filter response to predict the fluxes observed with PACS and calculates the appropriate temperature by giving at least two flux values of the PACS photometry. Like in the first method the Planck curve is fitted until the appropriate flux density ratio is reached.

The python scripts for the simulation were written by Stefano Pezzuto [Pezzuto, 2012].

As input the routine uses the response function of the PACS filters (Fig. 4.13), which is directly obtained from the calibration tree, and the flux densities from 70 $\mu\text{m}$  and 160 $\mu\text{m}$  PACS bands.

These response curves were derived from cold and warm measurements of the filter transmission, dichroic transmission and reflections.

In addition, the absorption coefficients of amorphous carbon at 70  $\mu\text{m}$  and 160  $\mu\text{m}$  were interpolated from the data tables (Table 4.5) of [Draine, 1981].

The derived temperature can now be checked against the method without the PACS filter response and the publication by [Kerschbaum et al., 2010] in Table 4.7.

For a black body assumption with PACS filters the detached shell has a temperature of 73 K and over the entire object a temperature of 81 K.

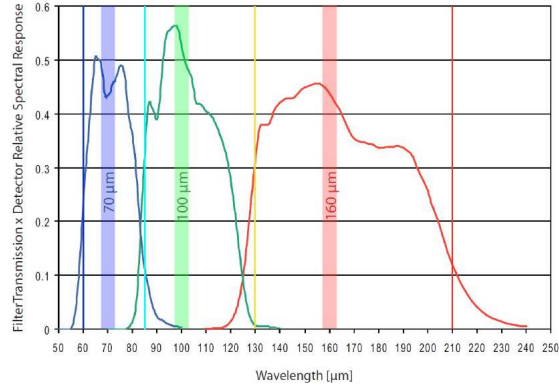


Figure 4.13: PACS filter response for the three bands (70  $\mu\text{m}$ , 100  $\mu\text{m}$ , 160  $\mu\text{m}$ ), [ESA, 2012b].

In [Kerschbaum et al., 2010] the temperature estimation is not derived through Planck fitting, but through hydrodynamic modeling in DUSTY and radial profile fitting, thus there is no flux density ratio and no temperature of the entire object.

| temperature estimation method    | wavelength ratio | $T_{\text{object}}$ [K] | $T_{\text{shell}}$ [K] |
|----------------------------------|------------------|-------------------------|------------------------|
| Planck fitting with AmC          | 70/160           | 78.3                    | 72                     |
|                                  | 160/250          | 35.5                    | 40.5                   |
| Planck fitting with AmC and PACS | 70/160           | 81                      | 73                     |
| DUSTY, [Kerschbaum et al., 2010] | -                | -                       | 39.3                   |

Table 4.7: Results for the temperature of the entire object and the detached shell from the Planck fitting with AmC, the Planck fitting with the PACS filter response and [Kerschbaum et al., 2010].

### 4.1.3 Model fitting with DUSTY

In this chapter the radial profile from the observation will be compared to the synthetic model, which is modeled in DUSTY. DUSTY was developed by Zeljko Ivezic, Maia Nenkova and Moshe Elitzur [Ivezic and Elitzur, 1997] at the university of Kentucky, Lexington, USA.

With DUSTY it is possible to solve the radiation transport problem for a star or a galactic nucleus in dusty environments. Furthermore the self-consistent solution contains dust scattering, emission and absorption without any approximations. Optical properties and different dust species can be specified within DUSTY and additional grain types are addable.

For this master thesis it is very important that the radiatively dust-driven wind around AGB-stars is full-dynamically calculated. DUSTY supports many other scenarios of simulations and adjustable parameters, but this is out of the scope of this master thesis. For a detailed description of DUSTY the user manual at the website <http://www.pa.uky.edu/~moshe/dusty/>, [Ivezic and Elitzur, 2012] is recommended.

For the model fitting and the comparison with the observed radial profile the PACS wavelength  $70 \mu\text{m}$  was chosen, because the detached shell was smooth and bright here. In addition the PSF in  $70 \mu\text{m}$  (obtained from the object AFGL 190, point source) of PACS-Herschel is available, which was created by Roland Ottensamer. This PSF will be convolved with the derived DUSTY model to fit the observed radial profile.

#### Necessary input parameters

The input parameters must be set in an appropriate text file.

First the effective temperature of the star must be given and is described by a Planck function as black body.

The next parameters specify the dust properties, at which the grain size (default values: minimal size:  $5 \cdot 10^{-3} \mu\text{m}$  and maximal size:  $2.5 \cdot 10^{-1} \mu\text{m}$ ) and dusty species can be selected. DUSTY provides built-in dust grain types and further species are addable via text files, which contain the absorption and scattering coefficients.

The fractions between the different types of dust is also adjustable, but grain mixtures are simulated as single-type dust grain with an appropriate average.

An important parameter is the dust temperature on the inner boundary of the shell (shell inner radius  $r_1$ ), which is the dominating factor for the positioning of the detached shell and is discussed in the paragraph “Effects on the shell radius by varying the input parameters”.

Another required input describes the density distribution, which is scaled with the shell inner radius. For AGB-stars the “density type = 3” was chosen to model the envelope

expansion, which is driven by the radiation pressure on dust grains and so the hydrodynamical equations must be solved by DUSTY (dust shift and star's gravity included). The typical wind has a expansion velocity larger than  $5 \text{ km s}^{-1}$ .

In addition to the density type, the shell thickness  $Y$  relative to the shell inner radius  $r_1$  is required ( $Y=r_{\text{out}}/r_1$ ,  $r_{\text{out}}$  ... outer boundary of the shell).

For the optical depth grid the reference wavelength of the dust (default:  $0.55 \mu\text{m}$ ), the minimum ( $\tau_{\text{min}}$ ) and maximum ( $\tau_{\text{max}}$ ) of optical depth ( $\tau$ ), and the number of models must be entered. The number of models fixes the sampling points between  $\tau_{\text{min}}$  and  $\tau_{\text{max}}$ . The more models, the more different  $\tau$  grid points can be tested and so more possible simulations. Per each  $\tau$  value a radial profile and other outputs can be derived. When only one model is chosen, the  $\tau_{\text{min}}$  value is used.

As last part the output files (for each  $\tau$  a separate file) as well as the intensity per square arcsec for a specified wavelength (here:  $70 \mu\text{m}$ ), which is used for the radial profile fitting, can be set.

### Output files

There is one global \*.out file, which summarizes the input parameters and describes for each  $\tau$  simulation the scaling factors (inner shell radius in cm at the default luminosity  $L = 10^4 L_{\odot}$ ; the radius scales in proportion of  $L^{1/2}$ ), the mass loss and many other outputs.

The intensity for the radial profile can be extracted from \*.i001 files (first  $\tau$  simulation), in which the first column shows the impact parameter (“the radius”), the second  $\tau$  as function of the impact parameter and the last the desired intensity per square arcsec.

### Rescaling of the impact parameter to arcsec for the comparison of the radial profile

It is necessary to rescale the impact parameter with the inner shell radius ( $r_1$ ) from the \*.out file for each  $\tau$  simulation because the impact parameter is normalised with the inner shell radius at a default luminosity  $L$  of  $10^4 L_{\odot}$ .

First the inner shell radius ( $r_1$ ) is multiplied with the square root of the ratio of luminosity of the star and the default luminosity ( $L = 10^4 L_{\odot}$ ) to derive a new inner shell radius scaling  $r_{1,\text{scale}}$ .

This new radius  $r_{1,\text{scale}}$  together with the distance is used to rescale the impact parameter to arcsec.

Each impact parameter value must be multiplied with

$$\arctan\left(\frac{r_{1,\text{scale}}}{\text{distance}}\right) \quad [\text{arcsec}] \quad (4.5)$$

for the comparison with the observed radial profile. ( $r_{1,\text{scale}}$  and distance in unit metre!)

### Effects on the shell radius by varying the input parameters

A base model was estimated to fix a detached shell at 42 arcsec with the DUSTY input parameters in Table 4.8. From this base model the parameters can be changed to test the parameter dependencies. For the other parameters, which are not given in Table 4.8, the default values from DUSTY were used.

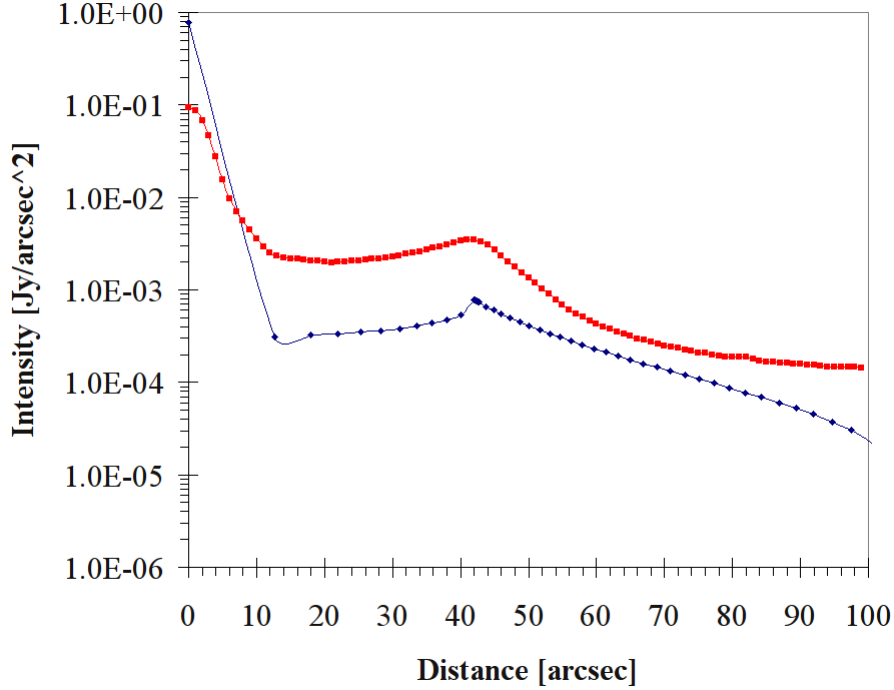


Figure 4.14: Radial profile of U Ant; red: PACS (70  $\mu\text{m}$ ) observation, blue: DUSTY base model.

|                        |                            |                       |               |
|------------------------|----------------------------|-----------------------|---------------|
| $T_{\text{eff}}$ [K]   | luminosity [ $L_{\odot}$ ] | $\Delta R=Y$          | distance [pc] |
| 2810                   | 5800                       | 2.5                   | 320           |
| dust species           | optical depth $\tau$       | $T_{\text{dust}}$ [K] |               |
| AmC-Hn, [Hanner, 1988] | 0.001                      | 73.1                  |               |

Table 4.8: DUSTY input parameters for the U Ant base model. effective temperature of the star in Kelvin as BB, luminosity of the star, shell thickness ( $Y=r_{\text{out}}/r_1$ ) relative to the inner shell radius  $r_1$ , distance in pc, dust species with 100 % AmC by Hanner [Hanner, 1988], optical depth of the dust shell, temperature at the inner boundary of the shell in Kelvin.

In Fig. 4.14 the radial profile of the observation (red) is compared with the derived base model (blue). It is recognisable that the detached shell in DUSTY is more peaked than the rounded detached shell in the observation. The reason for this discrepancy is the



Herschel optic, which has a special PSF (Fig. 4.2). Furthermore there are not many sampling points near the star in DUSTY and in addition the observation shows a weaker star profile, because an attached shell is necessary to account for the actual mass-loss rate, which can be represented by an attached shell around the star [Kerschbaum et al., 2010]. A further problem is the sky background after the detached shell, which cannot be fitted with DUSTY, but this is negligible.

In the next passages the dependency of the shell radius on different input parameters is outlined.

### Dust temperature on the inner boundary:

The dominating input parameter, which varies the shell radius significantly, is the dust temperature on the inner boundary. Through increasing the temperature the shell can be nearer at the star and vice versa.

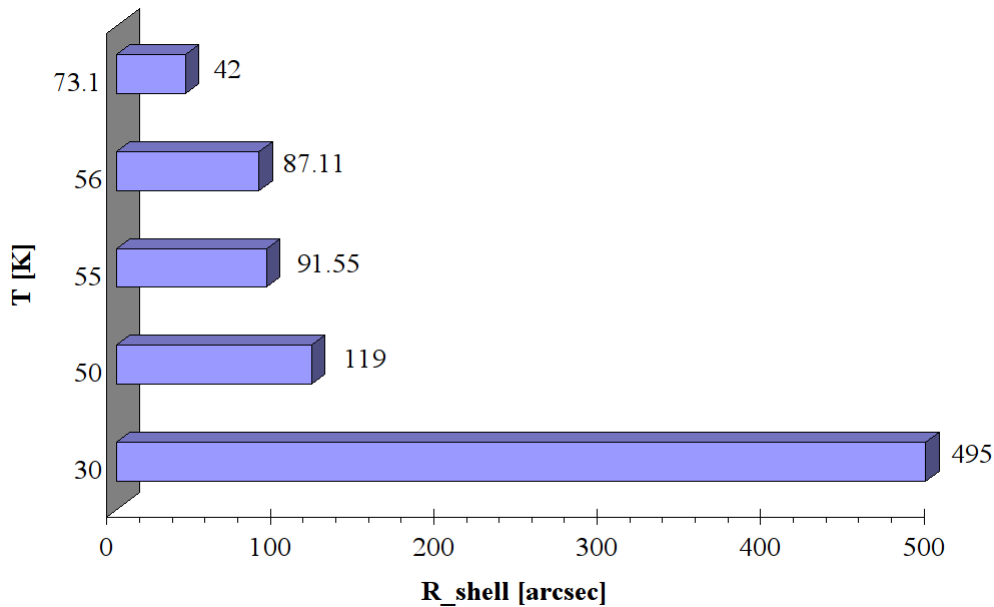


Figure 4.15: Inner shell radius as a function of the dust temperature on the inner boundary; beginning at 30 K until shell radius (42 arcsec) is fitted at 73.1 K

In Fig. 4.15 at 30 K the position of the shell radius at 42 arcsec enlarges to  $\sim 495$  arcsec. Changing to 50 K leads to a 119 arcsec shell radius. Variations in a 1-K-range from 55 K (91.55 arcsec) to 56 K (87.11 arcsec) result in 4.44 arcsec difference. The inner shell radius is highly dependent (inverse proportional) on the dust temperature on the inner boundary and that's why a shell with lower dust temperature is farther away from the star because the photon flux is weaker and vice versa.

**Distance:**

There are two verified distances known for U Ant, 260 pc (Hipparchos mission) and 320 pc [Bergeat and Chevallier, 2005].

With 320 pc the detached shell's radius is 42.05 arcsec. Using the distance of 260 pc the radius changes to 51.75 arcsec, which is  $\sim 23\%$  larger ( $\sim 10$  arcsec). The object is then closer to our solar system and thus it appears larger. To correct this shell radius difference, a dust temperature increase by  $\sim 2$  K is necessary.

**Luminosity:**

Changing the luminosity from  $5800 L_{\odot}$  to  $8000 L_{\odot}$  leads to shell radius of 49.4 arcsec, which is 7 arcsec bigger. To compensate this difference, an increase of the dust shell temperature by  $\sim 1.6$  K is possible.

**Shell thickness:**

The shell position remains unchanged, but the shell enlarges due to the larger thickness and the flux values distribute over a larger area and thus the flux from the shell is weaker.

In Fig. 4.16 radial profiles with different shell thickness's 1.3, 2.5 and 5 are shown. The distribution of the star flux at the shell with the largest thickness (black line) is broadened over a large area to an outer radius of 150 arcsec and thus the weakest. Furthermore the flux density is decreasing in a larger area with a lower gradient than the thinnest shell with thickness of 1.3.

**Chemical composition and the optical depth  $\tau$ :**

In Fig. 4.17 the interstellar silicate grains Sil-DL [Draine and Lee, 1984] and warm (oxygen-deficient) and cold (oxygen-rich) cosmic silicates Sil-Ow and Sil-Oc [Ossenkopf et al., 1992] are stable minerals with high bonding energy and thus are able to resist against the radiation better than amorphous carbon. So the shells can be placed closer to the star at the same temperature (73.1 K) because the silicate grains can absorb the radiation without destruction.

Graphite is a stable form of carbon (allotrope of carbon) in hexagonal structure, which can absorb high amounts of radiation similar to the silicates. Thus grf-DL [Draine and Lee, 1984] causes a shell at  $\sim 16 - 20$  arcsec.

Amorphous carbon dust AmC-Zb1-Zb2 (cosmic carbon analogue grains, [Zubko et al., 1996]) and ice-coated AmC grains [Preibisch et al., 1993], and AmC-Hn (Infrared observations of comets Halley and Wilson, [Hanner, 1988]) have no crystalline structures and a low packing density and thus a low bonding energy. So the shells must

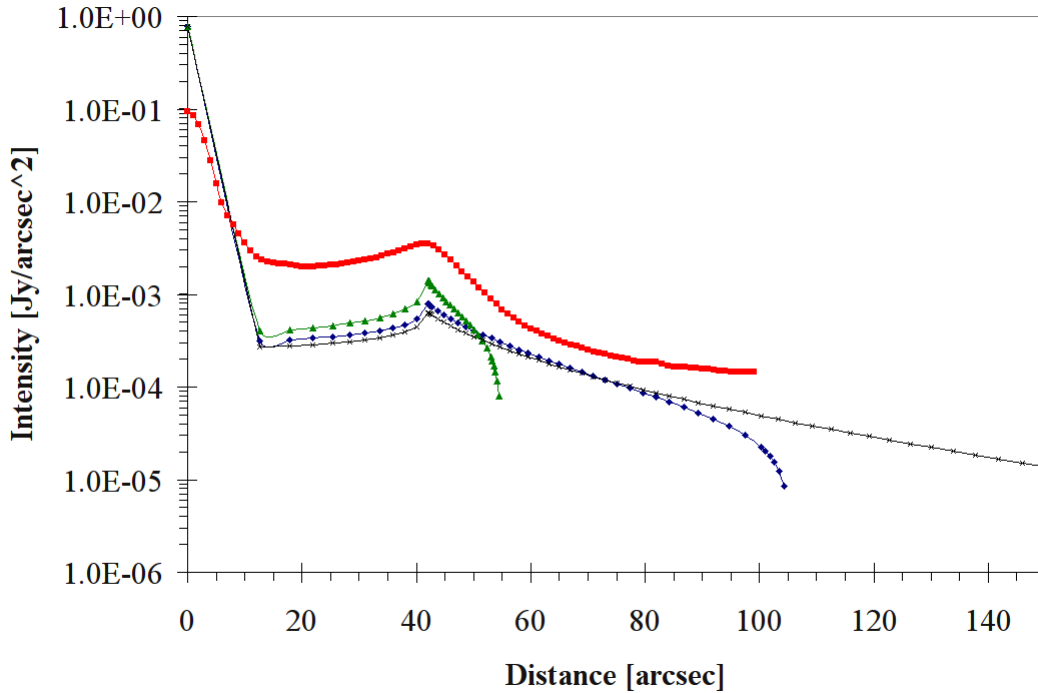


Figure 4.16: Radial profiles of U Ant; red: PACS ( $70 \mu\text{m}$ ) observation, DUSTY base model with different shell thickness: blue:  $\Delta R = 2.5$ , green:  $\Delta R = 1.3$ , black:  $\Delta R = 5$

be more distant from the star to stay on the whole.

AmC-Zb3 was produced in a  $\text{H}_2$  atmosphere under 10 mbar and thus is more stabilized. That's why it can block the radiation from the star better in a similar way as graphite.

Silicon-Carbide SiC-Pg [Pegourie, 1988] consists of silicon and carbon in hexagonal crystal structure, which is due to the weak resistance properties of carbon susceptible and decomposes. It reaches shell radii similar to AmC-Hn.

In the optically thick case ( $\tau \gg 1$ ;  $\tau = 5$ ) more radiation is absorbed and scattered in the shell than in an optically thin shell ( $\tau \ll 1$ ;  $\tau = 0.001$ ). The shell is getting warmer and so the dust can easier be dissociated, and thus the shell must be placed more outwards to survive the dissociation.

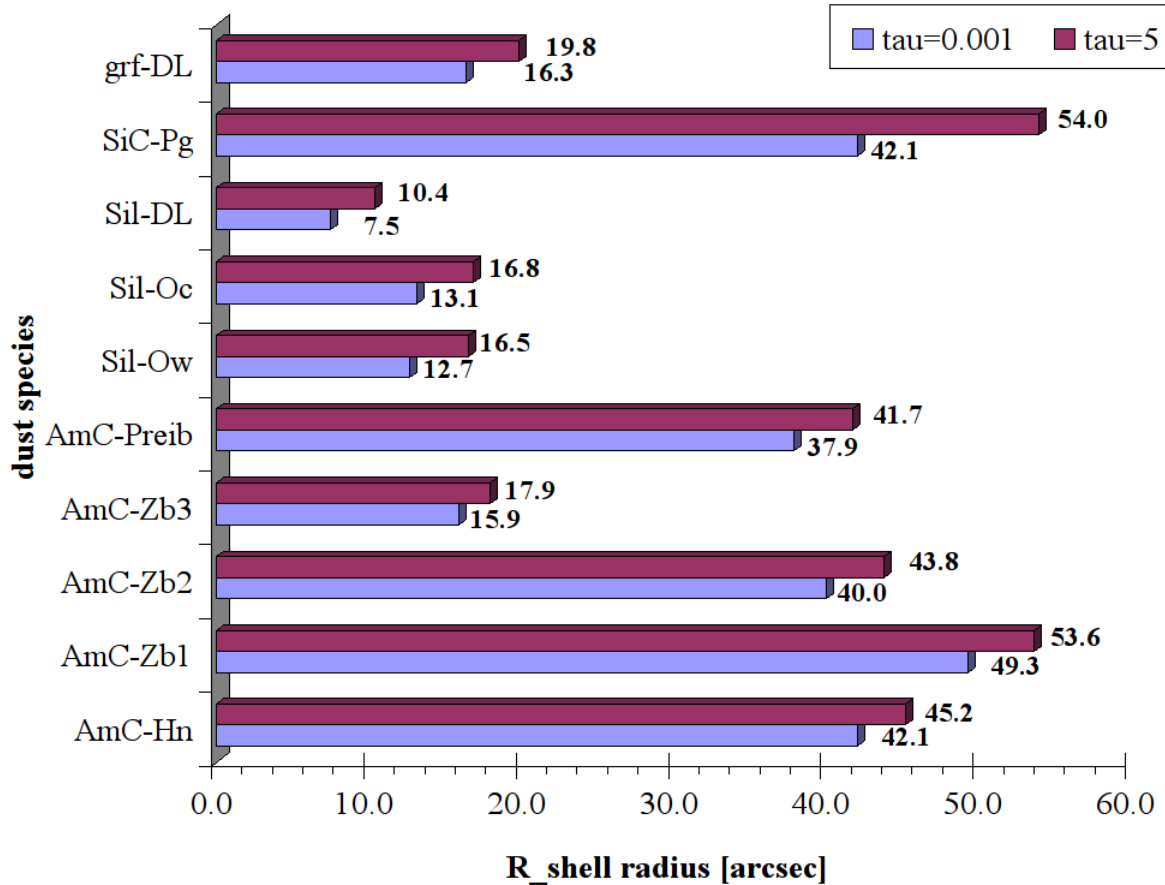


Figure 4.17: Different dust species in the optically thin ( $\tau=0.001$ ) and thick ( $\tau=5$ ) case at a constant temperature of 73.1 K.

grf-DL graphite [Draine and Lee, 1984], SiC-Pg silicon-carbide [Pegourie, 1988], Sil-DL astronomical silicate [Draine and Lee, 1984], Sil-Ow and Sil-Oc warm (O-deficient) and cold (O-rich) silicates [Ossenkopf et al., 1992], AmC-Preib ice-coated amorphous carbon grains [Preibisch et al., 1993], AmC-Zb1-3 three different cosmic amorphous carbon analogue grains [Zubko et al., 1996], AmC-Hn amorphous carbon grains from comets Halley and Wilson [Hanner, 1988].

### Final DUSTY model for U Ant

In Table 4.9 the parameters of the final DUSTY model are shown. Furthermore as comparison the DUSTY model by [Kerschbaum et al., 2010] was added. A comparison of the temperature estimation of the different methods is performed in Table 4.10.

To compare the models a luminosity of  $8000 L_{\odot}$  was assumed. The differences in distance (2 K higher  $T_{\text{dust}}$ ) and dust species (1 K lower  $T_{\text{dust}}$ ) would result in a by 1 K higher  $T_{\text{dust}}$  (2 K minus 1 K) for the final model, which is negligible. Furthermore the discrepancy in the shell thickness and the optical depth only vary the shell's shape and flux density in a nonsignificant way.

An other important disagreement with [Kerschbaum et al., 2010] concerns the dust temperature  $T_{\text{dust}}$  on the inner boundary of the shell. The offset of 38.4 K cannot be explained by the different distance or dust species, because this is only 1 K difference. In [Kerschbaum et al., 2010] additional assumptions to the BB of the radiation source are considered by [Aringer et al., 2009], who provide synthetic models for atmospheres of carbon stars with different opacities, scattering coefficients and abundance assumptions of molecules due to the C/O-ratio. This supplement can result in a lower flux density due to the absorption by molecules (Gustaffsson and Höfner, 2004) and thus in a lower temperature in the detached dust shell.

Comparing the dust temperature of the detached shell with the methods of the Planck fitting leads to good agreement of the temperatures 72 and 73 K at PACS wavelengths in Table 4.10. The 160 to 250  $\mu\text{m}$  (PACS and SPIRE) ratio estimation of 40.5 K is in agreement with [Kerschbaum et al., 2010] of 39.3 K, but the PACS and SPIRE estimation can be considered as rough estimation with high error, because in SPIRE it is very difficult to measure the detached shell due to the low resolution, and weak and noisy signal. A further error source concerns the absorption coefficients by [Draine, 1981], which accuracy decreases for the 250  $\mu\text{m}$  channel due to gaps in the sampling points and linear interpolation. The temperature value of 40.5 K from the 160/250 ratio can be assumed as lower temperature limit in the best case. In general the temperature of the dust shell can be set in a range of 40.5 – 77.7 K.

Moreover an attached shell with an inner temperature of 1000 K was added in [Kerschbaum et al., 2010] to fit the radial profile and to represent the actual mass-loss rate. This additional inner shell also changes the profile of the radiation source and thus can result in a different flux density and dust shell temperature. The SED of these shells were added together, which is due to [Schöier et al., 2005] possible when considered as optically thin shells, but this consideration can also be assumed as a possible error source.

In the final model the mass-loss rate of the detached shell of  $14 \cdot 10^{-7} M_{\odot} \text{ year}^{-1}$  with a grain density of  $1.85 \text{ g cm}^{-3}$  and a gas-to-dust-ratio of 200 is in order of magnitude similar to a mass-loss rate of  $7 \cdot 10^{-7} M_{\odot} \text{ year}^{-1}$  by [Kerschbaum et al., 2010].

The doubling of the mass-loss rate is due to different model assumptions, which were explained in the upper passages, and due to the uncertainty ( $\sim 30\%$ ) in DUSTY modeling.

| Final DUSTY model               |                            |                       |               |  |
|---------------------------------|----------------------------|-----------------------|---------------|--|
| $T_{\text{eff}}$ [K]            | luminosity [ $L_{\odot}$ ] | $\Delta R=Y$          | distance [pc] |  |
| 2810                            | 8000                       | 1.2                   | 320           |  |
| dust species                    | optical depth $\tau$       | $T_{\text{dust}}$ [K] |               |  |
| AmC-Hn, [Hanner, 1988]          | 0.0031                     | 77.7                  |               |  |
| [Kerschbaum et al., 2010] model |                            |                       |               |  |
| $T_{\text{eff}}$ [K]            | luminosity [ $L_{\odot}$ ] | $\Delta R=Y$          | distance [pc] |  |
| 2800                            | 8000                       | 1.3                   | 260           |  |
| dust species                    | optical depth $\tau$       | $T_{\text{dust}}$ [K] |               |  |
| AmC, [Preibisch et al., 1993]   | 0.002                      | 39.3                  |               |  |

Table 4.9: DUSTY final model parameters for U Ant and [Kerschbaum et al., 2010] model; effective temperature of the star, luminosity of the star, shell thickness ( $Y=r_{\text{out}}/r_1$ ) relative to the inner shell radius  $r_1$ , distance in pc, dust species, optical depth of the dust shell and temperature at the inner boundary of the shell.

| temperature estimation method    | wavelength | $T_{\text{shell}}$ [K] |
|----------------------------------|------------|------------------------|
| Planck fitting with AmC          | 70/160     | 72                     |
|                                  | 160/250    | 40.5                   |
| Planck fitting with AmC and PACS | 70/160     | 73                     |
| DUSTY, [Kerschbaum et al., 2010] | 70         | 39.3                   |
| DUSTY, thesis' results           | 70         | 77.7                   |

Table 4.10: Results for the temperature of the detached dust shell from the Planck fitting with AmC, the Planck fitting with the PACS filter response, [Kerschbaum et al., 2010] and the results of this master thesis.

In Fig. 4.18 the observed radial profile in PACS ( $70 \mu\text{m}$ ) and the final DUSTY model is plotted. The detached shell (peak) of the model is located at 41.7 arcsec and not at 42 arcsec. This offset has its purpose for the preparation of the convolution with the Herschel optics, which shifts and rounds up the detached shell with this small difference in radial distance.

Fig. 4.19 illustrates the fitted DUSTY model with convolution of the Herschel-PSF. The convolution causes a shift of the detached shell by 0.3 arcsec from 41.7 to 42 arcsec and weakens the star flux. Furthermore the peak of the detached shell is rounded up to fit the observation in Fig. 4.19(a) and Fig. 4.19(b). In non-logarithmic scale (Fig. 4.19(b)) and logarithmic scale (Fig. 4.19(a)) the DUSTY is nearly completely fitted except in the

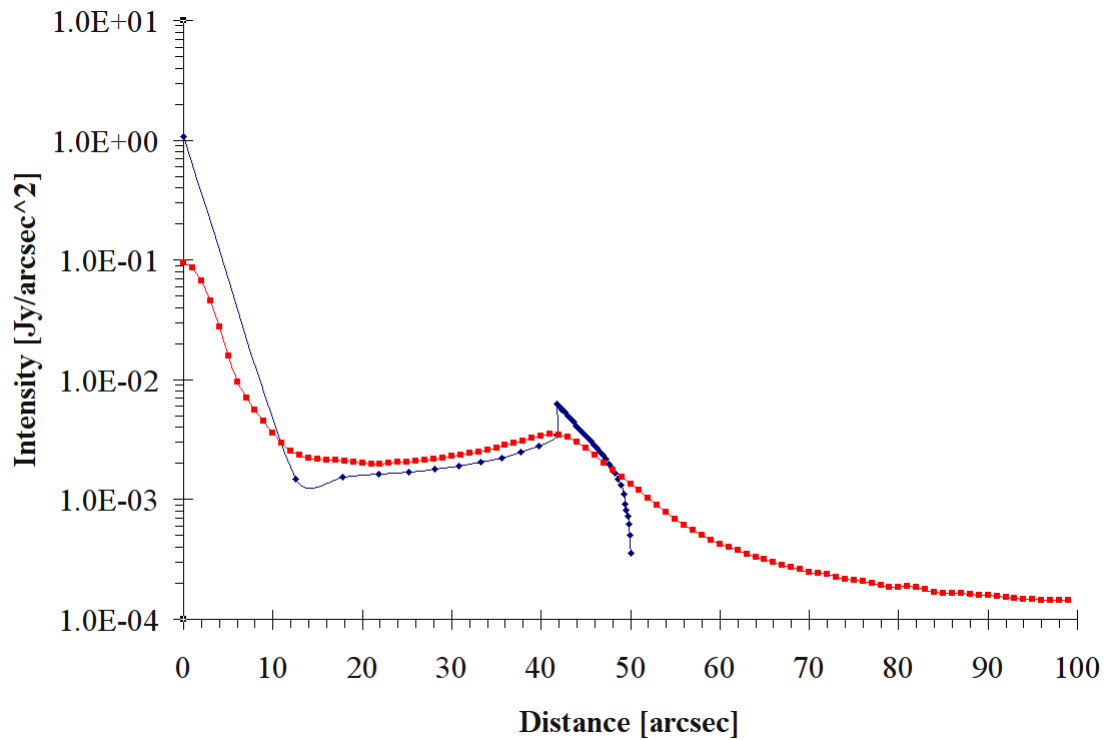
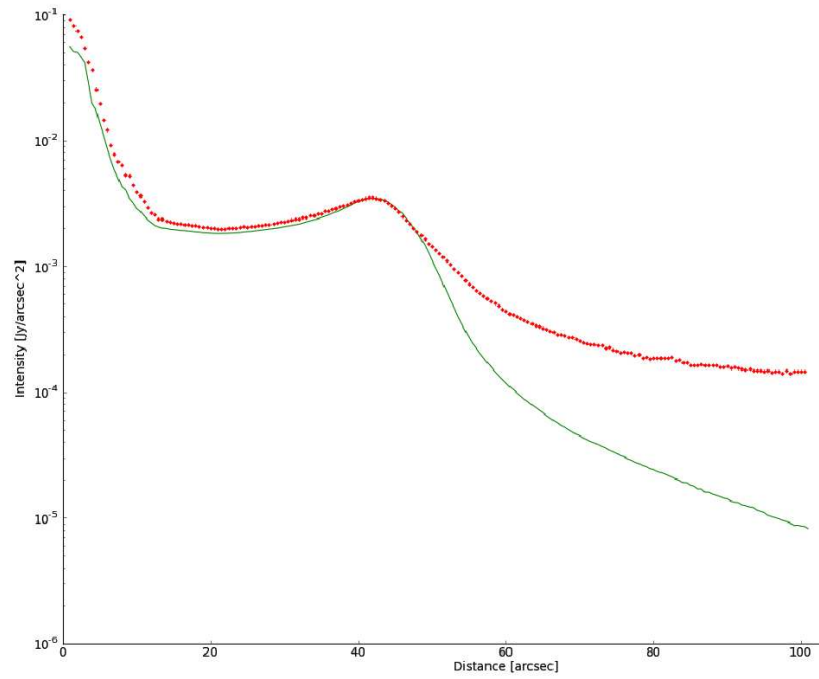
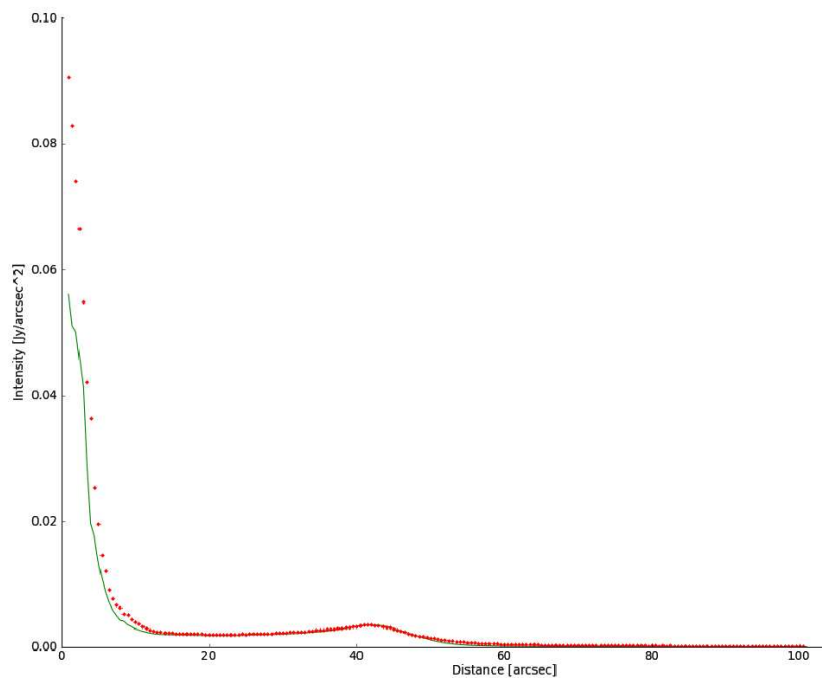


Figure 4.18: Final DUSTY model; red: observed radial profile in  $70 \mu\text{m}$ , blue: fitted DUSTY model without convolution with the Herschel optics.

inner star part. The star part of DUSTY is by  $\sim 0.03 \text{ Jy per arcsec}^2$  weaker (33 %) than the observation. The reason for the difference is the missing attached shell, which can raise the inner part. After the detached shell starting at  $\sim 50 \text{ arcsec}$  the sky background (Fig. 4.19(a)) cannot be simulated by DUSTY and results in an offset by  $\sim 0.1 \text{ Jy per arcsec}^2$ , which is negligible.



(a) red: observed radial profile, green: fitted DUSTY model with convolution with the Herschel PSF in logarithmic scale.



(b) red: observed radial profile, green: fitted DUSTY model with convolution with the Herschel PSF.

Figure 4.19: Final DUSTY model for U Ant as logarithmic (Fig. 4.19(a)) and linear (Fig. 4.19(b)) plot.



#### 4.1.4 Conclusion and interpretation

The observation of U Ant with the Herschel instruments PACS and SPIRE confirms the detached shell. In PACS the detached shell is located at 42 arcsec, which is published in [Kerschbaum et al., 2010] and also detected by [Maercker et al., 2010] in CO-lines and scattered light and with AKARI by [Arimatsu et al., 2011].

In this thesis further observations in SPIRE reveal shells at 36 and 40 arcsec, which could indicate superpositions of arc-like structures like in [Maercker et al., 2010] in the inner part with the detached shell, but this is only an assumption. Only the deconvolution of the inner part of the star could reveal further details.

The extended emission at 3 arcmin by [Izumiura et al., 1997] was partly discovered also in SPIRE in all detectors in addition to the PACS observations in [Kerschbaum et al., 2010].

Due to the different reduction method in this thesis the extended emission was not detected in PACS, but a smooth radial profile could be created to model the detached shell in DUSTY.

The derived radial profile from the observation in PACS was successfully modeled in DUSTY. In addition the shell's shape was reproduced with the help of the convolution of the Herschel PSF with the PACS map. Furthermore the offset of the inner stellar part to the model is caused due to a missing attached shell, which represents the recent mass-loss. A further offset concerns the sky background, which cannot be simulated with DUSTY and is negligible.

The dust shell temperature of 77.7 K of the model is in good agreement with the estimated Planck temperatures (PACS flux densities) of 72 K and 73 K when assuming amorphous carbon. The deviation of the dust temperature in [Kerschbaum et al., 2010] to a lower temperature of 39.3 K can be explained through different modeling of the stellar part [Aringer et al., 2009] and using of an attached shell. A dust temperature of 40.5K was also calculated through PACS and SPIRE flux densities, but this temperature can only be considered as lower limit, because the aperture photometry of the detached shell in SPIRE together with the absorption coefficients of the dust are fraught with uncertainty due to lower resolution and interpolated values. An overall dust temperature range of 40.5 – 77.7 K is estimated for the detached shell.

The mass-loss rate of the detached dust shell results in  $14 \cdot 10^{-7} M_{\odot} \text{ year}^{-1}$  and agrees with the mass-loss rate of  $7 \cdot 10^{-7} M_{\odot} \text{ year}^{-1}$  in [Kerschbaum et al., 2010] within the uncertainties of the model assumptions and of DUSTY in general.

## 4.2 AQ And

### 4.2.1 PACS and SPIRE observations

The PACS final maps were created by ScanAm version 13 and the SPIRE maps were reduced with HIPE (version 8.0.3282, calTree 8.1) and ScanAm (version 13) in the highest possible resolution in the same way as the science object U Ant.

The radial profiles of PACS and SPIRE are derived with the same procedure like for the object U Ant.

The task sourceFitting derived the accurate centre coordinates and the end product is the plot of the intensity per square arcsec versus the distance in arcsec.

In the PACS map (Fig. 4.20(a) and Fig. 4.20(b)) the detached shell at 52 arcsec radius has overall spheric geometry and the thickness of shell is almost constant.

In addition in the PACS blue radial profile (Fig. 4.20(b)) the detached shell at 52 arcsec is clearly visible. Furthermore the inset in Fig. 4.20(b) is an enlargement between 16 and 42 arcsec, which reveals a few intensity peaks. These intensity peaks suggest variations in the mass-loss rate as brief events and could be assumed as further thin shells or arc-like structures.

In the red channel (Fig. 4.20(d)) the detection of the detached shell is located at  $\sim 51$  arcsec and is comparable to the blue one. The red PACS map Fig. 4.20(c) shows a more clumpy and jagged structure with knots.

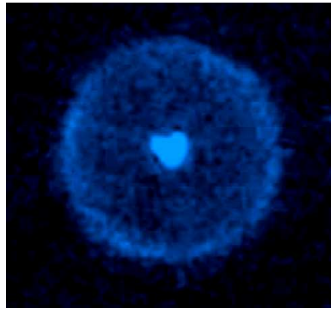
The distance from the star and clumpiness of the detached shell suggest an old mass-loss event, mentioned by [Kerschbaum et al., 2010] of  $\sim 19000$  years ago with a variation of between every 2000 and 5000 years.

In the SPIRE maps in Fig. 4.21 the detached shell in Fig. 4.21(a) and Fig. 4.21(c) is recognisable, but weak, clumpy and expanded, and shows a diamond or tetragon structure in contrast to the spherical appearance in PACS (Fig. 4.20).

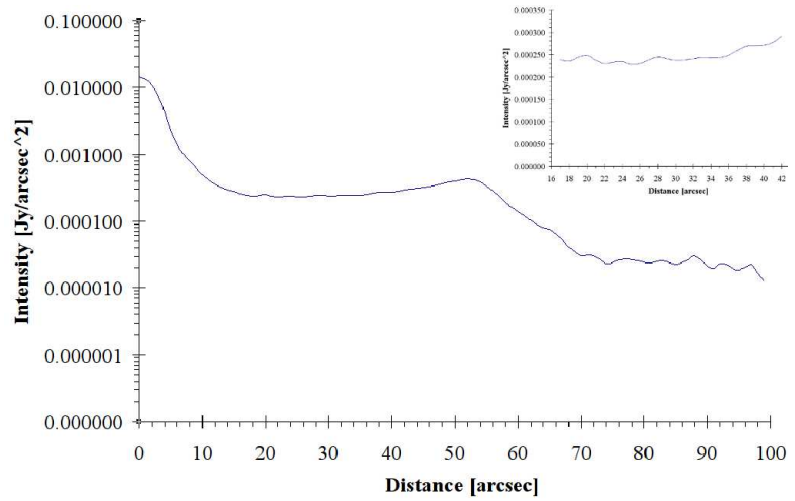
The noisy sky and the weak radiation of the object's detached shell combined with the lower resolution of SPIRE makes it difficult to resolve the detached shell.

A detached shell at  $\sim 46$  arcsec is indicated by a intensity peak in the radial profile in blue (Fig. 4.21(b)). In addition the radial profile in green (Fig. 4.21(d)) shows a plateau at 40 arcsec as tracer for a shell. These offsets from the detached shell at 52" in PACS can be explained by the contamination with fore- and background stars near the shell and its superposition with the shell, and the detached shell's shape is not a sphere anymore.

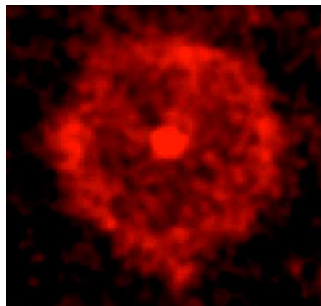
In the 500  $\mu\text{m}$  map (Fig. 4.21(e)) the science object is difficult to recognise because the object vanishes in the background and the point source, the star, is nearly invisible. The radial profile for the red channel (Fig. 4.21(f)) is not meaningful because of the



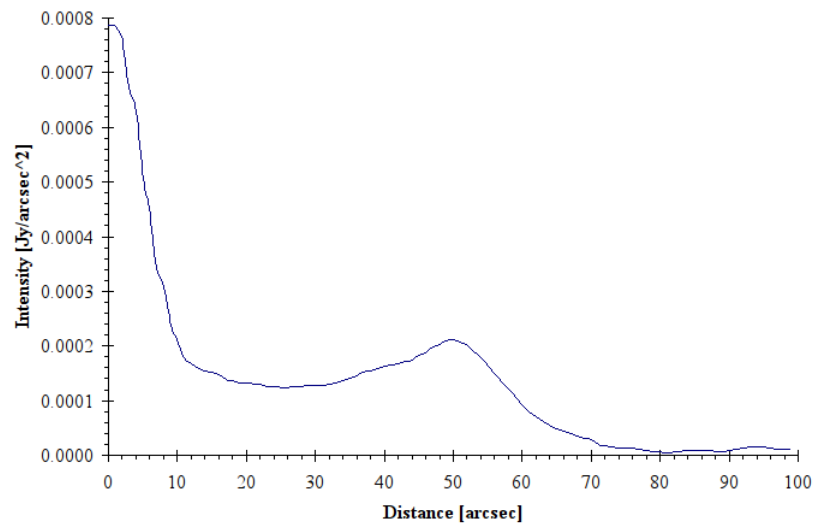
(a) blue:  $70 \mu\text{m}$ , detached shell at  $52 \text{ arcsec}$ ,  $1 \text{ pixel} = 1 \text{ arcsec}$ ,  $\text{FOV} \sim 2.5 \text{ arcmin}$ .



(b) Radial profile in blue ( $70 \mu\text{m}$ ), PACS.

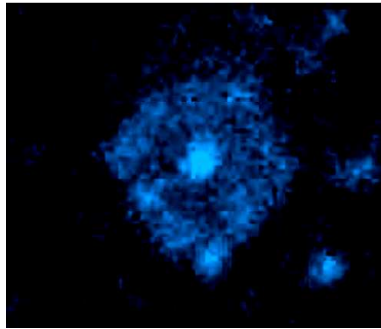


(c) red:  $160 \mu\text{m}$ , detached shell at  $\sim 52 \text{ arcsec}$ ,  $1 \text{ pixel} = 2 \text{ arcsec}$ ,  $\text{FOV} \sim 2.5 \text{ arcmin}$ .

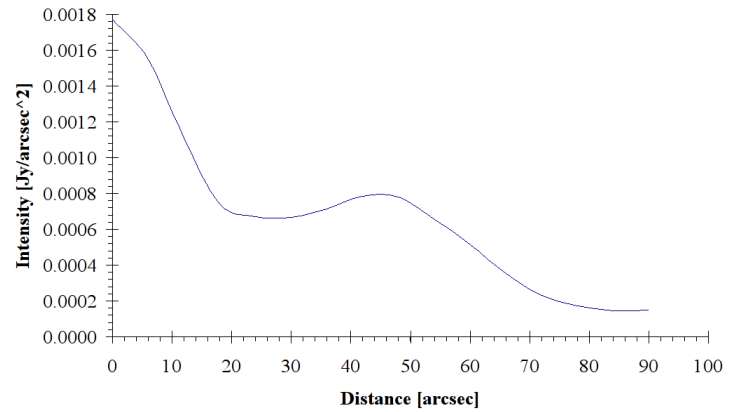


(d) Radial profile in red ( $160 \mu\text{m}$ ), PACS.

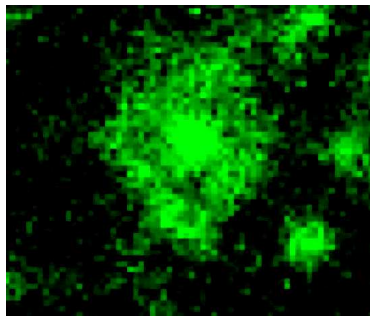
Figure 4.20: PACS observations of AQ And in  $70 \mu\text{m}$  (Fig. 4.20(a)) and  $160 \mu\text{m}$  (Fig. 4.20(c)) and their corresponding radial profiles (Fig. 4.20(b) and Fig. 4.20(d)).



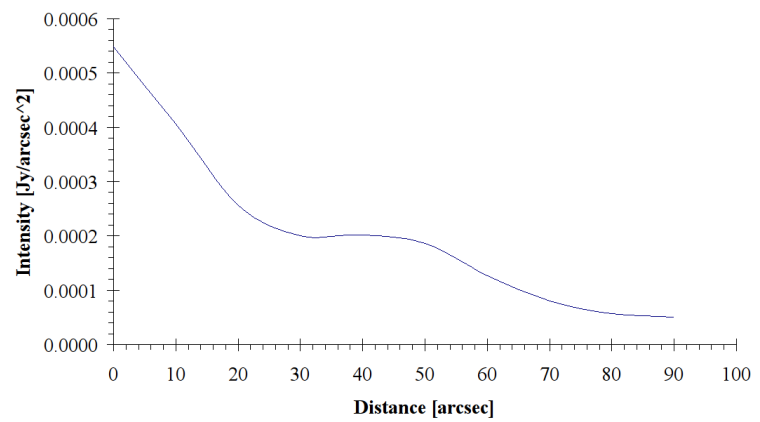
(a) blue: 250  $\mu\text{m}$ , detached shell,  
1 pixel = 3 arcsec,  
FOV:  $\sim 3$  arcmin.



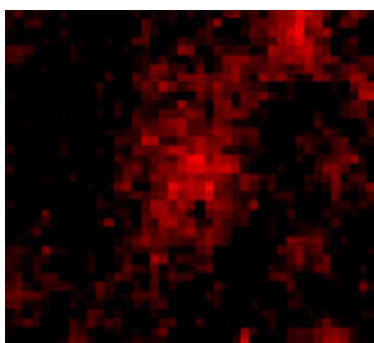
(b) Radial profile in blue (250  $\mu\text{m}$ ).



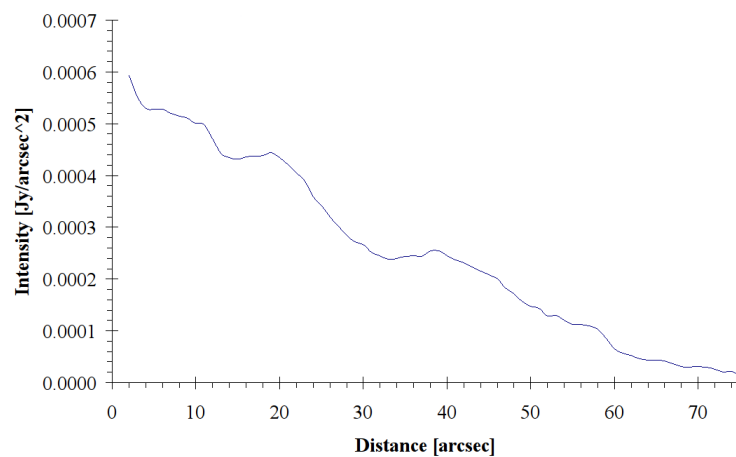
(c) green: 350  $\mu\text{m}$ , detached shell,  
1 pixel = 4 arcsec,  
FOV:  $\sim 3$  arcmin.



(d) Radial profile in green (350  $\mu\text{m}$ ).



(e) red: 500  $\mu\text{m}$ , 1 pixel = 7 arc-  
sec, FOV:  $\sim 3$  arcmin.



(f) Radial profile in red (500  $\mu\text{m}$ ).

Figure 4.21: SPIRE observations of AQ And in 250  $\mu\text{m}$  (Fig. 4.21(a)), 350  $\mu\text{m}$  (Fig. 4.21(c)) and 500  $\mu\text{m}$  (Fig. 4.21(e)) and their corresponding radial profiles (Fig. 4.21(b), Fig. 4.21(d) and Fig. 4.21(f)).

non-detection of the detached shell.

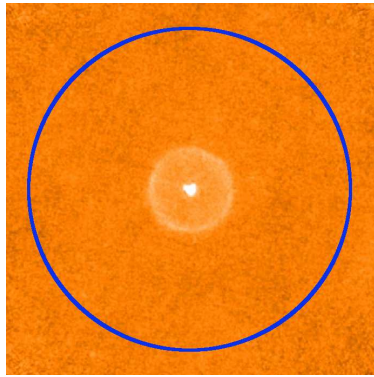
The cut levels (pixel value distribution) in Fig. 4.22 were set accordingly to saturate the science object and to reveal a possible background emission. Moreover the blue circle indicates the extended mission at 3.3 arcmin detected by [Young et al., 1993].

The sky background in PACS (Fig. 4.22(a) and Fig. 4.22(b)) is too flattened and so there is no extended emission at the outer parts of the sky visible.

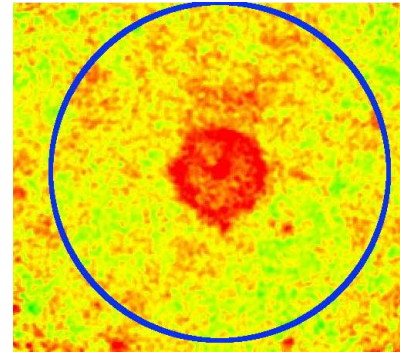
In the SPIRE sky background in Fig. 4.22(c), Fig. 4.22(d) and Fig. 4.22(e) around the blue circle there is no extended emission [Young et al., 1993] visible, only fore- and background stars.

Furthermore the blue SPIRE map (Fig. 4.22(f)), rebinned to the IRAS resolution, also revealed no emission and this is representative for further low resolution maps in SPIRE, which are not shown here.

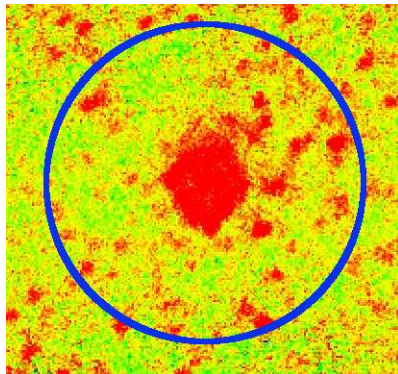
Either the faint emission was filtered out during the reduction process or the IRAS maps suffered from background contamination.



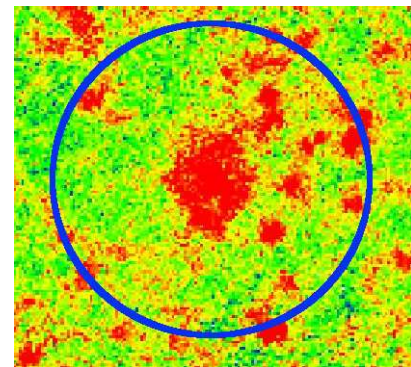
(a) blue:  $70 \mu\text{m}$ , 1 pixel = 1 arcsec, FOV:  $\sim 8$  arcmin.



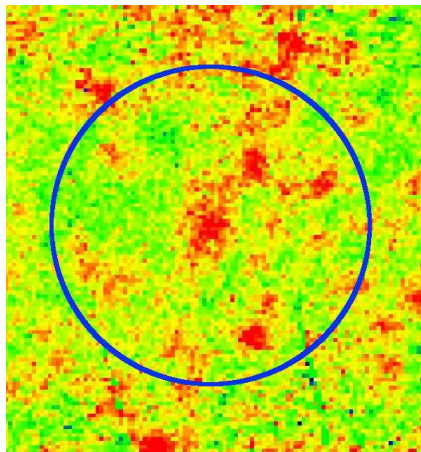
(b) red:  $160 \mu\text{m}$ , 1 pixel = 2 arcsec, FOV:  $\sim 8$  arcmin.



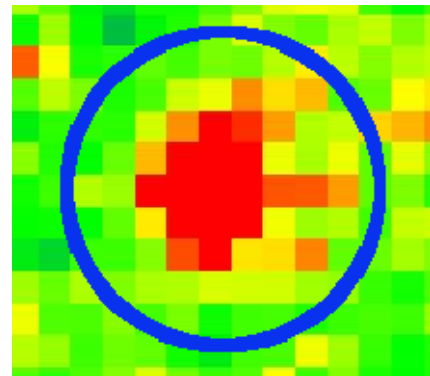
(c) blue:  $250 \mu\text{m}$ , 1 pixel = 3 arcsec, FOV:  $\sim 8$  arcmin.



(d) green:  $350 \mu\text{m}$ , 1 pixel = 4 arcsec, FOV:  $\sim 8$  arcmin.



(e) red:  $500 \mu\text{m}$ , 1 pixel = 7 arcsec, FOV:  $\sim 8.5$  arcmin.

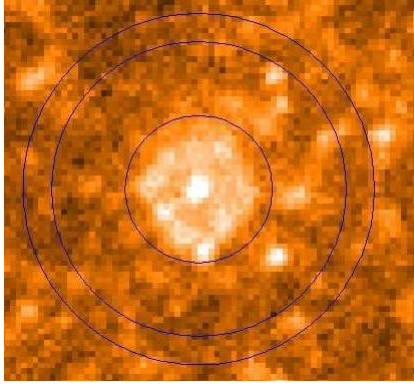


(f) blue:  $250 \mu\text{m}$ , rebinned to IRAS resolution, 1 pixel = 30 arcsec, FOV:  $\sim 8$  arcmin.

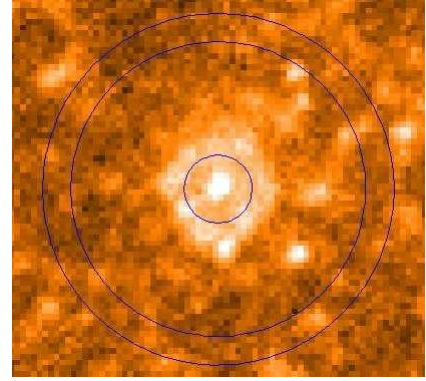
Figure 4.22: Sky background around AQ And of PACS (Fig. 4.22(a) and Fig. 4.22(b)) and SPIRE (Fig. 4.22(c), Fig. 4.22(d), Fig. 4.22(e) and Fig. 4.22(f)) observations. The blue circle indicates the extended emission at 3.3 arcmin of the IRAS mission by [Young et al., 1993].

### 4.2.2 Photometry and flux determination

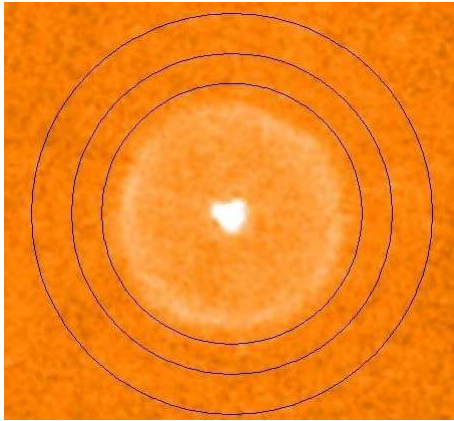
The aperture photometry and flux determination of the PACS and SPIRE maps are equally done as the object U Ant in chapter 4.1.2.



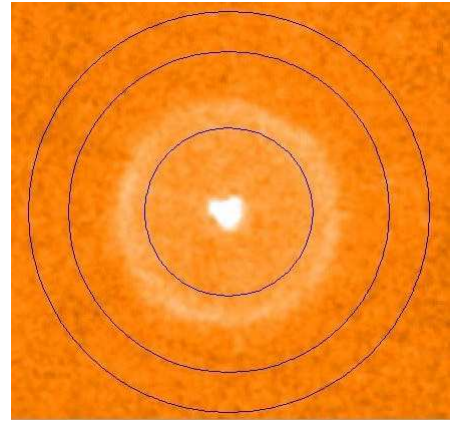
(a) entire object  $\sim 78$  arcsec, SPIRE ( $250 \mu\text{m}$ ), 1 pixel = 6 arcsec.



(b) inner part  $\sim 36$  arcsec, SPIRE ( $250 \mu\text{m}$ ).



(c) entire object  $\sim 65$  arcsec, PACS ( $70 \mu\text{m}$ ), 1 pixel = 1 arcsec.



(d) inner part  $\sim 30$  arcsec, PACS ( $70 \mu\text{m}$ ).

Figure 4.23: Aperture photometry of AQ And in SPIRE (Fig. 4.23(a) and Fig. 4.23(b)) and PACS (Fig. 4.23(c) and Fig. 4.23(d)). In Fig. 4.23(a) and Fig. 4.23(c) the entire object is measured, in Fig. 4.23(b) and Fig. 4.23(d) only the inner part without detached shell.

As an example the aperture photometry for SPIRE and PACS in Fig. 4.23 is performed for the blue channel for each instrument. Further results for the other detectors are summarized in Table 4.11.

In SPIRE Fig. 4.23(a) the entire object is measured with the task `annularAperturePhotometry`. The aperture size is 78 arcsec and the sky annulus was set in an area with only few background stars.

The total flux density of the entire object results in  $10.82 \pm 3.3$  Jy · pixel per beam, which leads to a corrected flux density of 1.102 Jy.

For the inner part of AQ And (Fig. 4.23(b)) an aperture size of 36 arcsec was chosen. As result the total flux density of the inner part ( $\sim 36$  arcsec) results in a corrected flux density of 0.369 Jy.

The subtraction of the entire object and the inner part is calculated to a detached shell total flux density of 0.733 Jy.

In PACS (Fig. 4.23(c)) the flux density from the entire object (aperture size:  $\sim 65$  arcsec) is 3.77 Jy and is comparable with  $4.3 \text{ Jy} \pm 0.7 \text{ Jy}$  from [Kerschbaum et al., 2010]). The variation in the flux density is caused by different flux calibration versions and reduction methods.

For the inner part (Fig. 4.23(d)) an aperture size of 30 arcsec was used to derive a detached shell flux density of 1.755 Jy.

In addition to the results of the aperture photometry of SPIRE and PACS, an additional flux density was obtained from the IRAS mission [Young et al., 1993] in the  $60 \mu\text{m}$  band and is shown in Table 4.11.

Due to the fact that there was no detached shell measurable for the SPIRE red (Fig. 4.21(e)), only the flux density of the entire object is given.

| wavelength [ $\mu\text{m}$ ] | pixel ["] | aperture ["] | inner part ["] | $Y_{\text{object}}$ [Jy] | $Y_{\text{shell}}$ [Jy] |
|------------------------------|-----------|--------------|----------------|--------------------------|-------------------------|
| SPIRE: 250                   | 6         | 78           | 36             | 1.102                    | 0.733                   |
| 350                          | 10        | 80           | 40             | 0.41475                  | 0.24045                 |
| 500                          | 14        | 70           | -              | 0.069067                 | -                       |
| PACS: 70                     | 1         | 65           | 30             | 3.77                     | 1.755                   |
| 160                          | 2         | 65           | 30             | 2.078                    | 1.4952                  |
| IRAS: 60                     | $\sim 30$ | -            | -              | 3.8                      | -                       |

Table 4.11: Summary of the aperture photometry of the SPIRE, PACS and IRAS [Young et al., 1993] observations. The aperture size was laid over the entire object and the inner part was measured without the detached shell.

$Y_{\text{object}}$  ... calibrated and corrected flux density in Janskys

$Y_{\text{shell}}$  ... flux density of the detached shell in Janskys.

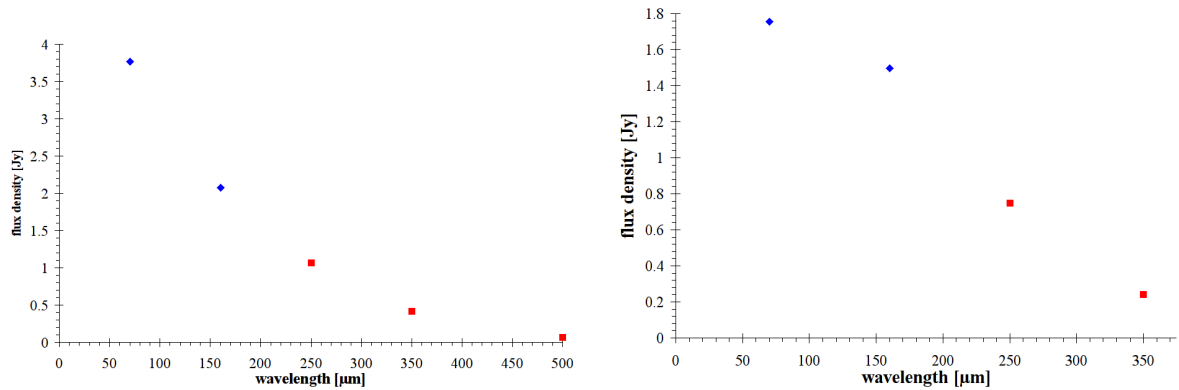
In Fig. 4.24 the data results from the photometry are plotted as flux density versus wavelength.

Fig. 4.24(a) shows the flux densities of the entire object. A further plot for the flux densities of the detached shell is shown in Fig. 4.24(b).

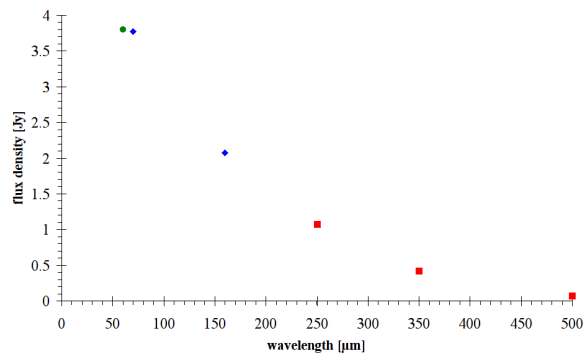
In the next plot (Fig. 4.24(c)) the additional flux density from the IRAS mission [Young et al., 1993] is included.



These data results can be compared with the black body radiation to derive a temperature estimation. The next chapter describes the temperature estimation for two methods.



(a) Flux density vs wavelength of the entire object; PACS (blue diamond) + SPIRE (red square). (b) Flux density vs wavelength of the detached shell; PACS (blue diamond) + SPIRE (red square).



(c) Flux density vs wavelength of the entire object; PACS (blue diamond) + SPIRE (red square) + IRAS (green circle).

Figure 4.24: AQ And:

Fig. 4.24(a): SED of the entire object from the PACS and SPIRE photometry.

Fig. 4.24(b): SED of the detached shell from the PACS and SPIRE photometry.

Fig. 4.24(c): SED of the entire object from the PACS, SPIRE and IRAS photometry [Young et al., 1993].

### 4.2.2.1 Black body estimation

#### Planck fitting with amorphous carbon

As it was performed at the object U Ant, a rough estimate of the temperature is calculated with the help of the Planck black body law and with assumptions of optical properties of amorphous carbon dust.

The same procedure as for U Ant was applied for AQ And and with the ratios of  $F_{\nu,70}$  and  $F_{\nu,160}$  and  $F_{\nu,160}$  and  $F_{\nu,250}$ . With equation 4.4 combined with the Q-factors from the interpolation (Table 4.5) the temperature for the entire object and detached shell can be estimated (Table 4.12).

| wavelength ratio | $T_{\text{object}}$ [K] | $T_{\text{shell}}$ [K] |
|------------------|-------------------------|------------------------|
| 70/160           | 48.3                    | 40.3                   |
| 160/250          | 27                      | 28                     |

Table 4.12: Results for the temperature of the entire object and the detached shell from the Planck fitting with AmC.

#### Planck fitting with amorphous carbon and PACS filter response

As I showed for the object U Ant, the derived temperature can be compared to the BB theoretical model combined with the PACS filter response (Fig. 4.13), which was applied after an algorithm by Stefano Pezzuto ([Pezzuto, 2012]). So the algorithm can only be used for PACS flux densities.

When modelled as a BB for PACS, the detached shell has a temperature of 40 K and the entire object has 48 K. This is not too far away from the simulation in the publication by [Kerschbaum et al., 2010] with 27.5 K until 44.8 K.

Furthermore the Planck fittings without the PACS filter response is in a perfect agreement with the Planck fittings with the PACS filter response.

A summary of the derived temperatures is given in Table 4.13. The results of the temperature estimation of both Planck fittings suit quite nicely to the results of temperature range of [Kerschbaum et al., 2010], although the Planck fittings must be considered as rough estimate.

| temperature estimation method    | wavelength ratio | $T_{\text{object}}$ [K] | $T_{\text{shell}}$ [K] |
|----------------------------------|------------------|-------------------------|------------------------|
| Planck fitting with AmC          | 70/160           | 48.3                    | 40.3                   |
|                                  | 160/250          | 27                      | 28                     |
| Planck fitting with AmC and PACS | 70/160           | 48                      | 40                     |
| DUSTY, [Kerschbaum et al., 2010] | -                | -                       | 27.5 - 44.8            |

Table 4.13: Results for the temperature of the entire object and the detached shell from the Planck fitting with AmC, the Planck fitting with the PACS filter response and [Kerschbaum et al., 2010].

### 4.2.3 Model fitting with DUSTY

The same tasks as U Ant were performed for the object AQ And to create a model, which fits with the observed radial profile optimally.

#### Effects on the shell radius by varying the input parameters

The base model is used as starting point, from which the parameters will be changed to fit the observed radial profile.

In Table 4.14 the derived parameters are shown and Fig. 4.25 illustrates the DUSTY base model (blue) with the observation (red).

In the radial profiles of AQ And in Fig. 4.25, both intensity peaks of the detached shell are located at 52".

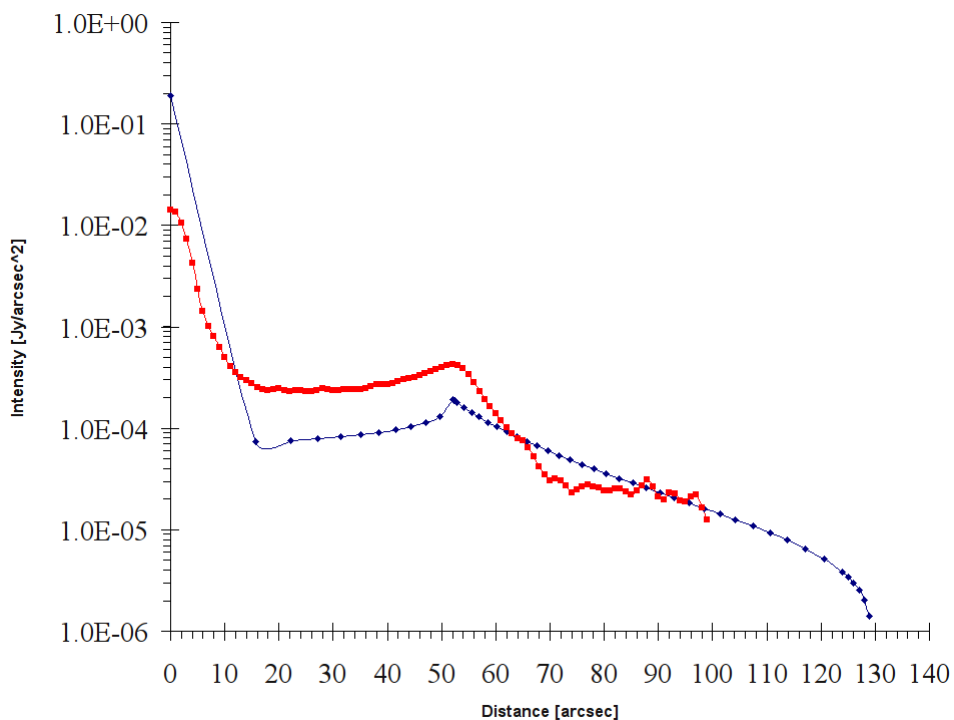


Figure 4.25: Radial profile of AQ And; red: PACS ( $70 \mu\text{m}$ ) observation, blue: DUSTY base model

|                        |                            |                       |               |
|------------------------|----------------------------|-----------------------|---------------|
| $T_{\text{eff}}$ [K]   | luminosity [ $L_{\odot}$ ] | $\Delta R=Y$          | distance [pc] |
| 2660                   | 12000                      | 2.5                   | 1015          |
| dust species           | optical depth $\tau$       | $T_{\text{dust}}$ [K] |               |
| AmC-Hn, [Hanner, 1988] | 0.001                      | 50.1                  |               |

Table 4.14: DUSTY input parameters for the AQ And base model. effective temperature of the star in Kelvin as BB, luminosity of the star, shell thickness ( $Y=r_{\text{out}}/r_1$ ) relative to the inner shell radius  $r_1$ , distance in pc, dust species with 100 % AmC by Hanner [Hanner, 1988], optical depth of the dust shell, temperature at the inner boundary of the shell in Kelvin.

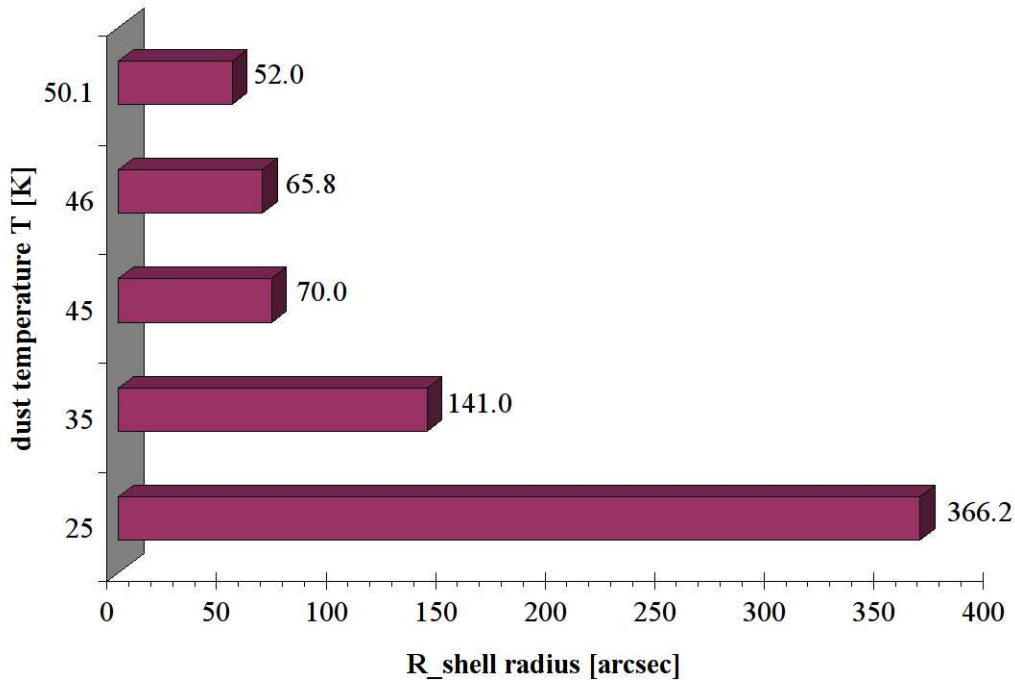
**Dust temperature on inner boundary:**

Figure 4.26: Inner shell radius as a function of the dust temperature on the inner boundary; beginning at 25 K until shell radius (52 arcsec) is fitted at 50.1 K

At a dust temperature of 25 K the position of shell radius enlarges to  $\sim 366$  arcsec. Changing the dust temperature to 35 K leads to a shell radius at 141 arcsec. Variations in a 1-K-range from 45 K (70 arcsec) to 46 K (65.83 arcsec) result in 4.17 arcsec difference in the shell radius. The inner shell radius is highly dependent (inverse proportional) on the inner dust temperature and that's why a shell with lower dust temperature is farther away from the star because the photon flux is weaker and thus the dust shell is not warmed up strongly through radiation.

**Distance:**

There are two verified distances known for AQ And, 825 pc (PL-relations, [Groenewegen and Whitelock, 1996]) and 1015 pc (Hipparchos, [Bergeat and Chevallier, 2005]).

Using the distance of 1015 pc the detached shell's radius is  $\sim 52$  arcsec in the base model. The distance of 825 pc will change the radius to  $\sim 64$  arcsec, which is  $\sim 23\%$  larger ( $\sim 12$  arcsec) than the Hipparchos distance. A closer distance to our solar system let the shell appear larger. To correct the shell radius offset of  $\sim 12$  arcsec, when using the distance of 825 pc, it is necessary to raise the dust temperature by 3 K.

**Shell thickness:**

The shell positions in Fig. 4.27 remain unchanged, but the shells enlarge due to larger thickness at  $\Delta R = 2.5$  and  $\Delta R = 5$ , and the flux density distributes over a larger area. So the flux densities of the larger shells are weaker, because of the extension. Furthermore the flux density gradients after the peak are different for each shell thickness.

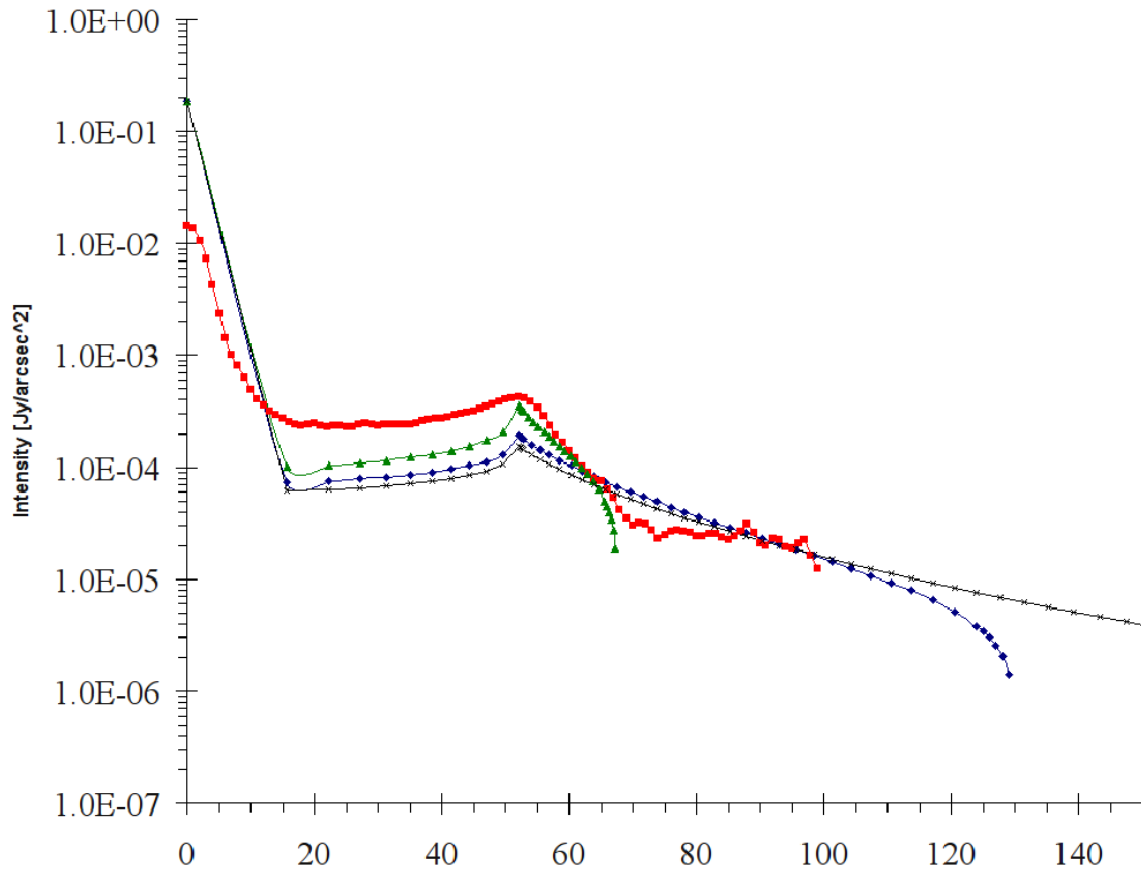


Figure 4.27: Radial profiles of AQ And; red: PACS ( $70 \mu\text{m}$ ) observation, DUSTY base model with different shell thickness: blue:  $\Delta R = 2.5$ , green:  $\Delta R = 1.3$ , black:  $\Delta R = 5$

**Chemical composition and the optical depth  $\tau$ :**

The dependence of the different dust grains on the inner shell radius is similar to that of U Ant. In Fig. 4.28 the silicate grains Sil-DL [Draine and Lee, 1984], Sil-Ow and Sil-Oc [Ossenkopf et al., 1992] are stable minerals and thus more resistant against the radiation than amorphous carbon. So the shells can be placed closer to the star at the same temperature (50.1 K).

Graphite grf-DL [Draine and Lee, 1984] is a stable form of carbon (allotrope of carbon) in hexagonal structure, which can absorb high amounts of radiation similar to silicates and locates the shell at  $\sim 19.2 - 23$  arcsec.

Amorphous carbon dust AmC-Zb1-Zb2 [Zubko et al., 1996] and ice-coated AmC grains [Preibisch et al., 1993], and AmC-Hn ([Hanner, 1988] have no sorted structures and a low packing density. To survive the radiation, the shells must be more distant from the star.

AmC-Zb3 was stabilized with  $H_2$  atmosphere under 10 mbar, which is called “hydrogenated amorphous carbon”, and thus is more robust. So it blocks the radiation from the star better in a similar way as graphite.

Silicon-Carbide SiC-Pg [Pegourie, 1988] is a compound of silicon and carbon with weak resistance against radiation and sets the shell radius like AmC-Hn.

In the optically thick case ( $\tau \gg 1$ ;  $\tau = 5$ ) the shell is dominated by absorption and scattering of radiation in contrast to an optically thin shell ( $\tau \ll 1$ ;  $\tau = 0.001$ ). The shell is heated up and thus the dust can be easier dissociated. So the shell at each dust species at  $\tau = 5$  must be placed more distant from the star.



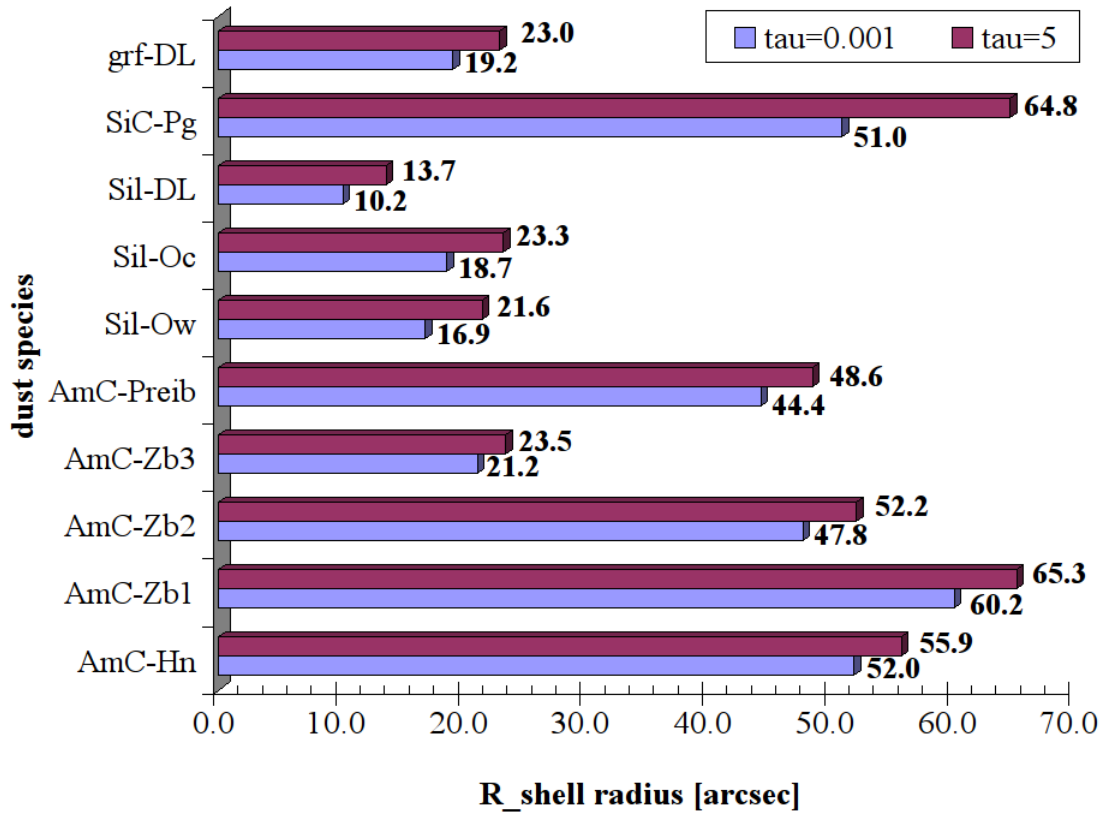


Figure 4.28: Different dust species in the optically thin ( $\tau=0.001$ ) and thick ( $\tau=5$ ) case at a constant temperature of 50.1 K.

grf-DL graphite [Draine and Lee, 1984], SiC-Pg silicon-carbide [Pegourie, 1988], Sil-DL astronomical silicate [Draine and Lee, 1984], Sil-Ow and Sil-Oc warm(O-deficient) and cold (O-rich) silicates [Ossenkopf et al., 1992], AmC-Preib ice-coated amorphous carbon grains [Preibisch et al., 1993], AmC-Zb1-3 three different cosmic amorphous carbon analogue grains [Zubko et al., 1996], AmC-Hn amorphous carbon grains from comets Halley and Wilson [Hanner, 1988].

### Final DUSTY model for AQ And

The final DUSTY model consists of following parameters, which are given in Table 4.15 together with the DUSTY model by [Kerschbaum et al., 2010]. In addition the temperature estimation of the different methods is itemised in Table 4.16.

When considering the differences of the distance (3 K higher  $T_{\text{dust}}$ ) and dust species (1.8 K lower  $T_{\text{dust}}$ ) in the final model and [Kerschbaum et al., 2010] model, the dust temperature would be by 1.2 K higher (3 K minus 1.8 K) for the final model, which is negligible. The difference of the effective temperature of 40 K between the models would result in a 0.2 K difference and thus not relevant. Discrepancies in the shell thickness and the optical depth only change the shell's shape and flux density. The overall uncertainty of the parameters like the distance, the dust species and the effective temperature amounts to only 1.4 K difference.

In [Kerschbaum et al., 2010] the authors used different shells to reproduce the radial profile. That's why the comparison between the final DUSTY and the [Kerschbaum et al., 2010] model leads to an offset of 5.4 K in the dust temperature to highest value of 44.8 K, and to an offset of 22.7 K to the lower limit of 27.5 K.

So the dust temperature of 50.2 K fits well with the highest temperature value in [Kerschbaum et al., 2010] of 44.8 K. Furthermore the lower limit of 27.5 K is covered by the Planck fitting of 40.3 K and 28 K (Table 4.16) and in addition the Planck fitting with the PACS filter response of 40 K lies in between the dust temperature range in [Kerschbaum et al., 2010].

In the general the dust shell temperature can be estimated to a temperature range of 28 – 50.2 K, which also fits into the temperatures of [Kerschbaum et al., 2010].

The small deviations in temperature can be explained, like at U Ant, with additional assumptions to the BB of the radiation source by [Aringer et al., 2009], who use synthetic models for atmospheres of carbon stars with different opacities, scattering coefficients and abundances of molecules.

In addition an attached shell with an inner temperature of 1200 K was superimposed in [Kerschbaum et al., 2010] to fit the radial profile, but it also changes the profile of the radiation source and thus can result in a different flux density and dust shell temperature. The assumption as optically thin shell can also be considered as possible error source.

The mass-loss rate of the detached shell of  $7.4 \cdot 10^{-7} M_{\odot} \text{ year}^{-1}$  with a grain density of  $1.85 \text{ g cm}^{-3}$  and a gas-to-dust-ratio of 200 is within the range of mass-loss rates between 0.3 and  $152 \cdot 10^{-7} M_{\odot} \text{ year}^{-1}$  by [Kerschbaum et al., 2010].

The observed radial profile in PACS (70  $\mu\text{m}$ ) and the final DUSTY model are shown in Fig. 4.29. The model of the detached shell is placed at 51.7 arcsec and the observed shell is located at 52 arcsec. This offset is used for the preparation of the convolution with the Herschel optics because the convolution shifts the shell by  $\sim 0.3$  arcsec and rounds up the detached shell's shape (Fig. 4.30).

The result of the convolution (green model) is illustrated in Fig. 4.30, which shows a rounded up detached shell, which covers the observation nearly completely (Fig. 4.30(b)). Because of the missing attached shell, the inner part up to  $\sim 45$  arcsec deviates from the observation. So at the centre of the star part there is an offset of 0.04 Jy per arcsec<sup>2</sup>, which is very small. Furthermore the sky background difference of 0.1 Jy per arcsec<sup>2</sup>, beginning at 60 arcsec, cannot modeled in DUSTY and is negligible.

| Final DUSTY model               |                            |                       |               |
|---------------------------------|----------------------------|-----------------------|---------------|
| $T_{\text{eff}}$ [K]            | luminosity [ $L_{\odot}$ ] | $\Delta R=Y$          | distance [pc] |
| 2660                            | 12000                      | 1.15                  | 1015          |
| dust species                    | optical depth $\tau$       | $T_{\text{dust}}$ [K] |               |
| AmC-Hn, [Hanner, 1988]          | 0.00155                    | 50.2                  |               |
| [Kerschbaum et al., 2010] model |                            |                       |               |
| $T_{\text{eff}}$ [K]            | luminosity [ $L_{\odot}$ ] | $\Delta R=Y$          | distance [pc] |
| 2700                            | 12000                      | 1.01 – 2              | 825           |
| dust species                    | optical depth $\tau$       | $T_{\text{dust}}$ [K] |               |
| AmC, [Preibisch et al., 1993]   | 0.003                      | 27.5 – 44.8           |               |

Table 4.15: DUSTY final model parameters for the AQ And and [Kerschbaum et al., 2010] model; effective temperature of the star, luminosity of the star, shell thickness ( $Y=r_{\text{out}}/r_1$ ) relative to the inner shell radius  $r_1$ , distance in pc, dust species, optical depth of the dust shell and temperature at the inner boundary of the shell.

| temperature estimation method          | wavelength | $T_{\text{shell}}$ [K] |
|--|------------|------------------------|
| Planck fitting with AmC                | 70/160     | 40.3                   |
|  | 160/250    | 28                     |
| Planck fitting with AmC and PACS       | 70/160     | 40                     |
| DUSTY, [Kerschbaum et al., 2010] model | 70         | 27.5 – 44.8            |
| DUSTY, thesis' results                 | 70         | 50.2                   |

Table 4.16: Results for the temperature of the detached shell from the Planck fitting with AmC, the Planck fitting with the PACS filter response, [Kerschbaum et al., 2010] model and the results of this master thesis.

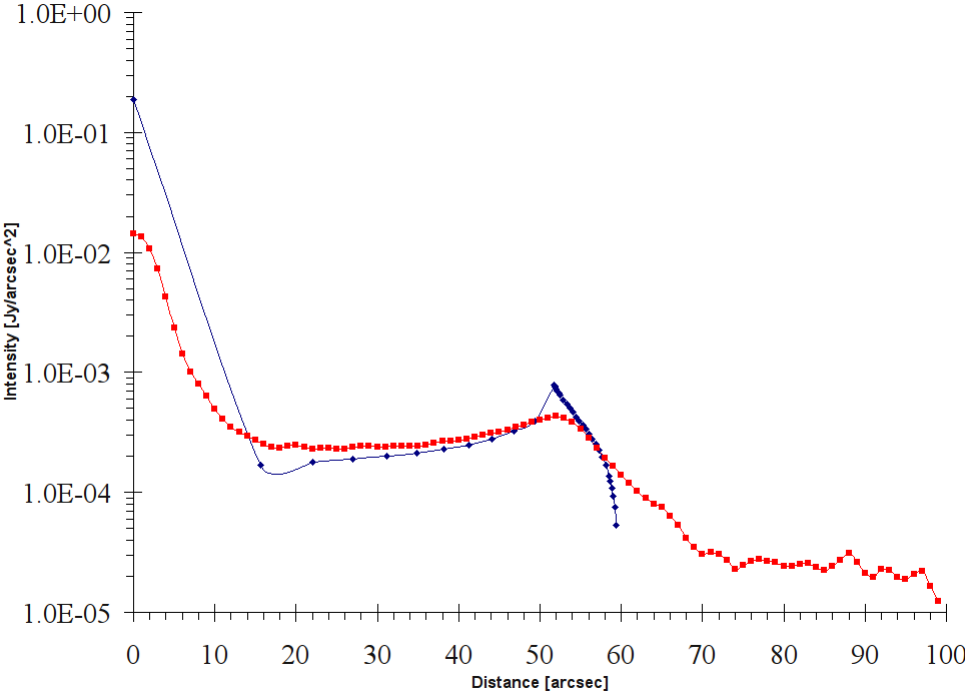
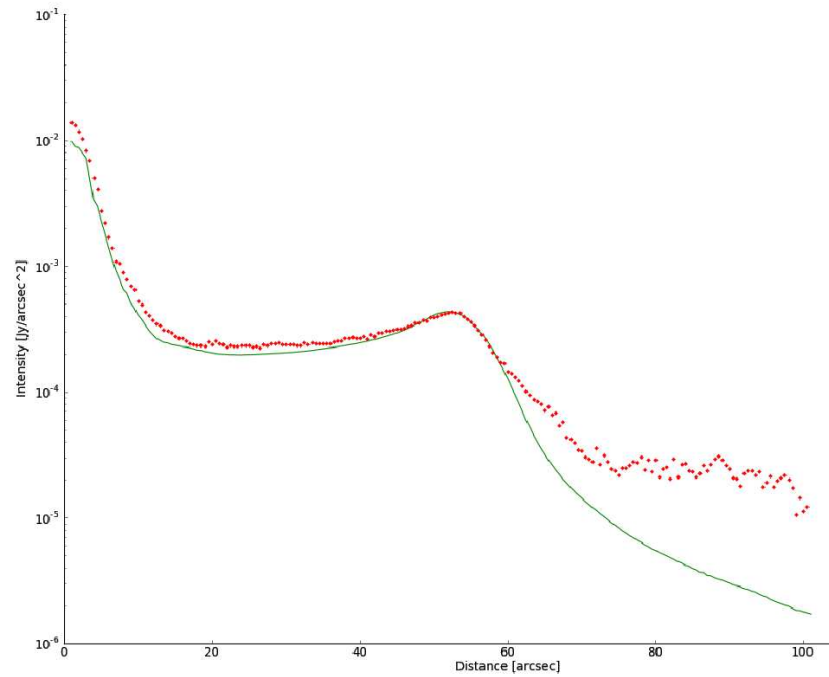
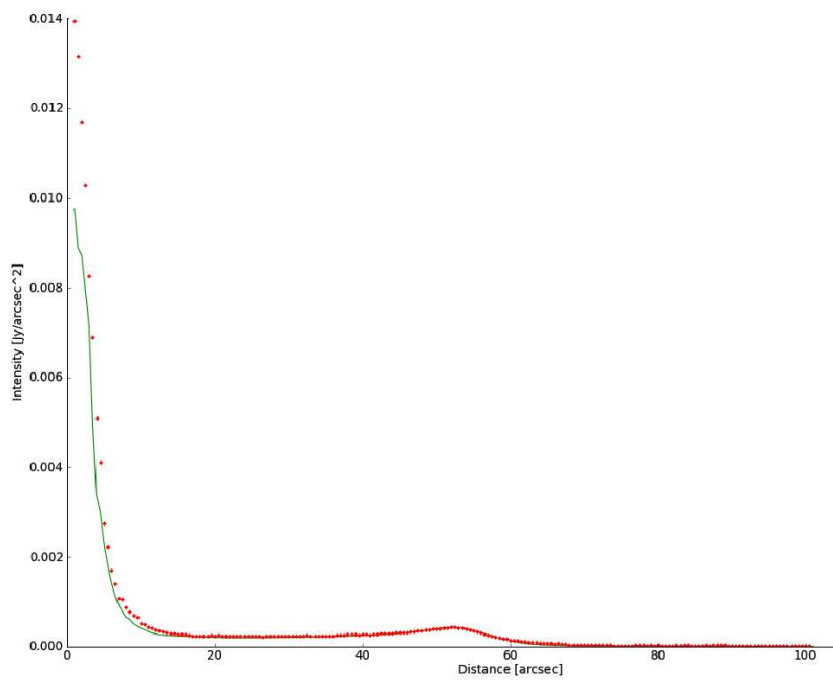


Figure 4.29: Final DUSTY model; red: observed radial profile in 70  $\mu\text{m}$ , blue: fitted DUSTY model without convolution.



(a) red: observed radial profile, green: fitted DUSTY model with convolution with the Herschel PSF in logarithmic scale.



(b) red: observed radial profile, green: fitted DUSTY model with convolution with the Herschel PSF.

Figure 4.30: Final DUSTY model for AQ And as logarithmic (Fig. 4.30(a)) and linear (Fig. 4.30(b)) plot.

#### 4.2.4 Conclusion and interpretation

The detached shell of AQ And was confirmed again in the PACS and SPIRE maps. In PACS the location of the detached dust shell is 52 arcsec, which was also observed in [Kerschbaum et al., 2010]. In this thesis further observations in SPIRE traced shells at 40 and 46", and not at 52". This discrepancy can be caused through the lower resolution and the background contamination by fore- and background stars within the shell. Moreover the extended emission, which was found by [Young et al., 1993], was neither detected in PACS and ISO [Kerschbaum et al., 2010] nor in SPIRE and thus suggests reduction problems like background contamination of the IRAS map.

For the comparison of observation and modeling of the detached shell, the DUSTY fitting of the radial profile of PACS (70  $\mu\text{m}$ ) was successfully performed. The final model is in good agreement with the observation except in the inner stellar part, which needs an attached shell to represent the recent mass-loss.

Offsets between final model and the model by [Kerschbaum et al., 2010] can be explained by further assumptions of the atmosphere of the AGB-star with different opacities and scattering coefficients [Aringer et al., 2009].

The derived dust shell temperature amounts to 50.2 K, which fits perfectly in the temperature range of 27.5 K – 44.8 K by [Kerschbaum et al., 2010] with a small deviation. But both Planck fittings with  $\sim 40$  K and 28 K reproduce the lower and upper limit of the temperature range and not the DUSTY modeling, which can be traced back to the measurement uncertainties in SPIRE and the uncertainty in the absorptions coefficients by [Draine, 1981].

An overall temperature estimation of the detached dust shell can be derived to 28 K - 50.2 K. This is a smaller uncertainty range (22.2 K) than of the object U Ant (37.2 K). Due to the large mass-loss rate range of  $0.3 - 152 \cdot 10^{-7} M_{\odot} \text{ year}^{-1}$  by [Kerschbaum et al., 2010], the mass loss rate of  $7.4 \cdot 10^{-7} M_{\odot} \text{ year}^{-1}$  in the final model fits nicely and is in the same order of magnitude as U Ant.

# Bibliography

- [Arimatsu et al., 2011] Arimatsu, K., Izumiura, H., Ueta, T., Yamamura, I., and Onaka, T. (2011). Detection of the Detached Dust Shell of U Antliae at Mid-infrared Wavelengths with AKARI/IRC. *The Astrophysical Journal Letters*, 729:L19.
- [Aringer et al., 2009] Aringer, B., Girardi, L., Nowotny, W., Marigo, P., and Lederer, M. T. (2009). Synthetic photometry for carbon rich giants. I. Hydrostatic dust-free models. *Astronomy and Astrophysics*, 503:913–928.
- [Bergeat and Chevallier, 2005] Bergeat, J. and Chevallier, L. (2005). The mass loss of C-rich giants. *Astronomy and Astrophysics*, 429:235–246.
- [Cantalupo et al., 2010] Cantalupo, C. M., Borrill, J. D., Jaffe, A. H., Kisner, T. S., and Stompor, R. (2010). MADmap: A Massively Parallel Maximum Likelihood Cosmic Microwave Background Map-maker. *American Astronomy Society*, 187:212–227.
- [Draine, 1981] Draine, B. T. (1981). Infrared emission from dust in shocked gas. *Astrophysical Journal*, 245:880–890.
- [Draine and Lee, 1984] Draine, B. T. and Lee, H. M. (1984). Optical properties of interstellar graphite and silicate grains. *Astrophysical Journal*, 285:89–108.
- [Eggen, 1972] Eggen, O. J. (1972). The classification of intrinsic variable stars. I. The red variables of type N. *Astrophysical Journal*, 174:45.
- [ESA, 2012a] ESA (2012a). European Space Agency, Herschel Website; Overview and Images of the Herschel Space Telescope and further links.  
[http://www.esa.int/esaSC/120390\\_index\\_0\\_m.html](http://www.esa.int/esaSC/120390_index_0_m.html)  
<http://hipparcos.esa.int/science-e/www/object/index.cfm?fobjectid=34695>  
<http://sci.esa.int/science-e/www/object/index.cfm?fobjectid=34682>  
<http://sci.esa.int/science-e/www/object/index.cfm?fobjectid=34699>  
[http://www.esa.int/esaSC/120390\\_index\\_0\\_m.html](http://www.esa.int/esaSC/120390_index_0_m.html)  
<http://herschel.esac.esa.int/links.shtml>.
- [ESA, 2012b] ESA (2012b). PACS filters and further details.  
<https://nhscsci.ipac.caltech.edu/sc/index.php/Pacs/FilterCurves>.
- [González Delgado et al., 2001] González Delgado, D., Olofsson, H., Schwarz, H. E., Eriksson, K., and Gustafsson, B. (2001). Imaging of detached shells around the carbon stars R Scl and U Ant through scattered stellar light. *Astronomy and Astrophysics*, 372:885–898.

- [González Delgado et al., 2003] González Delgado, D., Olofsson, H., Schwarz, H. E., Eriksson, K., Gustafsson, B., and Gledhill, T. (2003). Imaging polarimetry of stellar light scattered in detached shells around the carbon stars R Scl and U Ant. *Astronomy and Astrophysics*, 399:1021–1035.
- [Griffin et al., 2010] Griffin, M. J., Abergel, A., Abreu, A., Ade, P. A. R., André, P., Augueres, J.-L., Babbedge, T., and more (2010). The Herschel-SPIRE instrument and its in-flight performance. *Astronomy and Astrophysics*, 518:L3.
- [Groenewegen et al., 2011] Groenewegen, M. A. T., Waelkens, C., Barlow, M. J., Kerschbaum, F., Garcia-Lario, P., Cernicharo, J., Blommaert, J. A. D. L., Bouwman, J., Cohen, M., Cox, N., Decin, L., Exter, K., Gear, W. K., Gomez, H. L., Hargrave, P. C., Henning, T., Hutsemékers, D., Ivison, R. J., Jorissen, A., Krause, O., Ladjal, D., Leeks, S. J., Lim, T. L., Matsuura, M., Nazé, Y., Olofsson, G., Ottensamer, R., Polehampton, E., Posch, T., Rauw, G., Royer, P., Sibthorpe, B., Swinyard, B. M., Ueta, T., Vamvatira-Nakou, C., Vandenbussche, B., van de Steene, G. C., van Eck, S., van Hoof, P. A. M., van Winckel, H., Verdugo, E., and Wesson, R. (2011). MESS (Mass-loss of Evolved StarS), a Herschel key program. *Astronomy and Astrophysics*, 526:A162+.
- [Groenewegen and Whitelock, 1996] Groenewegen, M. A. T. and Whitelock, P. A. (1996). A revised period-luminosity relation for carbon Miras. *Monthly Notices of the Royal Astronomical Society*, 281:1347–1351.
- [Hanner, 1988] Hanner, M. (1988). Grain optical properties. Technical report.
- [Harm J. Habing, 2003] Harm J. Habing, H. O. (2003). *Book: Asymptotic Giant Branch stars*.
- [Hron and Le Bertre, 2012] Hron, J. and Le Bertre, T. (2012). Schematic view of an agb-star. Institute of Astronomy, Vienna, Austria.
- [Ivezic and Elitzur, 1997] Ivezic, Z. and Elitzur, M. (1997). Self-similarity and scaling behaviour of infrared emission from radiatively heated dust - I. Theory. *Monthly Notices of the Royal Astronomical Society*, 287:799–811.
- [Ivezic and Elitzur, 2012] Ivezic, Z. and Elitzur, M. (2012). DUSTY website. <http://www.pa.uky.edu/~moshe/dusty/>.
- [Izumiura et al., 1997] Izumiura, H., Waters, L. B. F. M., de Jong, T., Loup, C., Bontekoe, T. R., and Kester, D. J. M. (1997). A double dust shell surrounding the carbon star U Antliae. *Astronomy and Astrophysics*, 323:449–460.
- [Kerschbaum et al., 2010] Kerschbaum, F., Ladjal, D., Ottensamer, R., Groenewegen, M. A. T., Mecina, M., Blommaert, J. A. D. L., Baumann, B., Decin, L., Vandenbussche, B., Waelkens, C., Posch, T., Huygen, E., De Meester, W., Regibo, S., Royer, P., Exter, K., and Jean, C. (2010). The detached dust shells of AQ Andromedae, U Antliae, and TT Cygni. *Astronomy and Astrophysics*, 518:L140.



- [Kiss et al., 1999] Kiss, L. L., Szatmáry, K., Cadmus, Jr., R. R., and Mattei, J. A. (1999). Multiperiodicity in semiregular variables. I. General properties. *Astronomy and Astrophysics*, 346:542–555.
- [Maercker et al., 2010] Maercker, M., Olofsson, H., Eriksson, K., Gustafsson, B., and Schöier, F. L. (2010). The detached dust and gas shells around the carbon star U Antliae. *Astronomy and Astrophysics*, 511:A37.
- [Mecina, 2012] Mecina, M. (2012). Imaging and Photometry of TTCYG and UXDRAC using the Herschel Space Telescope. Master’s thesis, Institute of Astronomy, Vienna, Austria.
- [Olofsson et al., 1988] Olofsson, H., Eriksson, K., and Gustafsson, B. (1988). SEST CO ( $J = 1 - 0$ ) observations of carbon-rich circumstellar envelopes. *Astronomy and Astrophysics*, 196:L1–L4.
- [Ossenkopf et al., 1992] Ossenkopf, V., Henning, T., and Mathis, J. S. (1992). Constraints on cosmic silicates. *Astronomy and Astrophysics*, 261:567–578.
- [Ott, 2010] Ott, S. (2010). The Herschel Data Processing System HIPE and Pipelines Up and Running Since the Start of the Mission. In Y. Mizumoto, K.-I. Morita, & M. Ohishi, editor, *Astronomical Data Analysis Software and Systems XIX*, volume 434 of *Astronomical Society of the Pacific Conference Series*, page 139.
- [Pegourie, 1988] Pegourie, B. (1988). Optical properties of alpha silicon carbide. *Astronomy and Astrophysics*, 194:335–339.
- [Pezzuto, 2012] Pezzuto, S. (2012). Python scripts for the theoretical model of the observed PACS flux with the filter response for black body radiation.
- [Pilbratt et al., 2010] Pilbratt, G. L., Riedinger, J. R., Passvogel, T., Crone, G., Doyle, D., Gageur, U., Heras, A. M., Jewell, C., Metcalfe, L., Ott, S., and Schmidt, M. (2010). Herschel Space Observatory. An ESA facility for far-infrared and submillimetre astronomy. *Astronomy and Astrophysics*, 518:L1.
- [Poglitsch et al., 2010] Poglitsch, A., Waelkens, C., Geis, N., Feuchtgruber, H., Vandenbussche, B., Rodriguez, L., Krause, O., and more (2010). The Photodetector Array Camera and Spectrometer (PACS) on the Herschel Space Observatory. *Astronomy and Astrophysics*, 518:L2.
- [Preibisch et al., 1993] Preibisch, T., Ossenkopf, V., Yorke, H. W., and Henning, T. (1993). The influence of ice-coated grains on protostellar spectra. *Astronomy and Astrophysics*, 279:577–588.
- [Roussel, 2010] Roussel, H. (2010). Scanamorphos : a map-making software for Herschel and similar bolometer arrays used in scan mode. *Astronomy and Astrophysics*.

- [Schöier et al., 2005] Schöier, F. L., Lindqvist, M., and Olofsson, H. (2005). Properties of detached shells around carbon stars. Evidence of interacting winds. *Astronomy and Astrophysics*, 436:633–646.
- [Science Ground Segment Consortium et al., 2011] Science Ground Segment Consortium, Hifi, P., and Spire Consortia (2011). HIPE: Herschel Interactive Processing Environment. In *Astrophysics Source Code Library, record ascl:1111.001*, page 11001.
- [Sloan et al., 2003] Sloan, G. C., Kraemer, K. E., Price, S. D., and Shipman, R. F. (2003). A Uniform Database of 2.4–45.4 Micron Spectra from the Infrared Space Observatory Short Wavelength Spectrometer. *American Astronomy Society*, 147:379–401.
- [Sloan et al., 1998] Sloan, G. C., Little-Marenin, I. R., and Price, S. D. (1998). The carbon-rich dust sequence - Infrared spectral classification of carbon stars. *Astronomical Journal*, 115:809.
- [van Hoof et al., 2010] van Hoof, P. A. M., van de Steene, G. C., Barlow, M. J., Exter, K. M., Sibthorpe, B., Ueta, T., Peris, V., Groenewegen, M. A. T., Blommaert, J. A. D. L., Cohen, M., De Meester, W., Ferland, G. J., Gear, W. K., Gomez, H. L., Hargrave, P. C., Huygen, E., Ivison, R. J., Jean, C., Leeks, S. J., Lim, T. L., Olofsson, G., Polehampton, E. T., Regibo, S., Royer, P., Swinyard, B. M., Vandenbussche, B., van Winckel, H., Waelkens, C., Walker, H. J., and Wesson, R. (2010). Herschel images of NGC 6720: H<sub>2</sub> formation on dust grains. *Astronomy and Astrophysics*, 518:L137.
- [van Leeuwen, 2007] van Leeuwen, F. (2007). Validation of the new Hipparcos reduction. *Astronomy and Astrophysics*, 474:653–664.
- [Vassiliadis and Wood, 1993] Vassiliadis, E. and Wood, P. R. (1993). Evolution of low- and intermediate-mass stars to the end of the asymptotic giant branch with mass loss. *Astrophysical Journal*, 413:641–657.
- [Walker, 1979] Walker, A. R. (1979). Photometry and Radial Velocities of Southern Carbon Stars. *South African Astronomical Observatory Circular*, 1:112.
- [Wilson, 1953] Wilson, R. E. (1953). General catalogue of stellar radial velocities. *Carnegie Institute Washington D.C. Publication*, page 0.
- [Young et al., 1993] Young, K., Phillips, T. G., and Knapp, G. R. (1993). Circumstellar shells resolved in the IRAS survey data. I - Data processing procedure, results, and confidence tests. *American Astronomy Society*, 86:517–540.
- [Zubko et al., 1996] Zubko, V. G., Mennella, V., Colangeli, L., and Bussoletti, E. (1996). Optical constants of cosmic carbon analogue grains - I. Simulation of clustering by a modified continuous distribution of ellipsoids. *Monthly Notices of the Royal Astronomical Society*, 282:1321–1329.

# Curriculum vitae

**Name:** Bernhard Baumann  
**Address:** Hellwagstraße 15/7/5/21, 1200 Vienna, Austria  
**Email:** bernhard\_baumann@yahoo.de  
**Date & place of birth:** April 5<sup>th</sup> 1985 in Mistelbach, Austria  
**Citizenship:** Austria

## Education

**05/2004** Secondary school diploma at a technical college;  
subject area: technical informatics; A-Level with good success

**10/2004 – 09/2005** community service

**10/2005 – 02/2009** Bachelor study in Astronomy at the University of Vienna; topic:  
“Statistical analysis of homogeneous data sets within open clusters  
in WEBDA, the database for open clusters”

**03/2009 – 04/2012** Master study in Astronomy at the University of Vienna

**09/2010** Hvar Observatory, Croatia; Service and observation; Photometry of  
open star clusters. Furthermore the tracking of the ACT (Austro-  
Croatian-Telescope) and the technical equipment were tested.

## Conferences

Symposium JENAM (New Challenges To European Astronomy), 2010, Sept 8 – 12;  
Technical person in charge for the group “Star Clusters - Witnesses of Cosmic History”;  
Poster and abstract with topic “Statistical analysis of homogeneous data sets within open  
clusters in WEBDA”

## PUBLICATIONS

**The detached dust shells of AQ And, U Ant, and TT Cyg**  
Kerschbaum, F., Ladjal, D., Ottensamer, R., ..., Baumann, B., et al., 2010, Astronomy  
and Astrophysics, Herschel Special Issue 518:L140.